Coordination Chemistry Reviews 550 (2026) 217401

Contents lists available at ScienceDirect

Coordination Chemistry Reviews

journal homepage: www.elsevier.com/locate/ccr

# A Review of Advanced Nanomaterials for Electrochemical Nitrate Reduction to Ammonia

Muhammad Zubair Nawaz [a,c,*,1], Israr Masood ul Hasan [b,1], Waqas Ahmad [c], Huma Gulzar [d], Mai Li [e,*], Bo Weng [f,g], Paul K. Chu [h,*], Na Liu [b,*]

[a] Wuhan National Laboratory for Optoelectronics and School of Optical and Electronic Information, Huazhong University of Science and Technology, Wuhan 430074, China
[b] College of Life Science and Technology, Jinan University, Guangzhou 510632, Guangdong, China
[c] Laboratory of 2D Optoelectronics and Nanoelectronics (L2DON), State Key Laboratory of Quantum Functional Materials, Department of Materials Science and Engineering, Southern University of Science and Technology, 1088 Xueyuan Blvd, Shenzhen 518055, China
[d] School of Chemistry and Chemical Engineering, Harbin Institute of Technology, Harbin 150001, China
[e] College of Science, Donghua University, 201620 Shanghai, China
[f] State Key Laboratory of Advanced Environmental Technology, Institute of Urban Environment, Chinese Academy of Sciences, Xiamen 361021, PR China
[g] University of Chinese Academy of Sciences, Beijing 100049, PR China
[h] Department of Physics, Department of Materials Science and Engineering, and Department of Biomedical Engineering, City University of Hong Kong, Tat Chee Avenue, Kowloon, Hong Kong, China

ARTICLE INFO

*Keywords:*
Electrochemical nitrate to ammonia reduction
electrode fabrication
nanostructured electrocatalysts
carbon-based catalysts
metal oxide catalysts
noble and non-noble metals catalysts
DFT

ABSTRACT

Ammonia ($NH_3$) is essential for global agriculture, chemical synthesis, and emerging as a sustainable energy vector. Conventional Haber–Bosch production, relying on fossil-derived hydrogen, is energy-intensive and a major source of $CO_2$ emissions. Electrochemical nitrate reduction (e-$NO_3$RR) has emerged as a promising alternative, offering the dual advantage of mitigating nitrate pollution while enabling sustainable $NH_3$ synthesis under ambient conditions. This review critically examines recent progress in electrocatalyst design across diverse classes, including carbon-based frameworks, non-noble and noble metals, metal oxides, and multifunctional composites. Advanced strategies such as defect engineering, electronic structure modulation, interfacial tuning, and hybridization are highlighted for their roles in enhancing activity, selectivity, and operational stability. The influence of electrolyte composition, electrode architecture, local reaction microenvironments, and competing pathways is systematically analyzed. Mechanistic insights obtained from in-situ characterization and density functional theory (DFT) calculations are integrated to guide rational catalyst development. Challenges in maximizing nitrogen conversion efficiency, minimizing side reactions, and ensuring long-term durability are discussed, alongside perspectives on system-level integration and scalability. By unifying materials innovation with mechanistic understanding, this review provides a strategic roadmap for advancing e-$NO_3$RR as an efficient, sustainable, and industrially viable platform for $NH_3$ production.

## 1. Introduction

$NH_3$ occupies a central position in modern chemical and energy landscapes, serving as a critical precursor for fertilizers, pharmaceuticals, polymers, and other industrial chemicals, while also emerging as a carbon-neutral energy carrier due to its high hydrogen content and energy density [1–8]. Conventional production via the Haber–Bosch process, although historically transformative, is energy-intensive, relies heavily on fossil-derived hydrogen, and contributes significantly to global greenhouse gas emissions [9–11]. The urgent need for sustainable alternatives has catalyzed research into electrochemical routes for $NH_3$ synthesis, particularly the e-$NO_3$RR, which uniquely couples environmental remediation with value-added chemical production. Nitrate, a prevalent contaminant in industrial effluents, agricultural runoff, and polluted water bodies, exhibits high solubility and chemical stability, posing serious ecological and health risks [12–14]. Its electrochemical conversion to $NH_3$ therefore presents a promising strategy to "turn waste

* Corresponding authors.
*E-mail addresses:* zubair@mail.dhu.edu.cn (M.Z. Nawaz), limai@dhu.edu.cn (M. Li), paul.chu@cityu.edu.hk (P.K. Chu), liuna@jnu.edu.cn (N. Liu).
[1] These authors contributed equally to this work.

https://doi.org/10.1016/j.ccr.2025.217401
Received 15 September 2025; Accepted 19 November 2025
Available online 26 November 2025
0010-8545/© 2025 Elsevier B.V. All rights are reserved, including those for text and data mining, AI training, and similar technologies.

**Nomenclature**

($NH_3$) Ammonia
(e-$NO_3$RR) Electrochemical nitrate reduction
($NO_3^- \rightarrow NH_3$) Nitrate to ammonia reduction
(DFT) Density functional theory
(AWE) Alkaline water electrolyzers
(PEM) Proton-exchange membrane
(SOECs) Solid oxide electrolysis cells
(AEM) Anion-exchange membrane
(FE) Faradaic efficiency
(HER) Hydrogen evolution reaction
(PCET) Proton-coupled electron transfer
(RDS) Rate determining step
($NH_4^+$) Ammonia ion
(XAS) X-ray absorption spectroscopy
(XANES) X-ray absorption near-edge structure
(EXAFS) Extended X-ray absorption near-edge structure
(e-NRR) Electrochemical nitrogen reduction reaction
(OCP) Open-circuit potential
(IR) Infrared
(DEMS) Differential electrochemical mass spectroscopy
(e-$NO_2$RR) Electrochemical nitrite reduction reaction
(SECM) Scanning electrochemical microscopy
(EQCM) Electrochemical quartz crystal microbalance
(EPR) Electron paramagnetic resonance
(AEMC) Alkali-etched microchannel charcoal
(ox-LIG) Oxidized laser-induced graphene
(sm-LIG) Small molecule laser-induced graphene
(PDF) Pair distribution functionals
(W-CCNs) Tungsten-doped carbon co-axial nanocubes
(CNTs) Carbon nanotubes
(MWCNTs) Multi-walled carbon nanotubes
(SWCNTs) Single walled carbon nanotubes
(LSV) Linear sweep voltammetry
(BCN) Boron carbon nitride
(DOS) Density of states
($O_v$) Oxygen vacancy
($Co_{oh}$) Octahedral cobalt
($Co_{Td}$) Tetrahedral cobalt
(CoP) Cobalt phosphide
(PDS) Potential-determining step
(NTs) Nanotubes
(LDH) Layered double hydroxide

into wealth," aligning pollutant abatement with green chemical production.

The e-$NO_3$RR represents a highly intricate process, governed by multi-electron and multi-proton transfer events and further complicated by competing pathways such as hydrogen evolution and the formation of partially reduced intermediates. Traditional nitrate remediation strategies including biological denitrification, ion-exchange resins, reverse osmosis, and catalytic hydrogenation are constrained by high energy input, operational complexity, and limited scalability [15–18]. In contrast, electrocatalysis provides a sustainable and tunable platform. However, its widespread deployment hinges on addressing critical challenges such as optimizing electron transport, tailoring nitrate adsorption, and engineering catalysts capable of selectively driving the desired reaction pathways [19–23]. Over the past decade, e-$NO_3$RR has matured into a rapidly advancing research frontier, driven by innovations in noble metals, transition metals, carbonaceous frameworks, metal oxides, single-atom architectures, and multifunctional hybrid composites. These materials exploit diverse strategies such as defect engineering, electronic structure modulation, interfacial heterojunctions, and morphology-controlled design to enhance nitrate conversion and product yield [24–27]. Yet, progress remains fragmented, with most investigations confined to isolated material classes [1,3,4,6,9,11–17,21,28,29].

This review seeks to integrate these scattered advances within a unified framework, systematically correlating structural features, electronic configurations, and mechanistic pathways with electrocatalytic performance. By consolidating state-of-the-art knowledge and illuminating the interplay between material design and functional efficiency, this work provides a roadmap for the rational development of high-performance catalysts, advancing the vision of scalable, sustainable, and industrially viable $NH_3$ production from nitrate. This review systematically unravels the multifaceted aspects of electrochemical nitrate-to- $NH_3$ conversion, beginning with the foundational roles of electrodes, their fabrication strategies, and the influence of surface interactions on reaction dynamics. It further outlines mechanistic pathways that govern product distribution. The subsequent sections emphasize system-level considerations, including electrolyte engineering, pH-dependent modulation, nitrate concentration effects, and structural classification of catalysts. Advanced spectroscopic and operando characterization approaches, together with DFT modeling, are also highlighted as essential tools for mechanistic elucidation and predictive catalyst design. A comprehensive survey of catalytic architectures spanning carbon-based frameworks, non-noble metals, metal oxides, and noble metals provides a holistic view of material innovations shaping this field. Concluding with perspectives on current challenges and future opportunities, this review underscores rational design strategies as a blueprint for developing next-generation electrocatalysts, aiming to accelerate the realization of sustainable, high-efficiency $NO_3^- \rightarrow NH_3$ conversion.

## 2. Comparative Evaluation of $NH_3$ Synthesis Pathways: Electrochemical versus Hydrogen-Mediated Routes

$NH_3$ continues to be a foundational chemical in global industry, predominantly produced via the Haber-Bosch process, which catalytically combines $N_2$ and $H_2$ under elevated temperatures and pressures over iron-based catalysts. Traditionally, hydrogen is sourced from fossil fuels through steam methane reforming or coal gasification, processes that contribute significantly to $CO_2$ emissions, thereby imposing a substantial carbon footprint on conventional $NH_3$ production [30]. To address these environmental constraints, alternative hydrogen generation strategies have been developed, including thermocatalytic methane decomposition, chemical looping, and water electrolysis powered by renewable energy. Thermocatalytic methane decomposition produces high-purity $H_2$ with solid carbon as the sole byproduct avoiding $CO_2$ emissions, while chemical looping leverages cyclic oxygen transfer to generate $H_2$ with minimal emissions [31]. Renewable electricity-driven water electrolysis supplies green $H_2$, which can either feed conventional Haber-Bosch synthesis or enable emerging direct and mediated electrochemical nitrogen reduction processes, potentially bypassing Haber-Bosch entirely [32]. Nevertheless, the widespread adoption of these methods remains constrained by high energy intensity, renewable intermittency, and substantial infrastructure requirements.

Second-generation green $NH_3$ integrates green hydrogen into existing Haber-Bosch infrastructure by replacing fossil-derived $H_2$ with electrolytically produced hydrogen, powered by renewable electricity [32]. This approach preserves the core Haber-Bosch synthesis loop, substituting steam methane reforming units with water electrolyzers. However, the variability of renewable power necessitates the deployment of energy or hydrogen storage systems to maintain a continuous and stable hydrogen feed, representing a critical operational challenge.

Optimization of process integration and mitigation of renewable intermittency are therefore essential for achieving economically and operationally viable green $NH_3$ production.

Hydrogen generation technologies vary significantly in maturity, efficiency, and operational characteristics. Alkaline water electrolyzers (AWE) represent the most established technology, operating at moderate temperatures (60-90 °C) and pressures (1-30 bar) using alkaline electrolytes (KOH or NaOH) with cost-effective nickel- or cobalt-based electrodes [33]. AWE systems achieve 65-70% efficiency with energy consumption of 29-46 GJ $t_{NH_3}^{-1}$ and stack lifetimes of 60,000-90,000 h. Despite their economic advantages, AWE units exhibit slower dynamic response and require careful handling of corrosive electrolytes. Proton-exchange membrane (PEM) electrolyzers function at low temperatures (30-100 °C) and high pressures (10-200 bar) using Nafion membranes, with iridium anodes and platinum cathodes facilitating oxygen and hydrogen evolution. These systems allow high current densities and rapid responsiveness, achieving 80-90% efficiency at 31-46 GJ $t_{NH_3}^{-1}$ [33]. Their deployment is limited by high noble metal costs and accelerated membrane degradation in acidic environments. Solid oxide electrolysis cells (SOECs) operate at elevated temperatures (600-1000 °C for O-SOEC), offering 90-100% efficiency with energy consumption around 25 GJ $t_{NH_3}^{-1}$ and benefit from heat integration with industrial processes [34]. However, high operating temperatures accelerate material degradation, shorten stack lifetimes (10,000-30,000 h), and increase capital costs. Anion-exchange membrane (AEM) electrolyzers, although still emerging, combine AWE and PEM advantages, enabling high current densities (up to 500 mA $cm^{-2}$) with non-precious electrodes in alkaline conditions, operating at 30-80 °C and moderate pressures (~30 bar) [35,36]. AEM technology faces challenges including membrane degradation, voltage losses, and limited integration data for $NH_3$ synthesis. Each hydrogen generation route presents unique trade-offs in efficiency, cost, scalability, and adaptability to renewable energy, highlighting the importance of informed technology selection for sustainable green $NH_3$ production.

e-$NO_3$RR offers a complementary direct pathway to $NH_3$, converting $NO_3^-$ to $N_2$ and $NH_4^+$ through a multi-electron, proton-coupled process [32]. The product distribution is highly pH-dependent, with $NH_4^+$ predominating below pH 9.25 and $NH_4OH$ forming at higher pH, whereas $N_2$ is generally thermodynamically favored ($E^0 = 1.246$ V vs. SHE) [33]. e-$NO_3$RR involves complex reaction networks with intermediates such as $NO_2$, NO, $N_2O$, and $NH_2OH$, characterized by slow electron-proton transfer kinetics, high activation barriers and substantial overpotentials, resulting in low selectivity [32]. Catalyst composition, electrode surface structure, applied potential, and electrolyte environment strongly influence reaction pathways, yet achieving high FE toward a specific nitrogen product remains limited by competing reactions and intermediate desorption dynamics. Advanced mechanistic understanding, including transient species behavior and interfacial proton-electron interactions, is critical to enhance selectivity and efficiency in e-$NO_3$RR, positioning it as a promising alternative or complementary strategy alongside hydrogen-mediated $NH_3$ synthesis. We specifically emphasize the e-$NO_3$RR route for $NH_3$ synthesis, with subsequent sections providing an in-depth analysis of system design, catalyst engineering, reaction pathways, and strategies to improve selectivity and efficiency, and mechanistic insights supported by DFT calculations.

## 3. Cutting-Edge Approaches in Electrochemical Nitrate-to-Ammonia Conversion: Synthesis Strategies, Mechanistic Insights, Classification, Characterization, and Current Advances

### 3.1. Role and requirement of electrode in electrochemical processes

In the electrochemical reduction of $NO_3^- \rightarrow NH_3$, electrodes play a fundamental role in determining the overall efficiency, product selectivity, and operational stability [37]. The cathode serves as the active platform where nitrate ions undergo sequential proton-electron transfer steps, culminating in $NH_3$ formation. The efficacy of the cathode is influenced by multiple factors, including its electrical conductivity, surface chemical composition, structural robustness, and ability to minimize competing reactions such as hydrogen evolution [38]. Morphological features like high surface area, optimized porosity, and defect sites enhance catalytic performance by increasing accessible active sites and facilitating effective mass transport [39]. The anode generally consists of chemically inert and stable materials, tasked with supporting the complementary oxidation half-reaction without interfering with nitrate reduction at the cathode [40]. A reference electrode is employed to maintain precise control over the applied potential, ensuring reproducibility and accuracy in electrochemical measurements. Achieving an optimal balance among catalytic activity, selectivity, and electrode durability is essential to maximize $NH_3$ yield while minimizing energy consumption.

Electron transfer at the electrode interface can occur via two distinct mechanistic pathways [42], as depicted in Fig. 1. In the first scenario (Fig. 1a), the electrode actively catalyzes the reaction, with electron transfer occurring through an inner-sphere mechanism. The electrode material's composition strongly governs the reaction pathway, product distribution, and kinetics, making subtle material changes significantly impactful [43]. In contrast, the second scenario (Fig. 1b) involves an inert electrode that functions simply as an electron reservoir, enabling outer-sphere electron transfer without direct involvement in the catalytic process. Here, the electrode material has negligible influence on reaction outcomes. The electrolyte's chemical properties also substantially shape the interfacial chemistry at the electrode-electrolyte boundary. Parameters such as pH, buffering capacity, and supporting ion identity affect nitrate adsorption, activation energy barriers, and reduction kinetics. Acidic electrolytes, abundant in protons, tend to accelerate competing hydrogen evolution reaction (HER), reducing $NH_3$ selectivity. Alternatively, alkaline electrolytes promote nitrate adsorption and hinder proton reduction but may pose risks of electrode corrosion depending on material compatibility [44]. Thus, electrolyte selection requires a nuanced balance between maximizing catalytic activity and preserving electrode integrity.

Compatibility between electrolyte and electrode is critical to avoid surface passivation or degradation. Certain electrolytes may induce the formation of insulating films through precipitation of reaction intermediates or electrolyte decomposition products, which impede electron transfer and reduce catalytic longevity [45]. Additives can be employed to stabilize intermediates, increase solubility of fouling species, or modify the electrode interface to enhance catalytic performance and durability. Mass transport phenomena within the electrolyte are vital to maintaining high reaction rates. The diffusion coefficients of

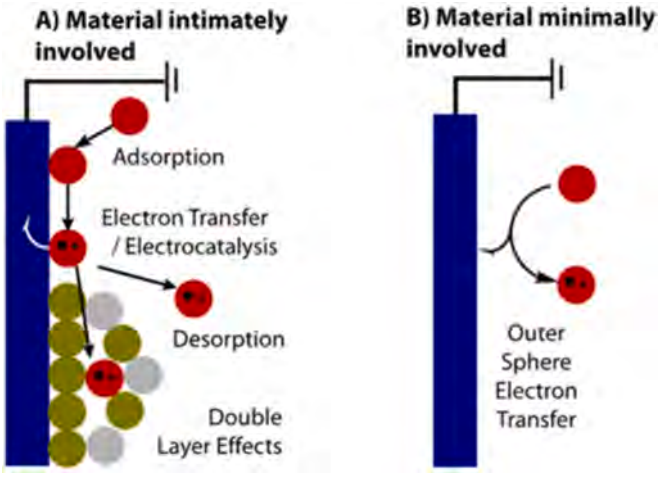



**Fig. 1.** Limiting regimes that define the kinetics of electron transfer. Reproduced with Permission from [41].

nitrate and supporting ions dictate how effectively reactants reach catalytic sites. Poor mass transport results in concentration gradients and polarization effects that limit current density and favor unwanted side reactions. Approaches such as modifying electrolyte viscosity, implementing forced convection, or tailoring ion-solvent interactions can substantially improve mass transport and thereby increase productivity [46].

Electrolyte composition also influences reaction thermodynamics and kinetics. Each step of the nitrate reduction pathway such as adsorption, electron transfer, desorption, and diffusion is sensitive to electrolyte environment [47,48]. Supporting electrolytes with high ionic strength reduce ion migration effects, facilitating a uniform potential profile on the electrode surface. Furthermore, specific ions can selectively adsorb onto catalytic sites, acting as promoters or inhibitors that modulate the activation energy and reaction rate [49]. Operational stability of the electrolyte under applied electrochemical conditions is another crucial consideration. Electrolyte breakdown can result in irreversible adsorption of decomposition products on the electrode surface, as shown in Fig. 2a, leading to catalyst deactivation and diminished product yield [50]. While intentional grafting of organic molecules onto electrodes has been used to enhance catalytic properties, unintentional film formation from electrolyte degradation creates electrically insulating layers that passivate the surface [51], illustrated in Fig. 2b. Mitigation strategies include optimizing electrode composition, employing pulse electrolysis, sonication, alternating electrode polarity, or introducing redox mediators that shuttle electrons away from the surface, maintaining catalytic activity [52,53]. The electrochemical stability window of the electrolyte, defined by the potentials at which solvent oxidation or reduction occur, limits the safe operational range and guides material selection. For practical and industrial-scale applications, considerations beyond performance include electrolyte cost, environmental impact, and handling safety. Ideal electrolytes are affordable, non-toxic, readily available, and compatible with continuous processes [54,55]. Recyclability and minimal environmental footprint are also key factors in the sustainable deployment of e-$NO_3$RR technologies.

### 3.2. Electrode Fabrication and Reaction Mechanism

#### 3.2.1. Electrode Fabrication: Role of Surface Interactions in Electrocatalysis

In electrochemical systems where the electrode surface directly participates in the reaction mechanism as illustrated in Fig. 1, electron transfer is closely coupled with specific adsorption and surface-mediated processes. Beyond serving as mere electron donors or acceptors, these electrodes function as catalysts by facilitating reaction pathways through their surface states, a phenomenon referred to as electrocatalysis [56]. As defined by Daniel, electrocatalysis involves the acceleration of electrochemical reactions via the active sites present on the electrode surface, distinguishing it from mediated electrolysis, which relies on discrete molecular catalysts in solution. The intricate nature of substrate-electrode interactions varies with the electrochemical reaction and often involves complex mechanistic details that remain under active investigation. Advances in theoretical modeling now enable comprehensive descriptions of these catalytic processes, including the adsorption-desorption equilibria, sequential electron transfer events, and the concertedness of multi-step reactions [57–59]. Adsorption encompasses a range of substrate binding modes, such as strong electrostatic forces, π–π interactions, and the formation of chemical bonds with the electrode surface.

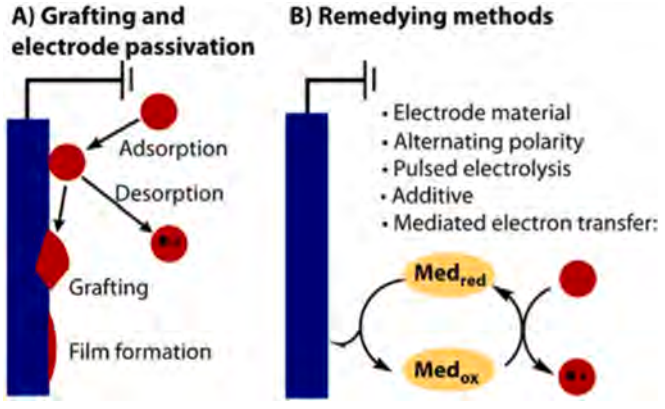



**Fig. 2.** Surface deactivation of the electrode. Reproduced with permission from [41]

The catalytically active sites are not restricted to the bulk electrode material alone. They may include structural defects, edge or corner atoms, surface-bound nanoparticles, ultrathin films, or even isolated single atoms of different elements deliberately introduced during electrode fabrication [60,61]. These engineered sites can significantly influence the reaction kinetics and selectivity. A critical design principle guiding electrode fabrication is the optimization of the interaction strength between the electrode surface and the reacting species. According to the Sabatier principle, the binding affinity must be sufficiently strong to activate the substrate and lower the reaction barrier, yet weak enough to allow facile desorption of the product [62]. This balance is essential to maximize catalytic turnover and has been evidenced in the characteristic volcano-type activity plots observed for reactions such as the HER [63,64]. In certain organic electrochemical transformations, strong adsorption of products onto the electrode surface can impede their release, causing surface fouling and degradation of catalytic performance, as depicted in Fig. 2a. Such surface-bound intermediates may undergo further unintended reactions, reducing overall mass balance and product yield. Hence, electrode fabrication strategies must also consider surface stability and resistance to poisoning to maintain long-term functionality.

#### 3.2.2. Reaction Mechanism

The e-$NO_3$RR in aqueous electrolytes is a heterogeneous process characterized by complex multi-step proton-coupled electron transfer (PCET) events [65]. The nitrogen species involved traverse a broad range of oxidation states, from +5 in nitrate ($NO_3^-$) down to −3 in $NH_3$, with various intermediates formed throughout the reaction pathway (Fig. 3b). This complexity leads to multiple possible products, predominantly nitrogen gas ($N_2$) and $NH_3$, governed by thermodynamics and reaction conditions [66–68].

Two primary overall reduction reactions can be summarized as follows:

$$N_2\text{Production}: 2NO_3^- + 12H^+ + 10e^- \rightarrow N_2 + 6H_2O \quad (E^0 = 1.17\,\text{V vs SHE}) \tag{1}$$

$$NH_3\text{Production}: NO_3^- + 9H^+ + 8e^- \rightarrow NH_3 + 3H_2O \quad (E^0 = -0.12\,\text{V vs SHE}) \tag{2}$$

The pH of the electrolyte critically influences the speciation of the $NH_3$ product: below pH 9.25, $NH_4^+$ ions dominate, whereas above this pH, $NH_3$ primarily exists as aqueous $NH_4OH$ [69]. Importantly, the HER, with a reduction potential overlapping the e-$NO_3$RR window, poses a significant competing pathway, often diminishing the Faradaic efficiency (FE) for $NH_3$ production [70,71].

*3.2.2.1. Initiation and Rate-Determining Step.* The e-$NO_3$RR is initiated by the adsorption of nitrate ions onto catalytically active sites on the electrode surface (*$NO_3^-$), a process influenced by surface pH, ionic impurities, and nitrate diffusion dynamics [72]. This adsorption step sets the stage for subsequent reduction steps:

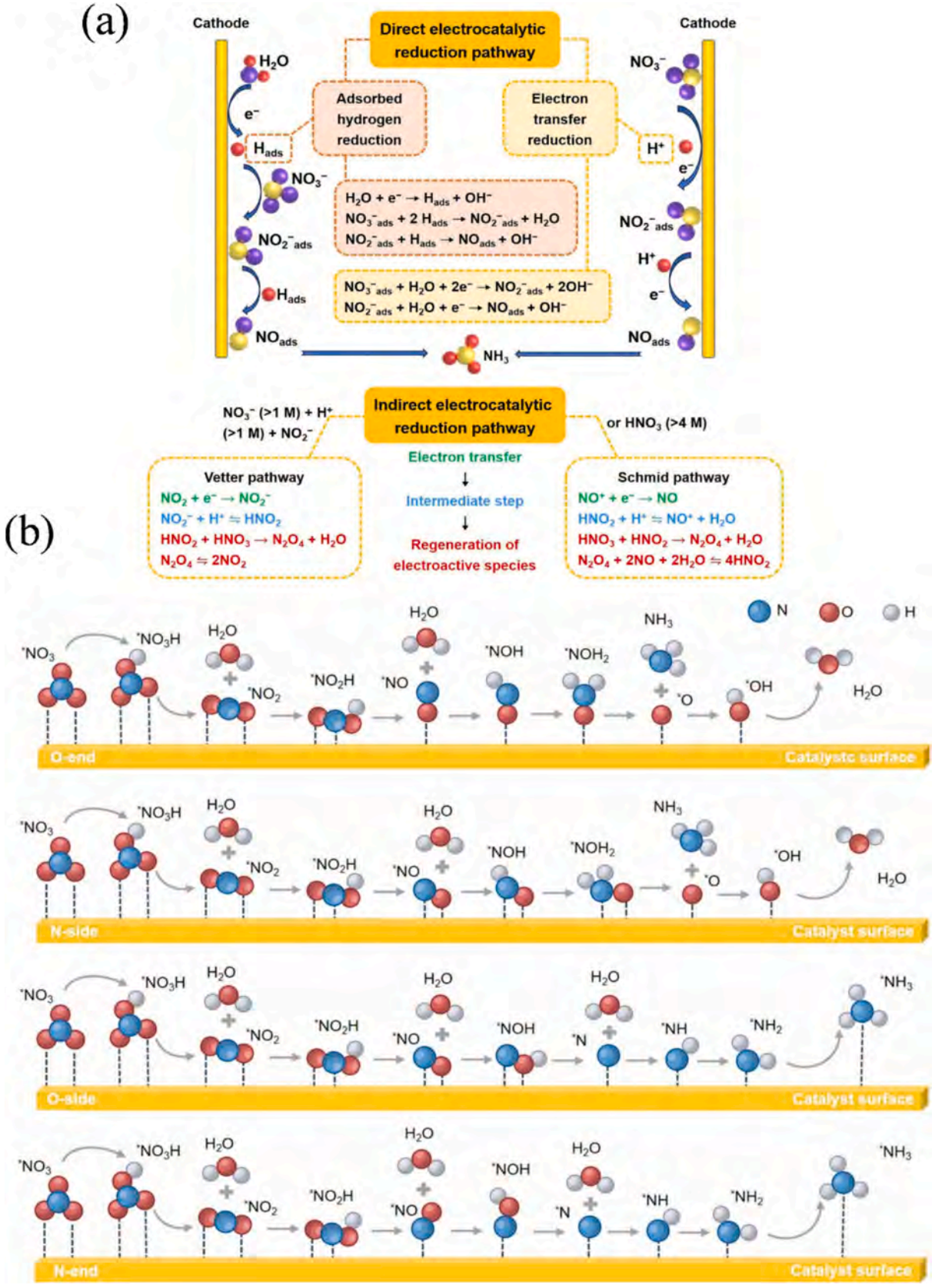



**Fig. 3.** a) Schematic illustration of both direct and mediated routes involved in e-$NO_3$RR. b) Detailed representation of $NO_3^-$ reduction pathways, highlighting the O-terminal, N-terminal, O-side, and N-side reaction channels. Reproduced with permission from [14,65]

$$NO_3^- + * \rightarrow *NO_3^- \quad (3)$$

The critical rate determining step (RDS) involves the two-electron, two-proton reduction of adsorbed nitrate to nitrite:

$$*NO_3^- + 2H^+ + 2e^- \rightarrow *NO_2^- + H_2O \quad (4)$$

This process can be further deconvoluted into sub-steps involving electron and proton transfers, where the formation of the surface-bound $NO_2^{2-}$ intermediate ($*NO_2^{2-}$) through the first electron transfer is widely regarded as the kinetic bottleneck, supported by Tafel slope analyses (~120 mV/decade) across various catalytic metals such as Ru, Rh, Ir, Pt, Cu, and Ag [73,74].

*3.2.2.2. Divergent Pathways: Direct vs. Indirect Reduction.* After the formation of the $*NO_2$ intermediate, the reaction proceeds along two distinct routes (Fig. 3a). In the first, $*NO_2$ is reduced to adsorbed nitric oxide (*NO), which then undergoes successive protonation and electron transfer steps leading to the production of either $NH_3$ or nitrogen gas ($N_2$) [75,76]. The subsequent transformation of *NO plays a crucial role in determining the final product distribution (see above portion, Fig. 3a) [77,78]. In the second route, occurring primarily under strongly acidic conditions with high nitrate concentrations, the dissociated nitrite ion ($NO_2^-$) can convert into nitrous acid ($HNO_2$) or nitrogen dioxide ($NO_2$) [79,80]. These species engage in indirect autocatalytic reactions, though this pathway is generally less dominant under typical neutral or alkaline nitrate reduction environments (see bottom portion, Fig. 3a) [81–83].

*3.2.2.3. Detailed $NH_3$ Formation Mechanism.* The formation of $NH_3$ proceeds primarily via three distinct *NO adsorption geometries on the catalyst surface:

***O-End Adsorption*:** Reduction proceeds through sequential PCET steps involving protonation of *NO to *HNO, then $*H_2NO$, culminating in $NH_3$ release and *O regeneration [84–86]. The rate-limiting step is generally the protonation of *HNO to $*H_2NO$.

$$*NO + H^+ + e^- \rightarrow *HNO \quad (5)$$

$$*HNO + H^+ + e^- \rightarrow *H_2NO \quad (6)$$

$$*H_2NO + H^+ + e^- \rightarrow NH_3 + *O \quad (7)$$

***N-End Adsorption*:** This pathway involves the protonation of *NO to *NOH, followed by stepwise hydrogenation to *N, *NH, $*NH_2$, and finally $NH_3$. Suppression of N–N coupling between *NO species is crucial here to avoid $N_2$ formation [87–89].

$$*NO + H^+ + e^- \rightarrow *NOH \quad (8)$$

$$*NOH + H^+ + e^- \rightarrow *N + H_2O \quad (9)$$

$$*N + H^+ + e^- \rightarrow *NH \quad (10)$$

$$*NH + H^+ + e^- \rightarrow *NH_2 \quad (11)$$

$$*NH_2 + H^+ + e^- \rightarrow NH_3 + * \quad (12)$$

Subsequent hydrogenations proceed until $NH_3$ is released.

***Side-On NO Adsorption*:** Protonation at either the N or O side influences the subsequent reduction steps [90,91]. Protonation at the O side can generate intermediates like *HNOH and $*H_2NOH$, which can desorb as hydroxylamine ($NH_2OH$) before further reducing to $NH_3$.

$$*NOH + H^+ + e^- \rightarrow *HNOH \quad (13)$$

$$*HNOH + H^+ + e^- \rightarrow H_2NOH + * \quad (14)$$

$$H_2NOH + 2H^+ + 2e^- \rightarrow NH_3 + H_2O \quad (15)$$

*3.2.2.4. Competing Reactions and Catalyst Design Considerations.* During e-$NO_3$RR, the formation of undesired side-products such as $N_2$ and $NO_2^-$ results from alternative reaction pathways involving N–N coupling or premature desorption of intermediates [92]. Particularly, strong O-binding catalyst sites favor these side reactions, reducing $NH_3$ yield and increasing energy losses. Moreover, the HER competes for electrons and protons at overlapping potentials, often diverting charge away from nitrate reduction and reducing $NH_3$ FE. To mitigate these challenges, catalyst design strategies such as heteroatom doping, defect engineering, and metal alloying have been employed to fine-tune adsorption energies, enhance electron transfer kinetics, and suppress HER activity [93].

### 3.3. System Design

The design of an efficient electrochemical system for nitrate reduction requires a holistic approach that addresses both catalytic and operational parameters. The e-$NO_3$RR offers a dual benefit such as remediation of nitrate-contaminated water and recovery of $NH_3$ as a high-value product. Yet, its large-scale deployment demands careful optimization of system architecture to ensure high selectivity, reduced energy consumption, and prolonged catalyst stability.

#### *3.3.1. Electrolyte Engineering: Cation and Anion Effects on Nitrate Reduction*

The nature of the supporting electrolyte exerts a substantial influence on the efficiency, selectivity, and mechanistic pathways of the e-$NO_3$RR. Both the identity of cations and anions can alter interfacial charge distribution, adsorption behavior, and intermediate stabilization, thereby modulating the overall reaction kinetics [94]. Systematic investigations have demonstrated that alkali metal cations follow a clear activity trend for nitrate reduction, typically increasing in the order $Li^+ < Na^+ < K^+ < Cs^+$. Notably, ammonium ions ($NH_4^+$) can promote even higher nitrate reduction rates than alkali cations, outperforming multivalent species such as $Ca^{2+}$ and $La^{3+}$. The observed behavior aligns with the cation catalysis theory, wherein cations accumulate at the outer Helmholtz plane and form ion pairs with reduced nitrate intermediates. These ion pairs are less strongly repelled by the negatively charged electrode, enabling more efficient electron transfer. The relative strength of these cation-nitrate interactions can be described by their association constants, reported as $Cs^+$ (2.35), $K^+$ (2.04), $Na^+$ (1.43), and $Li^+$ (0.65) [94,95].

Cation identity not only affects reaction rates but also product distribution. Mass spectrometric analyses have shown that when $K^+$ serves as the electrolyte cation, $N_2$ is the dominant product, aided by a moderate HER that facilitates nitrate-hydrogen interaction [94,95]. In contrast, $Na^+$ electrolytes tend to produce $N_2O$ as the primary product, a consequence of faster HER kinetics that hinder molecular hydrogen formation and alter the reaction pathway [95,96]. Multivalent cations can exert additional catalytic effects. For example, $La^{3+}$ in the supporting electrolyte has been observed to positively shift the zero-charge potential of polycrystalline Ag electrodes, suggesting enhanced nitrate reduction via acid-base catalysis. Experimental evidence also indicates deposition of $La(OH)_3$ films and the formation of $La^{3+}$–$NO_3^-$ ion pairs, where $La^{3+}$ acts as an $OH^-$ acceptor or proton donor, facilitating PCET steps. In contrast, $Al^{3+}$ displays negligible enhancement, attributed to its inability to form strong ion pairs with nitrate [97].

Anions in the supporting electrolyte also impact electrochemical nitrate reduction kinetics by competing with nitrate for adsorption and ion pairing. Halide ions follow the reactivity sequence $I^- > Br^- > Cl^- > F^-$, with iodide showing minimal ion pairing with nitrate, thereby reducing competitive adsorption and enabling faster reduction rates. The ionic composition of the electrolyte, particularly the cation-anion pairing can profoundly influence both reaction efficiency and selectivity [13,98]. This has important implications for nitrate reduction under practical conditions, especially in real wastewater treatment scenarios, where complex ionic matrices necessitate deliberate electrolyte engineering to

achieve optimal performance [99]. The role of the supporting electrolyte and the performance of specific catalysts in e-$NO_3$RR are summarized in Table 1.

### 3.3.2. pH-Mediated Control of Nitrate Reduction

A critical aspect of system design lies in tailoring the electrolyte environment. Parameters such as ionic composition, buffer capacity, and pH significantly influence the reaction pathway, intermediate stabilization, and competition from side reactions like the HER. Fine control over pH not only alters the thermodynamics of nitrate conversion but also impacts the adsorption behavior of nitrogen-containing intermediates on the catalyst surface. To further elucidate the thermodynamic influence of pH, a comparative analysis of the reduction potentials of different nitrogen sources such as nitrate ($NO_3^-$), nitrite ($NO_2^-$), and molecular nitrogen ($N_2$) toward $NH_3/NH_4^+$ under varying pH conditions is illustrated in Scheme 1 [100]. Compared with the strong N≡N triple bond in molecular nitrogen, the electrochemical reduction of nitrate and nitrite is energetically more favorable due to their lower activation barriers and the environmental necessity of mitigating nitrate contamination. As shown in Scheme 1, the reduction potentials of these nitrogen sources vary considerably with pH. Reactions conducted in neutral media demand higher overpotentials, while nitrate and nitrite reductions are more feasible in acidic or mildly neutral conditions. Conversely, nitrogen reduction can proceed over a wider pH range but generally yields lower $NH_3$ production and FE. This difference arises because nitrogen reduction is more susceptible to the competing HER, which inhibits $NH_3$ formation, whereas moderate surface hydrogen species can facilitate $NO_3^-/NO_2^-$ reduction [100]. Scheme 1 also summarizes the reported reduction potentials on various substrates, including carbon paper, carbon cloth, and nickel foam. This comparative insight underscores that nitrate and nitrite electroreduction pathways are both thermodynamically and practically more favorable than direct nitrogen reduction under ambient aqueous conditions.

Electrolyte pH plays a decisive role in determining the product distribution and reaction pathway of the e-$NO_3$RR. For example, on Cu single crystals, acidic electrolytes favor the formation of NO and $NH_3$ in Fig. 4a, whereas alkaline conditions predominantly lead to nitrate-to-nitrite conversion, followed by further reduction to hydroxylamine [79]. The enhanced activity in acidic media is generally attributed to the abundant proton supply, which accelerates PCET steps. However, investigating e-$NO_3$RR over a wide pH range is essential for understanding proton-intermediate interactions and broadening its practical applicability [101].

Catalyst-specific trends further illustrate the complex pH dependence. When Rh served as the cathode, nitrate reduction activity decreased with increasing pH. In the case of Fe single-atom catalysts, the FE for $NH_3$ synthesis in alkaline media (pH = 13.0) was comparable to that at neutral pH, but a significantly higher overpotential was required, and both catalytic activity and selectivity declined sharply under acidic conditions (pH = 1.0) [105]. For Ti electrodes, the highest current density occurred at strongly alkaline pH (13.0), whereas strongly acidic conditions (pH ≈ 0.77) improved $NH_3$ selectivity likely due to the synergistic effects of proton availability and nitrate adsorption at the Ti surface [106]. Beyond its impact on reduction kinetics, pH critically influences the anodic oxidation behavior of nitrogen species during electrolysis. At the anode, direct oxidation can generate nitrogen, nitrite, and nitrate, with this process becoming increasingly favorable as the solution pH exceeds approximately 9.25. Under acidic and neutral conditions, ammonium ($NH_4^+$) is the dominant nitrogen species (Fig. 4b). Its positive charge promotes strong electrostatic adsorption onto the anode surface, effectively impeding further oxidation. In contrast, molecular $NH_3$ exhibits weaker electrostatic interactions, allowing easier adsorption and enhanced oxidation at alkaline or near-neutral pH. Nevertheless, the direct oxidation pathway often demonstrates poor nitrogen selectivity, as $NH_3$ tends to oxidize predominantly into nitrate rather than nitrogen gas. For instance, during electrolysis using a graphite anode, roughly 25% of $NH_3$ was converted into nitrogen, while the majority underwent oxidation to nitrate.

From a mechanistic standpoint, pH can modulate the RDS, preferred reaction pathways, and limiting potentials by altering adsorption free energies (e.g., GNO* and $GNH_2$*), local atomic coordination, and the electronic structure of active sites [107]. Alkaline electrolytes often yield superior performance due to the abundance of $OH^-$ ions, which enhance nitrate adsorption/activation, promote efficient electron transfer, and stabilize key intermediates, thereby favoring $NH_3$ formation while suppressing the HER. In contrast, neutral electrolytes such as phosphate-buffered saline or $Na_2SO_4$ generally exhibit lower $NH_3$ yields, primarily due to weaker nitrate intermediate protonation and higher competition from HER [108,109]. For instance, Co single-atom catalysts (Co@NC and Co/NC-800) achieved $NH_3$ yield rates of 500 and 44 mmol $h^{-1}$ $g^{-1}$ in 0.1 M KOH and 0.1 M $Na_2SO_4$, respectively, with corresponding FEs of 96.5 % and 88.2 %. These observations underscore the importance of systematic studies across varying pH, salinity, and electrolyte compositions to optimize $NO_3$RR performance and elucidate mechanistic pathways [110–112].

### 3.3.3. Role of Nitrate Concentration

Nitrate concentration is another determinant of reaction performance. Low nitrate concentrations may limit reaction rates due to insufficient reactant availability, whereas excessively high concentrations can promote mass transport limitations and favor undesired byproducts. Establishing an optimal concentration range is thus essential for balancing conversion efficiency with product selectivity [113]. The concentration of nitrate in the electrolyte is a critical factor governing both the kinetics and selectivity of the e-$NO_3$RR. At low concentrations, nitrate reduction is limited by mass transport, as the initial adsorption of $NO_3^-$ onto the catalyst surface is diffusion-controlled. Increasing nitrate concentration mitigates this limitation, shifting the RDS to the availability and activity of active sites on the electrocatalyst. High nitrate concentrations can also promote autocatalytic reaction pathways, accelerating overall reduction rates and improving FE.

Experimental evidence demonstrates that the performance of catalysts, such as Co-based materials, is strongly dependent on nitrate availability. For instance, in alkaline media with high nitrate concentration (1.0 M $NaNO_3$ and 1.0 M NaOH), CoP catalysts achieve near-complete conversion with $NH_3$ yields of 9.56 mmol $h^{-1}$ $cm^{-2}$ and FE approaching 100 % (Fig. 4c-e). The combination of abundant nitrate ions and stabilizing hydroxide ions ensures continuous supply to active sites and facilitates multi-step reduction to $NH_3$ via stabilized intermediates like $NO_3^-$ and $NO_2^-$ [113]. Conversely, in low-concentration electrolytes (0.005 M $NaNO_3$), the same CoP/CC catalyst exhibits dramatically reduced performance, with $NH_3$ yields of only 0.018 mmol $h^{-1}$ $cm^{-2}$ and FE of 65 %. Here, limited nitrate availability decreases the frequency of productive catalytic cycles, while competing reactions such as hydrogen evolution become more pronounced [114].

Effective nitrate reduction at both low and high concentrations requires strategies to optimize reactant availability and product removal [115,116]. Pre-treatment methods can concentrate nitrate in wastewater to levels suitable for electrochemical processing, while operational parameters such as current density, applied potential, temperature, stirring, electrolyte flow, and electrode modifications can enhance local nitrate enrichment and improve electron transfer rates [6,117]. Timely desorption or removal of the generated $NH_3$ from the catalyst surface is also crucial, as accumulation can block active sites and reduce FE, particularly at high nitrate concentrations. Controlling nitrate concentration is essential for maximizing catalytic activity, selectivity, and FE. High nitrate levels ensure sustained reactant supply to active sites, favor multi-step reduction pathways, and reduce side reactions, while low concentrations necessitate tailored system designs to overcome mass transport limitations and maintain efficient $NH_3$ production [118].

**Table 1**
Comparative Overview of Catalyst Performance, Cell Architectures, Quantification Techniques, Product Distribution, and Reaction Conditions.

| Name of Catalyst | Electrolyte | Temperature | Cell Type | $NH_3$ Yield Rate | FE (%) | Quantification Method | Product | Electrolyte Medium | Ref. |
|---|---|---|---|---|---|---|---|---|---|
| Rh/C | 0.1 M KOH + 0.1 M $KNO_3$ | | | 34.4 μg h $h^{-1}$ $cm^{-2}$ at 0.1 V | 20.8 | Indophenol blue method | $NH_3$ | | [189] |
| $Pt_{78}Ru_{22}$/C | 1 M $H_2SO_4$ + 1 M $NaNO_3$ | | | / | 93 | Indophenol blue method | $NH_3$, NO | | [208] |
| V-$TiO_2$ | 0.5 M $LiClO_4$ | RT | H-type | 17.73 μg $h^{-1}$ $mg_{cat.}^{-1}$ at −0.5 V vs. RHE | 15.3 | Indophenol blue method | | | [471] |
| Pd-Co/CuO | 0.1 M KOH | | | 10.04 μg·h−1·mg−1cat. at −0.2 V vs. RHE | 2.16 | | | alkaline | [204] |
| $CuCo_2O_4$/CFs | 1.0 M KOH +0.1 M $NO_3^-$ | | | 394.5 mmol $h^{-1}$ $g^{-1}$ | 81.9 | Indophenol blue method | $NH_3$, $NO_2^-$ | | [453] |
| N-C@NiO/GP | 0.1 M HCl | RT | | 14.022 μg·h−1·mg−1cat. at −0.2 V vs. RHE | 30.43 | | | acidic | [256] |
| 2H Rh NPLs | 1 M KOH + 1 M $KNO_3$ | | | 156.97 mg $h^{-1}$ $mg_{cat}^{-1}$ | 91.9 | Indophenol blue method and $^1H$ NMR | $NH_3$ | | [257] |
| Fe-$TiO_2$ | 0.5 M $LiClO_4$ | RT | H-type | 25.47 μg $h^{-1}$ $mg_{cat.}^{-1}$ at −0.4 V vs. RHE | 25.6 | Indophenol blue method | | | [396] |
| Co-FePS3 | 0.1 M KOH | | | 90.6 μg·h−1·mg−1cat. at −0.4 V vs. RHE | 3.38 | | | alkaline | [324] |
| Cu | 0.5 M $K_2SO_4$ + 50 mg $L^{-1}$ $NO_3^-$ | | | 778.6 μg $h^{-1}$ $mg^{-1}$ | 85.7 | Colorimetric method | $NH_3$, $NO_2^-$ | | [310] |
| SN Co-$Li^+$/PCNF | 0.5 M $Na_2SO_4$+ 0.5 M $NO_3^-$ | | | 2.1 mmol $h^{-1}$ $cm^{-2}$ | 90.2 | Indophenol blue method | $NH_3$, $NO_2^-$ | | [68] |
| $NiCo_2O_4$/CC A1 | 0.1 M NaOH + 0.1 M NaNO3 | | | 973.2 μmol $h^{-1}$ $cm^{-2}$ at -0.3 V | 99 | Colorimetric method | $NH_3$, $NO_2^-$ | | [172] |
| N- porous carbon | 0.05 M $H_2SO_4$ | RT | H-type | 1.40 mmol $g^{-1}$ $h^{-1}$ at −0.9 V vs. RHE | 1.42 | Nessler's reagent | | acidic | [258] |
| Ni—CuO | 0.5 M $Na_2SO_4$ +0.1 M $KNO_3$ | | | 0.94 mmol $h^{-1}$ $cm^{-2}$ | 95.26 | Indophenol blue method | $NH_3$ | | [311] |
| CoS2-N/S-C | 0.05 M H2SO4 | RT | | 25 μg·h−1·mg−1cat. at −0.05 V vs. RHE | 25.9 | | | acidic | [343] |
| Cu/PI | 0.1 M KOH | | | 12.4 μg·h−1·mg−1cat. −0.3 V vs. RHE | 6.56 | | | alkaline | [312] |
| BCDs/$NiCo_2O_4$/ carbon cloth | 0.5 M $K_2SO_4$ + 200 ppm $NO_3^-$ | | | 173.9 μmol $h^{-1}$ $cm^{-2}$ | ≈100 | Ion chromatograph | $NH_3$ | | [259] |
| NiWO4 | 0.1 M HCl | | | 40.05 μg·h−1·mg−1cat. at −0.3 V vs. RHE | 19.32 | | | acidic | [368] |
| CoP HNC | 1 M KOH | | | 10.78 μg·h−1·mg−1cat. at −0.4 V vs. RHE | 7.36 | | | alkaline | [344] |
| Cu-Pt | 0.1 M $Na_2SO_4$ +10 mM $NaNO_3$ | | | 194.4 mg $NH_3$- N $L^{-1}gcat^{-1}$ | 22 | Colorimetric method | $NH_3$ | | [302] |
| $Mn_3O_4$@rGO | 0.1 M $Na_2SO_4$ | RT | | 17.4 μg·$h^{-1}$·$mg_{cat.}^{-1}$ at −0.85 V vs. RHE | 3.52 | / | | neutral | [267] |
| $V_2O_4$ NW/rGO | .1 mol $L^{-1}$ $Na_2SO_4$ | RT | | 24.75 μg $h^{-1}$·$mg_{cat.}^{-1}$ at − 0.3 V vs. RHE | 79 | / | | neutral | [268] |
| $Cu_2O$/CP | 0.5 M $Na_2SO_4$ + 200 ppm $NaNO_3$ | | | 0.0699 mmol $h^{-1}$ $mg^{-1}$ | 85.26 | Colorimetric method | $NH_3$ | | [321] |
| FeS/Fe | 0.1 M KOH | | | 4.13 × $10^{-10}$ μg·h−1·mg−1cat. at −0.3 V vs. RHE | 17.6 | | | alkaline | [329] |
| Pd-$Cu_2O$ | 0.5 M $K_2SO_4$ + 50 ppm $KNO_3$ | RT | | 925.11 μg $h^{-1}$ $mg_{cat}^{-1}$ | 96.56 | Colorimetric method | $NH_3$ | | [322] |
| Fe-$MoS_{2-x}$ | - | RT | Back to back | 36.1 ± 3.6 mmol $g^{-1}$ $h^{-1}$ at −0.2 V vs. RHE | 31.6 ± 2 | Ion chromatography | | | [18] |
| ZIF- nitrogen-carbon | 0.1 M KOH | 25 °C | Single cell | 9.22 mmol $g^{-1}$ $h^{-1}$ at −0.3 V vs. RHE | 10.2 | Indophenol blue method | | alkaline | [130] |
| Cu@$Cu_{2+1}O$ | 0.5 M $K_2SO_4$ + 50 mg $L^{-1}$ $KNO_3$ | | | 576.53 μg $h^{-1}$ $mg_{cat}^{-1}$ | 87.07 | Colorimetric method | $NH_3$, $NO_2$ | | [314] |
| MOF-Fe | 2 M KOH | RT | | 2.12 × $10^{-9}$ μg·h−1·mg−1cat. at 1.2 V vs. RHE | 1.43 | | | alkaline | [23] |
| dendritic Cu | 0.1 M HCl | | | 25.63 μg·h−1·mg−1cat. at −0.4 V vs. RHE | 15.12 | | | acidic | [315] |
| $Cu_2O$/Cu | 1 M KOH +250 mg $L^{-1}$ $NaNO_3$ | | | 2.17 mg $cm^{-2}$ $h^{-1}$ | 84.36 | Indophenol blue method | $NH_3$, $NO_2^-$ | | [316] |

(*continued on next page*)

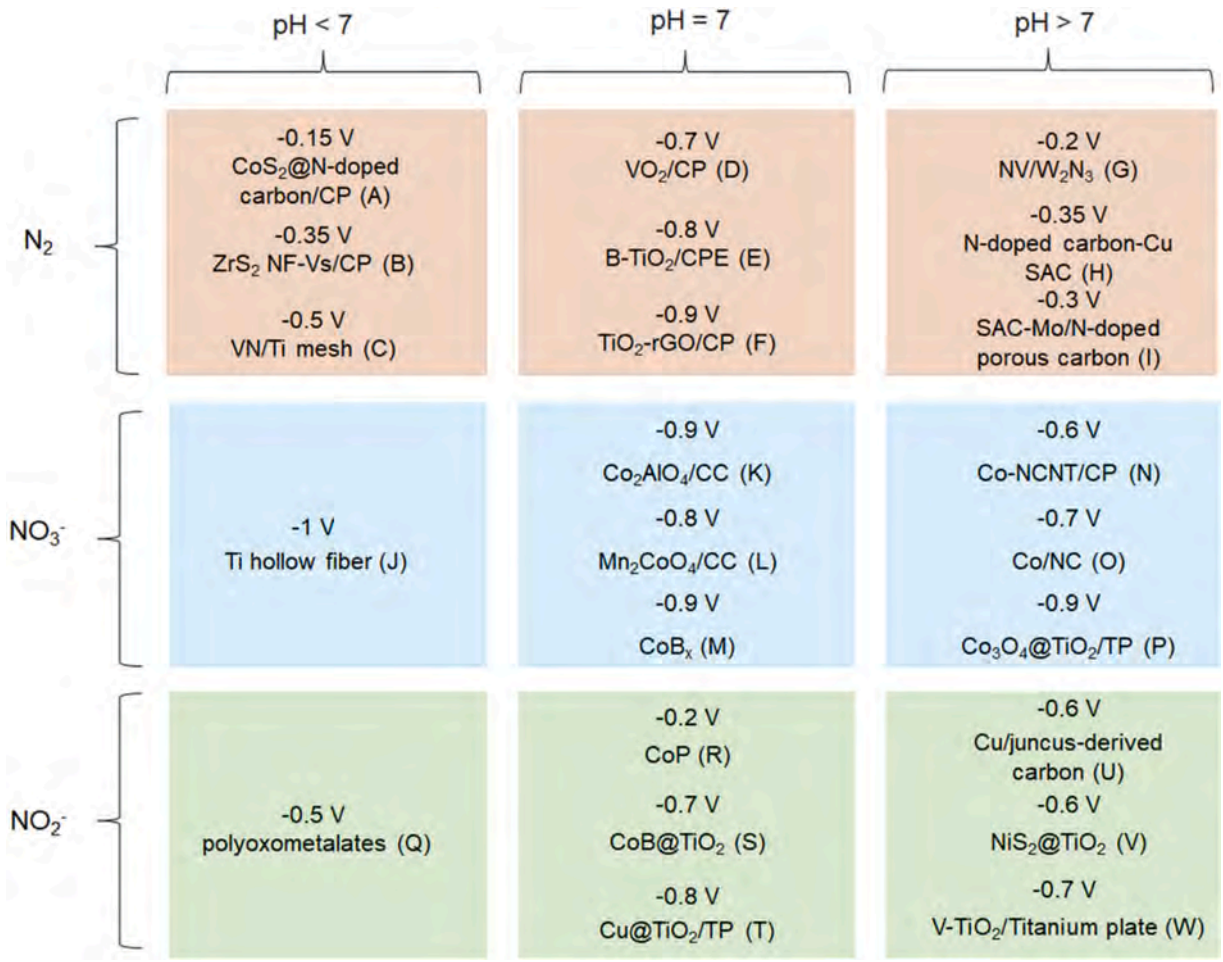
**Table 1** (*continued*)

| Name of Catalyst | Electrolyte | Temperature | Cell Type | $NH_3$ Yield Rate | FE (%) | Quantification Method | Product | Electrolyte Medium | Ref. |
|---|---|---|---|---|---|---|---|---|---|
| P-NiO/CC | 0.1 M Na2SO4 | | | 29.1 μg·h−1·mg−1cat. at −0.5 V vs. RHE | 10.8 | | | neutral | [185] |
| Fe-N/C-CNTs | 0.1 M KOH | RT | H-type | 34.83 μg·h−1·mg−1cat. at −0.2 V vs. RHE | 9.28 | | | alkaline | [325] |
| Co3O4@NC | 0.05 M H2SO4 | | | 42.58 μg·h−1·mg−1cat. at −0.2 V vs. RHE | 8.5 | | | acidic | [253] |
| NiO/G | 0.1 M Na2SO4 | | | 18.6 μg·h−1·mg−1cat. at −0.7 V vs. RHE | 7.8 | | | neutral | [373] |
| Cs/Ni-LaFeO3 | 2 M KOH | | | 13.46 μg·h−1·mg−1cat. at 2 V vs. RHE | 1.99 | | | alkaline | [460] |
| CoP/CNS | 0.1 M Na2SO4 | | | 48.9 μg·h−1·mg−1cat. at −0.4 V vs. RHE | 8.7 | | | neutral | [366] |
| Fe-$SnO_2$ | 0.1 M HCl | 25 °C | H-type | 82.7 μg $h^{-1}$ $mg_{cat.}^{-1}$ at −0.3 V vs. RHE | 20.4 | Indophenol blue method | | acidic | [338] |
| Au1Cu1 | 0.05 M H2SO4 | RT | | 154.91 μg·h−1·mg−1cat. at −0.2 V vs. RHE | 54.96 | | | acidic | [254] |
| O- carbon | 0.1 M HCl | RT | H-type | 25.12 μg $h^{-1}$ $mg_{cat.}^{-1}$ at −0.85 V vs. RHE | 9.1 | Indophenol blue method | | acidic | [276] |
| ISAS-Fe/NC | 0.1 M PBS | RT | | 62.9 μg·h−1·mg−1cat. at −0.4 V vs. RHE | 18.6 | | | neutral | [339] |
| Co-$MoS_2$ | 0.01 M $H_2SO_4$ | RT | | 0.63 mmol $g^{-1}$ $h^{-1}$ at −0.3 V vs. RHE | 10 | Nessler's reagent | | acidic | [350] |
| FePc/C | 0.1 M Na2SO4 | | | 137.95 μg·h−1·mg−1cat. at −0.3 v vs. RHE | 10.50 | | | neutral | [472] |
| γ-Fe2O3 | 0.1 M KOH | RT | | 12.5 μg·h−1·mg−1cat.at 0 V vs. RHE | 1.9 | | | alkaline | [473] |
| Fe/Fe3O4 | 0.1 M PBS | | | 0.19 μg·$cm^{-2}$·$h^{-1}$ at −0.3 V vs. RHE | 8.29 | | | neutral | [474] |
| Fe3S4 | 0.1 M HCl | RT | | 75.4 μg·h−1·mg−1cat. At −0.4 V vs. RHE | 6.45 | | | acidic | [475] |
| Ti/Fe3O4 | 0.1 M Na2SO4 | | | 5.6 × 10−11 mol·s−1·cm−2 at −0.4 V vs. RHE | 2.6 | | | neutral | [476] |
| N-S- graphene | 0.1 M HCl | RT | H-type | 7.7 μg $h^{-1}$ $mg^{-1}$ at −0.6 V vs. RHE | 5.8 | Indophenol blue method | | acidic | [477] |
| Fe2O3-rGO | 0.5 M LiClO4 | | | 22.13 μg·h−1·mg−1cat. at −0.5 V vs. RHE | 5.89 | | | neutral | [326] |
| o-Fe2O3-Ar/CNT | 0.1 M KOH | | | 0.46 μg·h−1·mg−1cat. at −0.9 V vs. RHE | 6.04 | | | alkaline | [332] |
| Fe2O3 | 0.1 M Na2SO4 | | | 15.9 μg·$h^{-1}$·$mg^{-1}$cat. at −0.8 V vs. RHE | 0.94 | | | neutral | [340] |
| LaFeO3 | 0.1 M HCl | RT | | 18.59 μg·h−1·mg−1cat. at −0.55 V vs. RHE | 8.77 | | | acidic | [470] |
| Fe2O3-CNT | KHCO3 | | | 2.2 × $10^{-3}$ g·$m^{-2}$·$h^{-1}$ at −2 V vs. RHE | | | | neutral | [279] |
| Cl-graphdiyne | 0.1 M HCl | RT | H-type | 10.7 μg $h^{-1}$ $cm^{-2}$ at −0.45 V vs. RHE | 8.7 | Indophenol blue method | | acidic | [273] |
| CoO/rGO | 0.1 M Na2SO4 | | | 21.5 μg·h−1·mg−1cat. at −0.6 V vs. RHE | 8.3 | | | neutral | [358] |
| N- graphitic carbon | 0.1 M HCl | RT | H-type | 0.08 g $h^{-1}$ $m^{-2}$ at −0.3 V vs. RHE | 5.2 | Indophenol blue method | | acidic | [58] |
| C@CoS@TiO2 | 0.1 M Na2SO4 | | | 8.09 ×$10^{-10}$ mol·$s^{-1}$·$cm^{-2}$ at −0.55 V vs. RHE | 28.6 | | | neutral | [405] |
| CoS2@NC | 0.1 M HCl | RT | | 17.45 μg·h−1·mg−1cat. At −0.15 V vs. RHE | 4.6 | | | acidic | [261] |
| NiCo2O4@HNCP | 0.1 M Na2SO4 | | | 17.8 μg·h−1·mg−1cat. at −0.25 V vs. RHE | 5.3 | | | neutral | [455] |

## 4. Structural Taxonomy of Catalysts

Electrocatalyst development for nitrate reduction is fundamentally guided by the need to maximize activity, selectivity, and operational stability through precise control of composition, structural features, and surface chemistry. A wide spectrum of materials including carbon-based frameworks, semiconductors, metallic compounds, and composite architectures has been explored for their ability to facilitate the complex multi-electron transfer processes required for efficient $NH_3$ generation [119–121]. The catalytic performance is intimately connected to intrinsic physicochemical properties such as specific surface area, electrical conductivity, crystallographic arrangement, and the availability of exposed active sites [122–125]. High-surface-area materials play a critical role by enhancing the interaction between reactants and active sites, thereby promoting efficient charge transport and improving overall reaction kinetics. Graphene, for instance, exhibits remarkable electrical conductivity, thermal stability, and a theoretical surface area exceeding 2600 $m^2$ $g^{-1}$, enabling rapid electron mobility and effective stabilization of reaction intermediates. One-dimensional nanostructures, such as carbon nanotubes, extend electron pathways and provide tunable morphologies, while their curvature and defect density can further influence adsorption energies of nitrate and its intermediates [126,127].

The crystallographic phase and bonding environment are also decisive factors influencing catalytic efficiency. Differences in hybridization, such as those between graphite-like and diamond-like structures, modulate electron density distribution and redox characteristics. Surface functionalization through heteroatom doping, with elements like




**Scheme 1.** Reduction potentials (vs. RHE) of various nitrogen sources at different pH values. CP, CC, and NF denote carbon paper, carbon cloth, and nickel foam, respectively. Reproduced with permission from [100].

boron or nitrogen, or the creation of defects can strategically modify the local electronic environment, optimize the adsorption of reactive species, and suppress parasitic reactions, including hydrogen evolution [128–130]. Semiconductor-based materials, including polymeric graphitic carbon nitride and related frameworks, offer intrinsic stability and favorable band structures for electrocatalysis [131]. However, challenges such as limited surface area or strong hydrogen adsorption often necessitate additional structural or compositional engineering [132]. Approaches such as introducing vacancies, creating porous architectures, or integrating conductive supports can significantly enhance charge transfer and improve overall catalytic efficiency.

No single material class universally dominates performance. Rather, the most effective electrocatalysts arise from combining high-conductivity frameworks, abundant active site exposure, tailored surface chemistry, and structural robustness. Metal-based semiconductors, for example, provide high intrinsic activity and the ability to stabilize reactive intermediates through tunable oxidation states and surface terminations, whereas carbon-based systems offer economic and environmental advantages along with long-term stability [133–136]. Composite and heterostructure designs, including p–n junctions, type-II or Z-scheme architectures, and plasmonic metal-semiconductor hybrids, deliver synergistic benefits such as improved charge separation, suppressed recombination, and enhanced light or electron harvesting, although reliance on noble metals can limit scalability [137–142]. Fig. 5 presents the structural diversity of these catalytic materials, highlighting representative examples from each category. Collectively, the strategic design and integration of carbon-based, metal-based, and heterostructured catalysts enable a synergistic balance of conductivity, active site availability, and structural robustness. Such an approach is essential for optimizing electron transfer pathways, intermediate stabilization, and reaction selectivity, advancing the development of high-performance, sustainable systems for e-$NO_3$RR and associated energy conversion reactions [134,143]. Further detailed discussion on each category of catalysts will be presented in the subsequent sections.

## 5. Cutting-Edge Characterization Approaches

The structural configuration of the electrode plays a pivotal role in the nitrate e-$NO_3$RR, directly influencing the distribution and accessibility of active sites that govern the reaction pathway. To elucidate these structural features and gain insights into catalytic activity, a range of advanced analytical methods has been employed. Techniques such as Raman spectroscopy [144], X-ray photoelectron spectroscopy (XPS) [145], aberration-corrected scanning transmission electron microscopy (AC-STEM) [146], X-ray absorption spectroscopy (XAS) [147], transmission electron microscopy (TEM) [148], and scanning electron microscopy (SEM) [149] provide complementary information on composition, crystallinity, and morphology [150].

***5.1. Ultraviolet–Visible Spectroscopic Analysis***: For quantifying nitrate ions, ultraviolet-visible spectroscopy remains a standard approach, although its sensitivity at low concentrations is limited and typically requires the addition of a chromogenic agent [151]. The use of such agents is critical for enabling light absorption at ~220 nm, facilitating accurate $NO_3^-$ detection. Colorimetric methods, including the

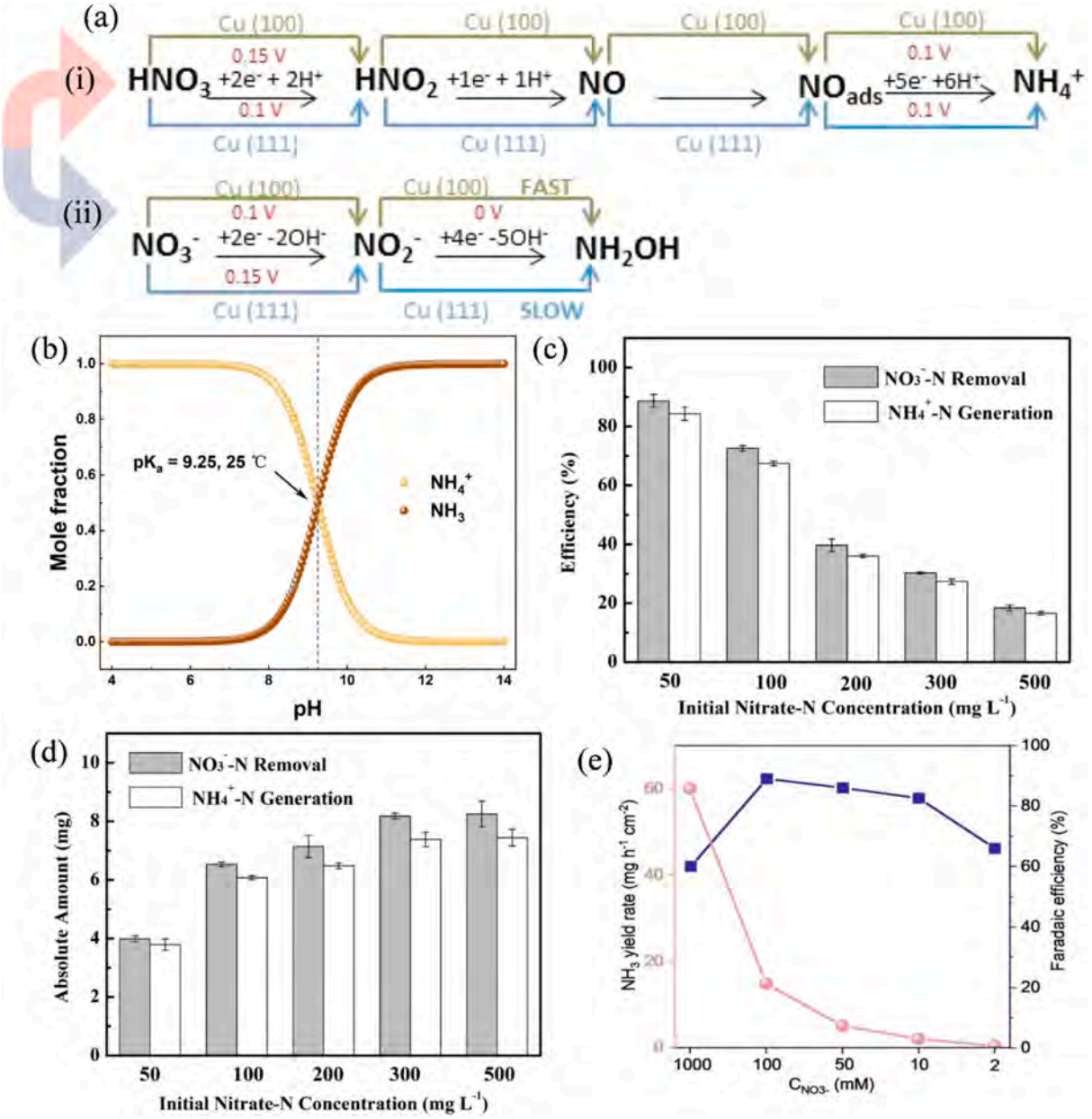



**Fig. 4.** (a) Mechanistic pathways of nitrate electroreduction on copper single-crystal electrodes under (i) acidic and (ii) alkaline conditions. (b) Variation in the relative abundance of $NH_3$ and $NH_4^+$ species with solution pH at 25 °C. (c) Influence of the initial $NO_3^-$–N concentration on nitrate removal efficiency and ammonium formation selectivity. (d) Quantitative analysis of $NO_3^-$–N conversion and $NH_4^+$–N production on the $Co_3O_4$/T cathode. (e) Dependence of $NH_4^+$–N yield rate and FE on starting nitrate concentration using the Rh@Cu-0.6% cathode. Reproduced with permission from [79,102–104].

indophenol blue and Nessler's reagent assays, are widely employed to determine nitrate concentrations and validate $NH_3$ production [152].

***5.2. X-ray Absorption Spectroscopy***: XAS has emerged as a pivotal technique for elucidating the electronic and atomic-scale structure of electrocatalysts under working conditions. By analyzing the X-ray absorption near-edge structure (XANES) and extended X-ray absorption fine structure (EXAFS) regions, researchers can extract valuable insights into oxidation states, local coordination, and bond environments of the absorbing atoms [153]. These measurements typically performed using synchrotron radiation with monochromators and high-sensitivity detectors, which can be integrated with electrochemical testing to establish direct correlations between active site evolution and catalytic performance. For instance, XAS has been used to track the geometric and electronic restructuring of copper-based catalysts during nitrate electroreduction, revealing potential-dependent transitions from atomically dispersed Cu–$N_4$ sites to metallic Cu nanoparticles, which were found to enhance $NH_3$ selectivity [154]. In Cu–Ni alloys, operando XAS demonstrated that Ni incorporation modulates the Cu d-band center, thereby tuning intermediate adsorption energies and boosting activity [155,156]. Similarly, in Ru-Cu nanowire systems, in situ XAS confirmed complete reduction of both metals to their metallic states and atomic-level Ru dispersion, which contributed to exceptional current densities and FE in industrially relevant nitrate concentrations [157].

The versatility of XAS extends beyond nitrate reduction. For nitrogen reduction reactions, operando measurements on Fe-Pd single-atom alloys revealed Fe-N coordination changes and bond distortions during $N_2$ activation, while Pd remained electronically inert. In C-N coupling reactions for urea synthesis, in situ XANES identified $Bi^{2+}$ species in Sb-doped $BiO_x$ clusters as the active phase, stabilized by Sb to prevent structural degradation [158]. Across these studies, operando XAS has

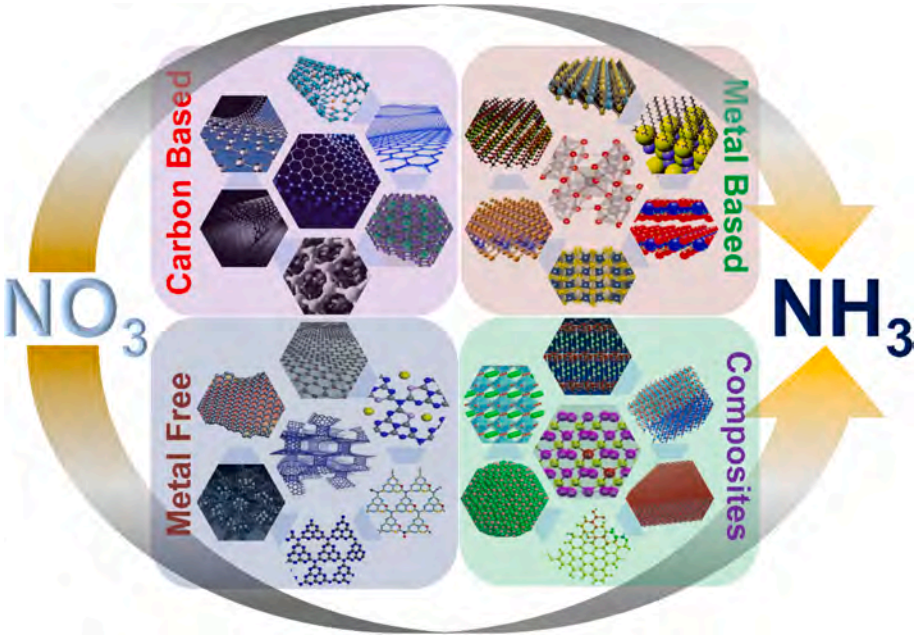



**Fig. 5.** Comprehensive evaluation of catalyst families relevant to nitrate reduction is presented.

proven indispensable for revealing structure-performance relationships and guiding the rational design of catalysts with optimized active site configurations.

***5.3. Operando Raman Spectroscopy, Real-Time Insights*:** Raman spectroscopy, particularly in its operando configuration, enables real-time monitoring of molecular vibrations, surface reconstructions, and transient intermediates under actual reaction conditions. This capability is essential for elucidating the mechanisms of complex multi-electron reactions such as electrochemical nitrogen reduction (e-NRR) and e-$NO_3$RR, where catalytic performance depends on short-lived active species and dynamic site chemistry [159]. Oxygen-vacancy-enriched $MoO_{3-x}$/MXene catalysts exhibited a distinct Mo-N stretching mode (~835 $cm^{-1}$) during $N_2$ exposure, indicating vacancy-induced chemisorption and activation that lowered the hydrogenation energy barrier (Fig. 6a-d) [160]. Tailoring annealing atmospheres effectively tuned vacancy density, directly enhancing e-NRR activity. Electrolyte engineering, such as the use of concentrated water-in-salt systems, intensified N-metal interactions while suppressing competing hydrogen evolution. Detection of –$NH_2$ and –NH intermediates under $N_2$-saturated conditions confirmed genuine nitrogen activation pathways [161].

Operando Raman also revealed in situ structural transformations, such as the electrochemical fragmentation of bismuth-based species into metallic nanoparticles, which improved *NNH adsorption and catalytic rates [164]. Oxidation-state modulation further optimized electronic structures, promoting stronger reactant binding and accelerating RDS, as supported by DFT analysis [165]. In $NO_3$RR, reversible CuO↔$Cu_2O$ phase transitions were identified under applied bias (Fig. 6e), with mixed-phase active sites driving high ammonium yields [162]. Alloy catalysts demonstrated superior nitrate adsorption and efficient $NO_2^-$ hydrogenation, while dopant-modified phosphides optimized active site electronic states for a cascade hydrogenation pathway [163]. In $CO_2$–$NO_3^-$ co-reduction systems, carbonate (*$CO_3^{2-}$) and CO (*CO) intermediates were detected, confirming their role in C-N coupling to urea formation (Fig. 6f-g). Operando Raman spectroscopy provides unparalleled insight into the identification of active sites, detection of key intermediates, and observation of structural dynamics, offering a powerful platform for the rational design of catalysts in $NH_3$ synthesis, nitrate valorization, and C–N bond formation [166].

***5.4. Real-Time IR Monitoring:*** Infrared (IR) spectroscopy is a powerful operando tool for probing molecular vibrations and adsorbed intermediates on electrocatalyst surfaces in real time. By capturing dynamic changes in chemical bonds during electrochemical reactions, IR spectroscopy provides mechanistic insight into multi-step processes such as e-NRR, e-$NO_3$RR, and $CO_2$–$NO_3^-$ co-reduction, enabling the identification of transient species and active sites [167]. Time-resolved IR studies reveal the stepwise formation of nitrogenous intermediates. On Ag–Ni nanocatalysts, characteristic bands at ~1320, 1475, and 1582 $cm^{-1}$ correspond to *$N_2H_y$ species and $NH_4^+$, demonstrating the progressive hydrogenation of $N_2$ (Fig. 7a) [168]. Electrolyte composition significantly affects surface activation; water-in-salt electrolytes enhance *$NH_x$ formation, while dilute electrolytes show weaker signals, indicating less efficient $N_2$ activation [161]. Similarly, $H^+$-permeable COF layers on boron-doped carbon substrates amplify N–H vibrational signals under negative bias, highlighting their ability to promote e-NRR activity [169].

ATR-IR setups, using a thin metal-coated prism as the working electrode, allow in situ detection of adsorbed intermediates. For $NH_3$ oxidation on Pt electrodes, IR spectra trace the evolution of $NH_3$, $N_2H_4$, and NO species as a function of applied potential, confirming the involvement of $N_2H_4$ as a key intermediate [173]. In nitrate reduction, in situ FTIR studies on CoP-CNS and CuCo catalysts reveal the stepwise reduction of $NO_3^-$ to $NO_2^-$, $NH_2OH$, and $NH_3$, with Co enhancing hydrogenation via surface H* provision (Fig. 7b). Synergistic Cu–Co sites lower energy barriers for intermediate conversion, achieving high FE and selectivity [81,170]. IR spectroscopy also elucidates co-reduction processes. Fe–Ni diatomic catalysts activate $NO_3^-$ and $CO_2$ simultaneously, facilitating C-N coupling for urea formation (Fig. 7c). Bands assigned to *NH, *NHCO, and *NO species grow with negative potential, directly correlating with catalytic performance, and revealing the sequence of bond formations leading to urea [171]. Operando IR spectroscopy provides a direct window into the evolution of intermediates, active sites, and reaction pathways, guiding the rational design of high-performance electrocatalysts for $NH_3$, nitrate, and urea synthesis.

***5.5. Differential electrochemical mass spectrometry (DEMS):*** DEMS is a powerful in situ analytical tool that enables real-time, mass-resolved detection of gaseous and volatile species formed during electrochemical reactions [174]. By correlating faradaic currents with ion mass signals, DEMS allows direct identification of reaction intermediates and products, thereby clarifying ambiguous mechanistic pathways. The technique is particularly valuable for e-NRR and nitrate/

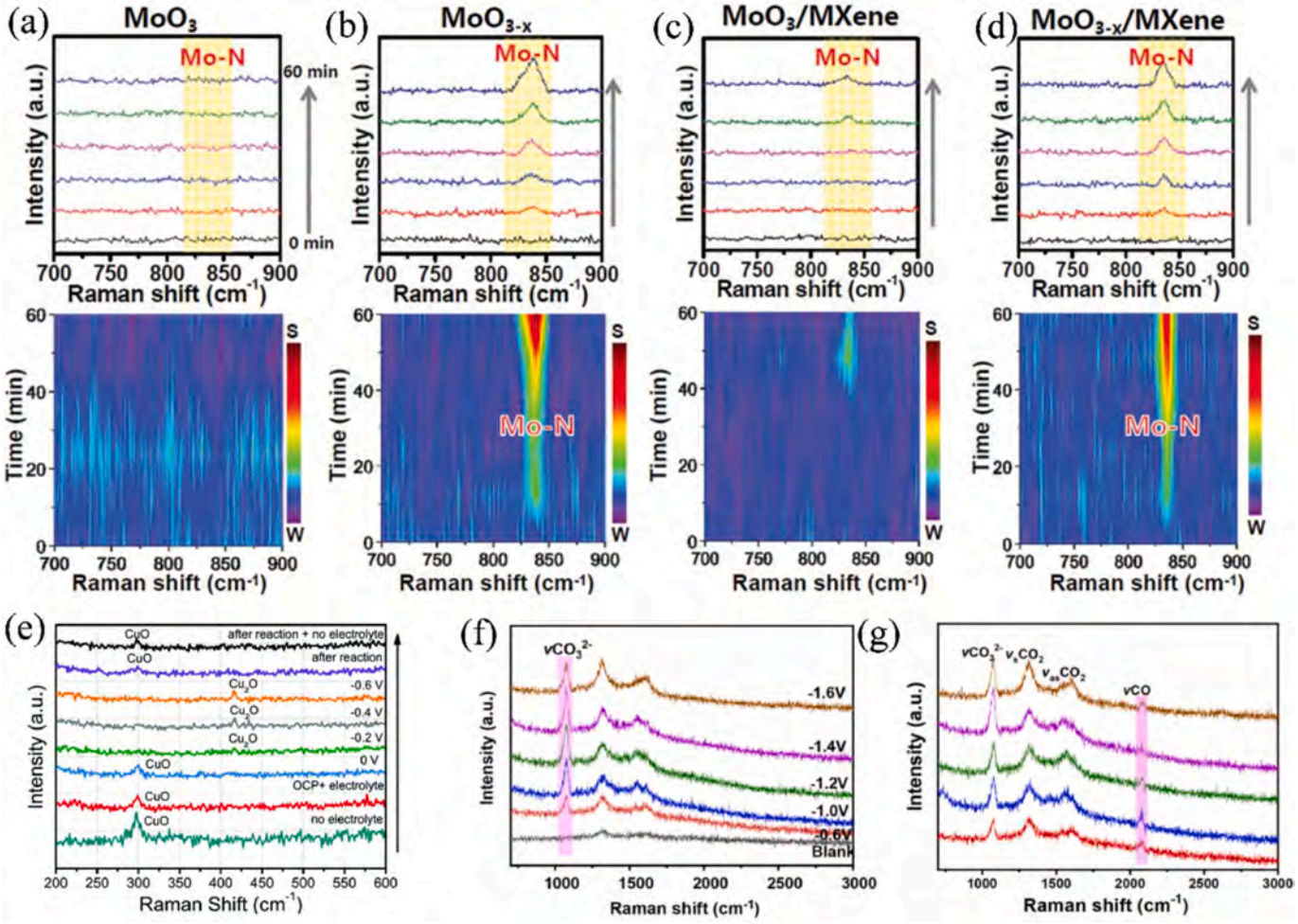



**Fig. 6.** (a–d) Two dimensional Raman spectral maps of multiple catalysts recorded during e-NRR electrolysis at −0.4 V, accompanied by corresponding contour representations (bottom panels). (e) Operando Raman spectra of pCuO-5 deposited onto a screen-printed microelectrode under varying experimental conditions and applied potentials. From bottom to top: Raman measurements at open-circuit potential (OCP) without electrolyte, OCP in 0.05 M $KNO_3$ + 0.05 M $H_2SO_4$ electrolyte, under applied potentials within the electrolyte, and post-reaction OCP without electrolyte. (f) Time-resolved Raman signatures captured during the electrocoupling of $NO_3^-$ and $CO_2$, and (g) Raman responses recorded during $CO_2$RR electrocoupling. Reproduced with Permission from [160,162,163].

nitrite reduction (e-$NO_3$RR/$NO_2$RR), where multiple competing pathways and short-lived intermediates often complicate product assignment [175]. For example, selective nitrite reduction to $N_2$ on Pt(100) surfaces has been demonstrated, with DEMS revealing product formation at distinct potentials, separating pathways to $N_2$ and $NH_3$ [176]. Similarly, Cu-based catalysts for nitrate reduction have been studied using DEMS to identify intermediates (*$NO_3$, *$NO_2$, *NOH, *$NH_2OH$) and validate stepwise hydrogenation routes toward $NH_3$, while suppressing competing hydrogen evolution [17,28].

In $CO_2$-nitrate co-reduction systems, DEMS has clarified whether $N_2$ or $NH_3$ participate in C-N coupling during urea synthesis. For $CuWO_4$, signals for $CO_2$, CO, $N_2$, and $NH_3$ confirmed a direct coupling mechanism between *CO and *$NO_2$ without $N_2$/$NH_3$ intermediacy, whereas oxygen-deficient ZnO showed urea formation from *CO and *$NH_2$ precursors [177,178]. For e-NRR, operando DEMS has resolved transient species such as $N_2H_4$ and $N_2H_x$ on catalysts like Bi nanoparticles and Rh/C, revealing potential-dependent pathways involving two-electron transfers followed by chemical decomposition. Complementary operando FTIR has confirmed the presence of N=N stretching and N–H vibrational bands, linking e-NRR and nitrate reduction through common intermediates [179]. DEMS serves as a critical mechanistic probe in electrocatalytic nitrogen chemistry, offering unparalleled capability to directly detect, quantify, and temporally resolve volatile intermediates under realistic operating conditions.

***5.6. Further Analytical Approaches*:** Advanced electrochemical characterization techniques are essential for revealing the structure-activity relationships of electrocatalysts and guiding the rational design of high-performance materials for nitrate and nitrogen reduction reactions. Scanning electrochemical microscopy (SECM) provides localized mapping of surface reactivity and topography with nanometer-scale resolution. By operating in modes such as scanning generation–tip collection and surface interrogation, SECM enables in situ detection of reaction products and quantification of active sites, offering valuable mechanistic insights into interfacial processes [180]. Electrochemical quartz crystal microbalance (EQCM) complements SECM by measuring real-time mass variations at the electrode-electrolyte interface through frequency shifts of a vibrating quartz crystal [181]. This approach links surface mass changes to adsorption, desorption, or restructuring events. For example, during nitrate reduction on copper electrodes, EQCM has revealed the buildup of surface-bound intermediates that inhibit further reaction, while anodic pulsing effectively regenerates active sites [182]. Vibrational sum-frequency generation spectroscopy offers interface-specific molecular information by combining visible and infrared laser excitations to detect vibrational signatures of adsorbed species under reaction conditions. This technique has been used to confirm the role of oxygen vacancies in cerium oxide catalysts, where such sites stabilize key intermediates and promote C-N coupling during urea synthesis [183–185].

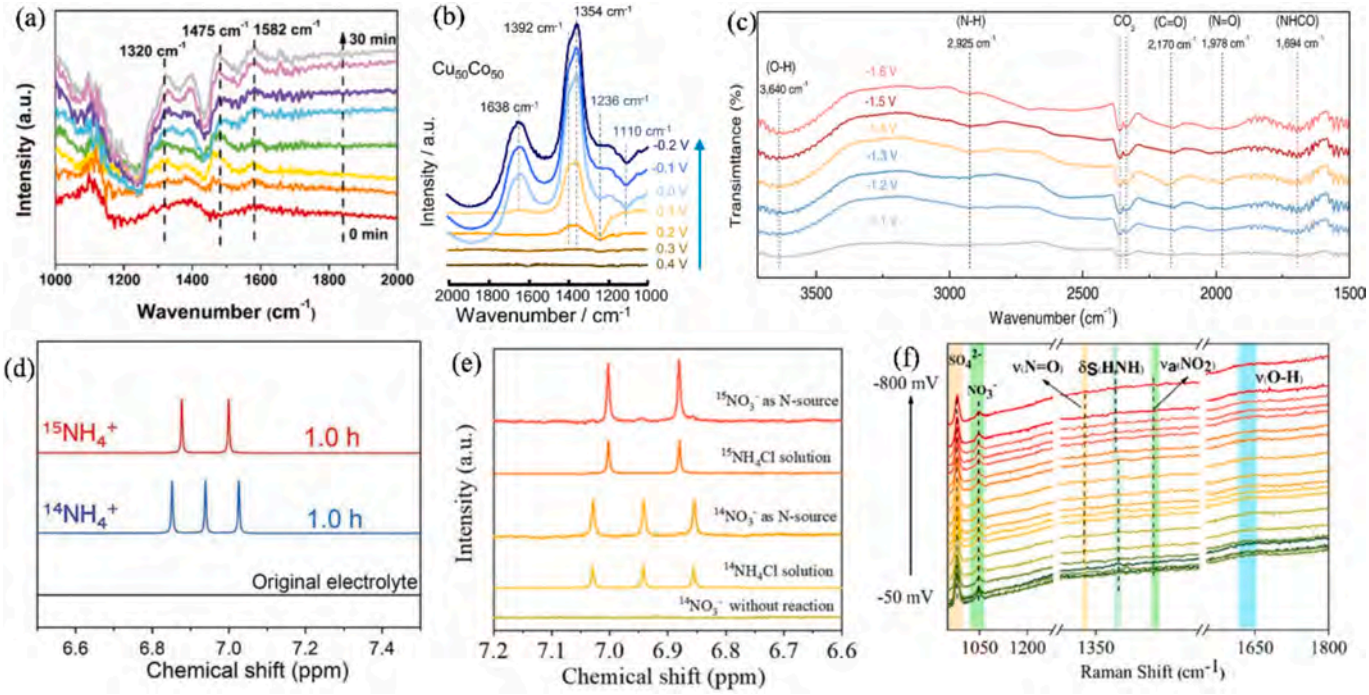



**Fig. 7.** (a) In situ FTIR measurements of $Ag_4Ni_2$ nanoclusters conducted at −0.2 V. (b) Electrochemical thin-layer in situ FTIR spectra capturing $NO_3^-$RR behavior on $Cu_{50}Co_{50}$ catalysts. (c) IR responses within 1500–3750 $cm^{-1}$ under varying applied potentials for B-FeNi-DASC during the electrocoupling of nitrate and $CO_2$. (d) $^1H$ NMR spectra of electrolytes post-e$NO_3$RR using $^{15}NO_3^-$ and $^{14}NO_3^-$ as nitrogen isotopic sources. (e) $^1H$ NMR spectra recorded with $^{14}NO_3^-$ and $^{15}NO_3^-$ reactants to trace nitrogen incorporation. (f) In situ Raman spectra spanning 900-1800 $cm^{-1}$ recorded at potentials from −0.05 to −0.8 V on $Fe_2O_3$ nanorods supported on carbon cloth (CC) in 0.5 M $Na_2SO_4$ and 0.1 M $NaNO_3$ electrolytes. Reproduced with permission from [144,168,170–172].

In situ electron paramagnetic resonance (EPR) spectroelectrochemistry provides complementary mechanistic insights by detecting transient radical species formed during electrochemical reduction. Optimized electrode configurations allow sensitive monitoring of these intermediates under operational conditions, revealing the role of reactive hydrogen species in product selectivity [186]. Accurate identification of nitrogen sources in $NH_3$ products is vital for validating nitrate reduction pathways. Isotopically labeled nitrate ($15NO_3^-$) combined with $^1H$ NMR spectroscopy can distinguish $^{15}NH_4^+$ from $^{14}NH_4^+$, confirming the genuine nitrogen origin (Fig. 7d-e) [144,172]. In situ Raman spectroscopy further supports mechanistic studies by non-invasively detecting intermediates such as nitrate, nitrite, and amide groups directly on catalyst surfaces during operation (Fig. 7f) [144,172]. The integration of these operando spectroscopic, microscopic, and electrochemical techniques with DFT simulations provides a comprehensive understanding of adsorption energetics, electronic structure modifications, and intermediate transformation pathways. This combined approach is pivotal for advancing the design of efficient, selective, and durable catalysts for sustainable nitrate and nitrogen electroreduction.

## 6. DFT Calculations

DFT has become an essential computational tool for unraveling the mechanistic pathways of complex electrocatalytic processes such as the e-$NO_3$RR and e-NRR. These reactions involve multi-electron transfer steps and numerous surface intermediates, making experimental analysis alone insufficient to fully capture reaction dynamics. By providing atomistic-level insights into intermediate adsorption, activation energies, and reaction energetics, DFT enables rational catalyst design to improve activity, selectivity, and suppression of competing reactions such as the HER. When coupled with in situ characterization techniques, DFT allows a more comprehensive understanding of the reaction mechanisms under realistic operating conditions, bridging the gap between theory and experiment [187–189].

In e-$NO_3$RR, DFT calculations have been extensively applied to determine Gibbs free-energy profiles for each elementary step, elucidating the energy barriers for the formation and hydrogenation of key intermediates such as *NO, *NOH, and *$NH_2$OH [193]. For example, Cu@Cu-CuO catalysts synthesized via electrochemical reconstruction exhibit a favorable energy landscape, where the conversion of $NO_{ads}$ to $NOH_{ads}$ proceeds with minimal energy input, and subsequent hydrogenation steps are energetically facilitated compared to pure Cu surfaces [194,195]. Similarly, 10Cu/$TiO_{2-x}$ electrodes demonstrate enhanced $NO_3^-$ adsorption and dissociation, which promote nitrate reduction while suppressing HER, highlighting the importance of surface defects and oxygen vacancies in modulating catalytic activity [196]. These studies illustrate how DFT-guided insights into potential-dependent steps and intermediate stabilization can inform the rational design of electrodes to optimize e-$NO_3$RR performance. In the context of e-NRR, DFT calculations provide critical understanding of $NH_3$ synthesis mechanisms by constructing free-energy diagrams, identifying potential-limiting steps, and analyzing adsorption energies of surface intermediates. Transition metals (Mo, Fe, Rh, Ru) and their oxides, as well as single-atom catalysts and metal-free materials, have been systematically evaluated for $N_2$ activation, hydrogenation, and $NH_3$ desorption. Computational studies reveal that electronic structure modulation, heteroatom doping, and defect engineering significantly influence the adsorption of $N_2$ and intermediates while mitigating HER competition. For instance, Mo dispersed on $WS_2$ or loaded on defective $BC_2N$ monolayers exhibits low overpotentials (0.36–0.44 V) for e-NRR via enzymatic or associative pathways (Fig. 8a-b) [190,197]. Moreover, hydride-transfer mechanisms on α-PdH and vacancy-assisted activation on $Bi_2O_{3-x}$ surfaces demonstrate alternative reaction pathways that enhance $N_2$ conversion efficiency (Fig. 8c) [191]. Ab initio molecular dynamics and nudged elastic band analyses further confirm catalyst stability and feasibility under realistic reaction conditions (Fig. 8d-e) [192]. DFT studies also enable the development of predictive models, such as volcano plots and scaling relationships, which correlate

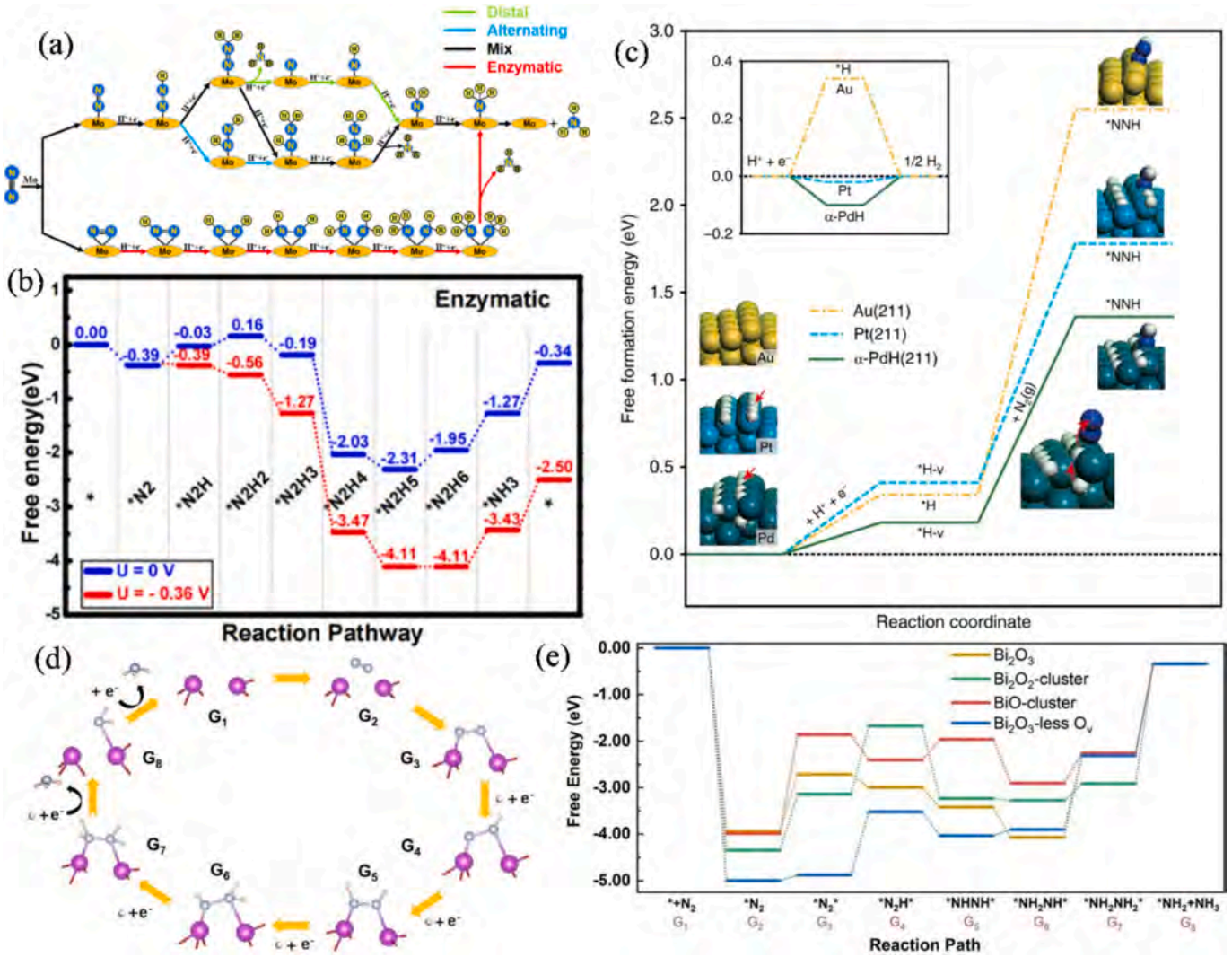



**Fig. 8.** (a) Illustration of the multiple electrocatalytic nitrogen reduction pathways on Mo@$WS_2$. (b) Gibbs free-energy landscape depicting enzymatic reaction trajectories. (c) DFT-derived free energy profiles for HER (inset) and $N_2$RR intermediates on the (211) facets of Au, Pt, and α-PdH at 0 V vs. RHE and 298.15 K, with corresponding atomic configurations shown as insets. The initial step involves *H formation on Au and *H vacancy (H-v) creation on Pt and α-PdH step sites. The subsequent step represents direct surface hydrogenation of $N_2$ to generate $N_2H$ on Au and Pt, whereas a Grotthuss-type hydride transfer occurs on α-PdH. (d) Schematic representation of the eight-step catalytic cycle at dual Bi active sites. (e) Computed reaction energy profiles for sequential $N_2$ fixation steps catalyzed by $Bi_2O_3$ and unsaturated $BiO_x$ clusters. Reproduced with permission from [190–192].

intermediate adsorption energies with overall catalytic performance [198,199]. These approaches, grounded in the Sabatier principle, help identify optimal catalyst-intermediate interactions that balance reactant activation with product desorption. Computational insights into Lewis-base interactions, vacancy effects, and electronic orbital coupling provide additional guidance for tuning active sites at the atomic scale [200,201]. By integrating DFT with experimental data, researchers can accelerate high-throughput screening of catalysts, leading to the discovery of novel materials with enhanced electrocatalytic efficiency, selectivity, and durability.

## 7. Advanced Materials for Electrochemical Nitrate to Ammonia Reduction

The advancement of electrochemical nitrate-to-$NH_3$ conversion relies heavily on the rational design of catalysts, where material architecture dictates efficiency, selectivity, and durability. Tailored modifications in electronic structures, defect engineering, and surface chemistry across metals, alloys, oxides, and emerging low-dimensional frameworks have proven effective in lowering reaction barriers while mitigating side reactions. The degree of crystallinity critically influences the $NH_3$ synthesis efficiency of catalytic materials by modulating the density of active sites, defect concentration, and charge transport characteristics. Generally, lower crystallinity introduces structural defects such as vacancies, edges, and disordered regions that act as active centers for $N_2$ adsorption and activation, thereby facilitating the cleavage of the N≡N triple bond and enhancing $NH_3$ formation [202]. However, this crystallinity–activity relationship differs between metallic and non-metallic systems. In metallic catalysts, higher crystallinity ensures superior electrical conductivity and stability, essential for efficient electron transfer, whereas excessive amorphization can lead to charge recombination and reduced durability. Conversely, in non-metallic or carbon-based catalysts, lower crystallinity or controlled disorder is often beneficial, as defect engineering and heteroatom doping create abundant active sites and improve proton-coupled electron transfer. Therefore, while high crystallinity favors performance in metallic systems, moderately disordered or defect-rich structures are more promising for non-metallic catalysts, such as amorphous carbon, highlighting that an optimal degree of crystallinity is key to achieving high $NH_3$ synthesis efficiency [203]. Incorporation of heterostructures, single-atom sites,

and conductive scaffolds has further enhanced charge transport and active site utilization, enabling promising FEs and industrially relevant current densities. In this section, we will thoroughly discuss carbon-based electrocatalysts, non-noble metal-based materials, metal oxide-based materials, and noble metal-based materials for electrochemical nitrate-to-$NH_3$ conversion.

### 7.1. Noble Metal-based Materials

Noble metals stand out as highly effective electrocatalysts owing to their distinctive electronic configurations, which enable strong interaction with reactants and efficient stabilization of reaction intermediates [204]. Their inherent resistance to heat, oxidation, and corrosion further enhances their durability under harsh electrochemical conditions. Within the nitrate reduction reaction, noble metals display markedly different catalytic behaviors depending on their elemental composition. Ruthenium (Ru) has been shown to deliver exceptional activity and selectivity for $NH_3$ synthesis under mild conditions, while palladium achieves high yields through efficient $NO_3^-$ → $NH_3$ conversion. Silver also demonstrates strong performance, offering both high conversion efficiency and product selectivity. These insights emphasize the strategic importance of noble metals in tailoring advanced catalytic systems for sustainable nitrate reduction [205–208]. Accordingly, this section will provide a broad discussion on the role of noble metals as catalysts in facilitating the electrochemical conversion of $NO_3^-$ → $NH_3$.

**7.1.1. Ru based catalyst**: Ru has emerged as a premier choice among noble-metal catalysts for e-$NO_3$RR, owing to its remarkable combination of intrinsic activity, electrical conductivity, and resistance to corrosion and thermal stress. Compared with Pt, Pd, and Ir, Ru not only exhibits superior catalytic efficiency for e-$NO_3$RR but also offers a more cost-effective and sustainable alternative. Its exceptional performance arises from the strong adsorption of nitrate ions on the Ru surface, facilitating efficient reduction pathways while minimizing competing reactions such as the HER [88,206]. Tuning the structural attributes of Ru at the nanoscale significantly enhances its catalytic behavior. Sub-nanometer Ru clusters, particularly those engineered with tensile strain, have demonstrated remarkable activity. Jie et al. reported 2 nm Ru nanoclusters prepared via sol–gel synthesis of ruthenium oxychlorides followed by electrochemical reduction [155]. The incorporation of oxygen in the subsurface induced lattice strain, adjustable by oxygen content, which modulated hydrogen adsorption and promoted intermediate hydrogenation (Fig. 9a-b). Among these, Ru-ST-12 with 12% strain achieved a peak $NH_3$ yield of 1.17 ± 0.04 mmol $h^{-1}$ $cm^{-2}$ (5.56 mol $g_{cat.}^{-1}$ $h^{-1}$) with >96% FE at 0.2 to −0.2 V (vs. RHE), maintaining performance over 100 h (Fig. 9c). This strain suppressed HER by limiting hydrogen dimerization while accelerating *H-mediated nitrate conversion. The interplay between Ru and its support is another critical determinant of performance. Jinhui et al. developed Ru nanoclusters on phosphorus-doped, oxygen-vacancy-rich $Fe/Fe_3O_4$ nanorods (Ru@P-$Fe/Fe_3O_4$), which achieved $NH_3$ FE of ~97.2% and NH3 yield of 8.32 ± 0.12 mg $h^{-1}$ $cm^{-2}$ over 50 cycles at −0.55 V (vs. RHE) (Fig. 9d-e) [209]. DFT studies indicated that strong metal-support interactions facilitated oxygen vacancy formation, adjusted Ru electronic states, and lowered reaction barriers, while suppressing HER (Fig. 9f-g).

Single-atom Ru catalysts offer a pathway toward maximal atomic efficiency and highly tunable electronic environments [211]. Yancai et al. anchored Ru atoms on $TiO_x$/Ti foam, achieving an $NH_3$ yield of 22.2 mol $g^{-1}$ $h^{-1}$ with 87.6% FE at −0.3 V (vs. RHE) [212]. Feng et al. incorporated Ru into Cu nanowires (Ru-CuNW), realizing industrial-scale $NH_3$ production (~1 A $cm^{-2}$) with 93% FE and over 100 h of stable operation [118]. The DFT results highlighted that dispersed Ru provided active sites for nitrate reduction, while adjacent Cu suppressed HER. Structural engineering also plays a pivotal role in enhancing Ru catalysis. Amorphous Ru clusters and nanosheets present abundant low-coordinate sites and flexible atomic arrangements that outperform crystalline counterparts. For instance, Yuting et al. synthesized amorphous $RuO^2$ nanosheets on carbon paper, yielding $NH_3$ FE of 97.46% and selectivity of 96.42%, far surpassing low- or high-crystallinity $RuO_2$ [193]. Minghang et al. demonstrated ultrafine amorphous Ru clusters (~1.2 nm) on carbon nanotubes, exhibiting higher $NH_3$ yields and FE than crystalline analogs due to more accessible active sites [213]. Alloying Ru with other metals further enhances performance through electronic modulation, lattice strain effects, and synergistic interactions [214,215]. RuCu alloys on reduced graphene oxide exploit a relay mechanism as demonstrated by Gao et al [210]. Cu efficiently converts $NO_3^-$ to $NO_2^-$, while Ru catalyzes $NO_2^-$ to $NH_3$, with TEM and FT-EXAFS confirming atomic-level Ru incorporation in Cu matrices. Bader charge analysis shows 0.77 e transfer from Cu to Ru in the RuCu alloy, optimizing $NO_3^-$/$NO_2^-$ adsorption compared to individual metals (Fig. 9h). In e-$NO_3$RR, Cu encounters its potential-determining step (PDS) at *NO → *N (ΔG = 0.79 eV), whereas Ru binds *$NO_3$ strongly, resulting in a higher barrier of 1.71 eV. Incorporation of Ru into Cu moderates these effects, reducing the PDS to 1.20 eV, restraining *NO2 desorption, and promoting $NH_3$ release due to weaker *$NH_3$ interaction, thereby improving overall catalytic efficiency (Fig. 9i-j).

Cao et al. reported that the introduction of Ru triggers substantial self-reconstruction of $Co_2(OH)_2CO_3$ nanowires during $NO_3^-$ reduction, forming Ru single-atom sites anchored on $Co(OH)_2$ nanosheets (Ru SASs/Co HNSs) [216]. The engineered Ru SASs/Co HNSs display significantly enhanced catalytic activity, characterized by lower overpotentials, increased $NH_3$ production rates, and superior FE for $NO_3^-$-to-$NH_3$ conversion. Computational studies indicate that strong electronic interactions between Ru SASs and the $Co(OH)_2$ framework stabilize the Ru atoms, while adsorbed $NO_3^-$ undergoes a preferential N-end reduction pathway with *NO as a key intermediate. Additionally, the presence of Ru SASs promotes the hydrogenation of *$NH_2$, the thermodynamically rate-limiting step, thereby accelerating the overall nitrate-to-$NH_3$ conversion. Yunhao et al. designed RuMo alloy nanoflowers with fcc/hcp heterophase delivered 95.2% $NH_3$ FE and stable yields over 20 cycles, with DFT showing high d-band centers that enhance intermediate adsorption and electron transfer while suppressing HER [215]. Similarly, Xinying et al. developed RuFe alloys on single-atom catalyst supports utilized heteroatom ensemble effects to achieve $NH_3$ yield of 118.8 mg $h^{-1}$ $mgcat.^{-1}$ and FE of 92.2% at −1.4 V (vs. RHE) [214]. Heterostructure designs also significantly boost e-$NO_3$RR efficiency. Weijie et al. fabricated Ru/β-$Co(OH)_2$ catalysts with ultra-low Ru content (3.08 at%), where interfacial Ru–Co interactions optimized d–p orbital hybridization with the *$NH_3$ intermediate, lowering energy barriers and accelerating reaction kinetics [217]. Post-reaction analysis indicated that electron-deficient Ru at the interface facilitated *$NH_3$ desorption, enhancing overall catalytic activity. Beyond the above achievements, Ru-based catalysts through nanoscale engineering, support interaction, single-atom dispersion, amorphization, alloying, and heterostructure formation enable rapid, selective, and high-current-density $NH_3$ synthesis under ambient conditions. The combination of lattice strain, electronic modulation, and surface engineering consistently suppresses HER while promoting *H-mediated hydrogenation, establishing Ru as a cornerstone of high-performance e-$NO_3$RR catalysis [16,210,214,215,218,219].

**7.1.2. Pd-based Catalyst**: Pd-based electrocatalysts have emerged as exceptional platforms for $NO_3^-$ → $NH_3$ conversion, owing to their inherent chemical robustness, fast PCET kinetics, and well-balanced hydrogen evolution activity [223,224]. The introduction of secondary metals into Pd frameworks has proven highly effective in fine-tuning electronic properties and surface adsorption behaviors [222,225]. Zhou et al. designed PdM (M = Fe, Co, Ni, Cu) metallenes (Fig. 10a), where ultrathin architectures enhanced active site accessibility, and transition metal dopants served as electron donors, inducing localized electron accumulation on neighboring Pd sites [220]. Bader charge analysis indicated that this electronic reconfiguration shifted the Pd d-band center toward the Fermi level (Fig. 10b), optimizing the adsorption

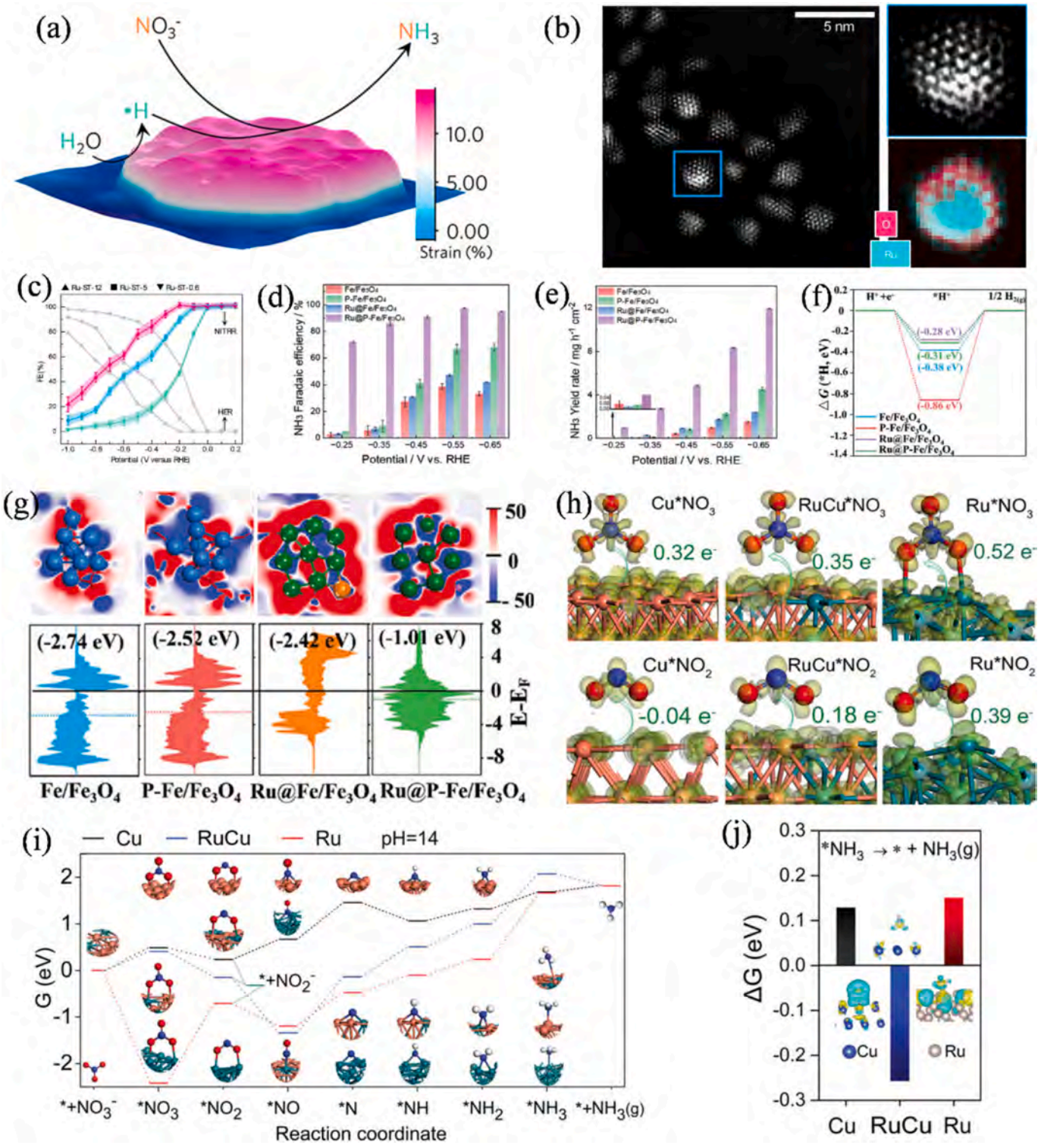



**Fig. 9.** (a) Three-dimensional strain-field distribution maps of the nanostructures. (b) Aberration-corrected HAADF-STEM micrograph with corresponding EELS elemental mapping. (c) Electrocatalytic performance of strained nanoclusters toward $NO_3^-$ → $NH_3$ conversion, showing $FE_{NH3}$ and $FE_{HER}$. (d) $NH_3$ FEs and (e) yield rates of Fe/$Fe_3O_4$, P–Fe/$Fe_3O_4$, Ru@Fe/$Fe_3O_4$, and Ru@P–Fe/$Fe_3O_4$ catalysts across applied potentials. (f) Gibbs free-energy landscapes of HER at 0 V vs. RHE for Fe/$Fe_3O_4$, P–Fe/$Fe_3O_4$, Ru@Fe/$Fe_3O_4$, and Ru@P–Fe/$Fe_3O_4$ surfaces. (g) Top panel: charge density difference maps for $Fe_8$ in Fe/$Fe_3O_4$ and P–Fe/$Fe_3O_4$, $Ru_8$ with adjacent Fe atoms in Ru@Fe/$Fe_3O_4$, and $Ru_8$ in Ru@P–Fe/$Fe_3O_4$ (red = electron accumulation, blue = depletion). Bottom panel: projected density of states (pDOS) of the 3d orbitals in the above catalysts. Dotted color lines mark the d-band centers, solid black lines denote Fermi levels, and shaded regions highlight orbital occupancies. (h) Charge redistribution and electron transfer upon $NO_3^-$ and $NO_2^-$ adsorption on Cu, Ru, and RuCu solid solutions (yellow = electron gain, blue = depletion). (i) Free-energy profiles of key intermediates on Cu, Ru, and RuCu solid-solution catalyst surfaces (color scheme: O = red, N = blue, H = white, Cu = gold, Ru = dark green). (j) $NH_3$ desorption energies and associated charge-density difference maps (insets) for Cu, Ru, and RuCu solid-solution catalysts (yellow = electron accumulation, green = depletion). Reproduced with permission from [155,209,210].

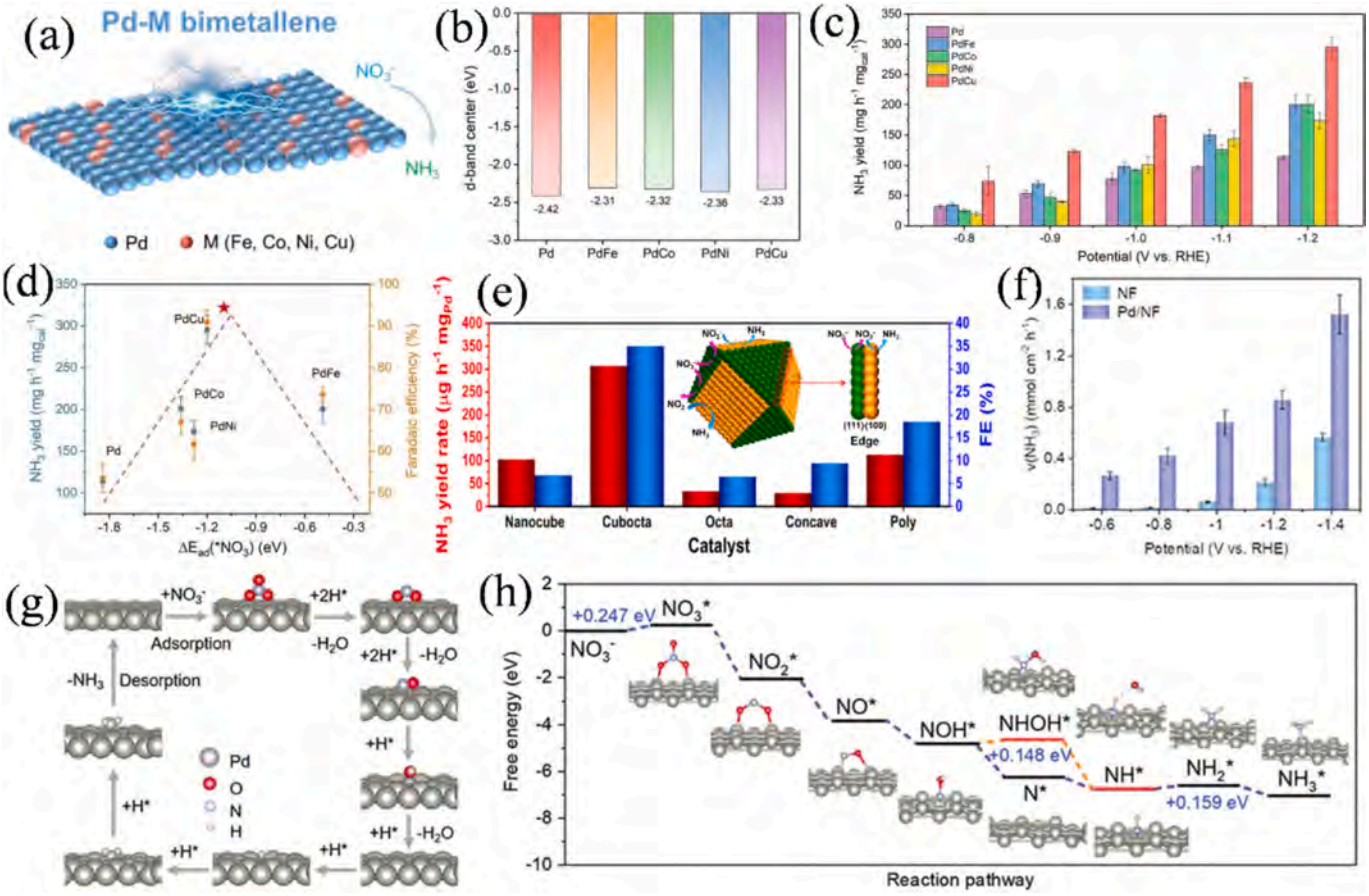



**Fig. 10.** (a) Conceptual diagram of Pd metallenes incorporating different transition metal dopants. (b) Computed d-band center shifts for Pd–M systems (M = Fe, Co, Ni, Cu). (c) Potential-dependent $NH_3$ production rates for pristine Pd and its doped variants (PdFe, PdCo, PdNi, PdCu). (d) Volcano-type trend correlating $\Delta E_{ad}(*NO_3)$ with nitrate reduction activity across Pd metallene dopants. (e) Three-hour $NH_3$ yields and corresponding FEs of all Pd-based catalysts. Inset: schematic showing morphology-controlled Pd nanoparticles. (f) $NH_3$ yield rates of Pd/NF electrodes under different applied potentials. (g) Mechanistic representation of the Pd/NF catalytic pathway for e-$NO_3$RR. (h) Free-energy profile of $NO_3^-$ reduction on the Pd(111) surface. Reproduced with permission from [220–222].

of $*NO_3$, $*NO_2$, and *H intermediates while regulating HER. Among these systems, PdCu alloys displayed superior catalytic performance, achieving a delicate balance of $\Delta E_{ad}(*NO_3)$ that promoted effective hydrogenation without causing surface poisoning (Fig. 10c-d). The nature of the catalyst support profoundly influences Pd activity. Reducible supports such as $SnO_2$, $CeO_2$, and Zr-MOF not only stabilize intermediates and facilitate nitrate adsorption but also enhance mass transport, whereas non-reducible supports exhibit limited activity [226–229]. For instance, Jiang et al. designed a Pd-nanodots on Zr-MOF that delivered an $NH_3$ yield of 287.31 mmol $h^{-1}$ $g^{-1}$cat with 58.1% FE at −1.3 V versus RHE, highlighting the dual role of the support as an electron promoter and transport facilitator [227].

Control over particle shape and exposed facets provides another level of activity modulation. Lim et al. showed that Pd (111) facets preferentially reduce $NO_3^-$ to $NO_2^-$, while Pd (100) facets accelerate $NO_2^-$ conversion to $NH_3$ (**Fig. 10e**) [221]. Combining these facets in cuboctahedral Pd nanoparticles developed by Guo et al. produced synergistic effects that maximized $NH_3$ yield [222]. Self-supported Pd arrays on nickel foam further demonstrated that high surface exposure and scalable architectures enhance activity, achieving 1.52 mmol $h^{-1}$ $cm^{-2}$ $NH_3$ with 78% FE (Fig. 10f). Fig. 10g outlines the Pd/NF pathway where $NO_3$* undergoes successive reduction to N* before hydrogenation to $NH_3$. As shown in Fig. 10h, the critical step is $NO_3$* adsorption (0.247 eV), while Pd facilitates N–H bond formation (0.148 eV), suppressing NHOH* intermediates and steering the reaction toward efficient $NH_3$ production. Bimetallic and heterostructure strategies extend these advantages. As discussed previously, Zhou et al. employed DFT-guided design to identify PdCu bimetallenes as optimal, where transition metal dopants tuned electronic structures, balanced intermediate adsorption, and suppressed HER, resulting in 295 mg $h^{-1}$ $mgcat.^{-1}$ $NH_3$ with 90.9% FE [220]. PdCu mesoporous nanocavities further enhanced mass transport and maintained high FE (96.6%) over extended operation. Other bimetallic systems such as PdAu, PdAg, PdBi, and PdFe, including $PdFe_3$ intermetallics embedded in mesoporous carbon nanofibers, achieved high $NH_3$ yields (1.01 mmol $h^{-1}$ $cm^{-2}$) with excellent stability [230–233].

Single-atom and interfacial engineering also contribute to performance enhancement. $Bi_1Pd$ catalysts exploit synergistic interactions between isolated Bi atoms and adjacent Pd, facilitating $NO_3^-$ activation, destabilizing *NO, and reducing the energy barrier of the PDS (*NO → *NOH), thereby enhancing protonation along the $NO_3^-$ → $NH_3$ pathway [232]. Choi et al. demonstrated that cluster decorated Pd/$Cu_2O$ nanoparticles, featuring multiple heterointerfaces, achieved 0.555 mmol $h^{-1}$ $cm^{-2}$ $NH_3$ production and 2.79 mmol $h^{-1}$ $mg^{-1}$ catalyst with 95.8% FE, with DFT calculations confirming that Pd nanoclusters on $Cu_2O$ surfaces are responsible for the superior activity [234]. Similarly, Yunqing et al. synthesized np Cu–Pd@ZrCuAl catalysts via dealloying and galvanic replacement, achieving 21.46 mg $h^{-1}$ $cm^{-2}$ $NH_3$ with 95% FE [235] The trace Pd enhanced $H_2O$ dissociation, reduced $NO_2^-$ accumulation, and lowered the energy barrier of the RDS, yielding high activity and long-term stability. Yuanwei et al. reported PdNi nanosheets with 181 μmol $h^{-1}$ $cm^{-2}$ $NH_3$ production and 99.6% FE, retaining stability over 20 cycles at −0.77 V versus RHE, offering insights for Zn–$NO_3^-$ battery applications [236]. Considering above efficient work, Pd-based catalysts

achieve high selectivity, yield, and durability for $NO_3^-$ → $NH_3$ conversion by integrating strategies such as bimetallic alloying, single-atom doping, heterostructure design, facet engineering, and optimized supports. The interplay of electronic tuning, active site engineering, and interfacial synergy underpins their superior performance, making Pd systems a benchmark platform for efficient and sustainable e-$NO_3$RR.

**7.1.3. Ag-based Catalyst**: Silver-based catalysts have emerged as promising candidates for electrochemical $NO_3^-$ → $NH_3$ reduction due to their intrinsic conductivity, chemical stability, and ability to facilitate selective redox reactions. Numerous studies highlight the role of Ag as either a primary active site or as part of synergistic architectures with transition metals and oxides [10,237]. Most recently, Swathi et al. reported surfactant-free Ag nanocubes with well-preserved {111} facets, demonstrating excellent activity and stability with nearly 97% FE and stable $NH_3$ yields validated through isotopic labelling and NMR analysis [10]. Similarly, Jiang et al. designed atomic-scale Ag/Ni interfaces in A-Ag@Ni/Ni(OH)$_2$ nanowires, where Ag promoted nitrate adsorption and its reduction to nitrite, while Ni facilitated hydrogen-mediated conversion to $NH_3$ [238]. DFT calculations confirmed that the $H_{ads}$-mediated pathway significantly lowered the energy barrier, resulting in high yield and selectivity.

Beyond binary systems, alloy and composite strategies have shown remarkable advantages. Wen et al. developed fern-like Ag–Cu–P structures that alleviated the tendency of Ag to accumulate nitrite, achieving over 94% selectivity and improved kinetics via d-band center modulation [239]. Recently, Shi *et al.* engineered a heterostructured Ag/$CeO_2$ electrocatalyst that exhibits exceptional activity for the e-$NO_3$RR [240]. The intimate interfacial coupling between metallic Ag and $CeO_2$ facilitates directional electron transfer from Ag to the $CeO_2$ lattice, effectively tuning the local electronic structure and enhancing nitrate adsorption and activation. This interfacial electronic synergy accelerates reaction kinetics while suppressing competitive side reactions, delivering superior catalytic performance. The Ag/$CeO_2$ achieve a FE of 94.4 ± 0.3% at −0.5 V vs RHE, a high $NH_3$ production rate of 13.31 ± 0.13 mg cm$^{-2}$ h$^{-1}$, and remarkable selectivity of 98.58 ± 0.9% at −0.8 V versus RHE. Beyond electrocatalysis, the heterostructure functions effectively as a cathode in a Zn–$NO_3^-$ battery, enabling simultaneous $NH_3$ generation and energy output with a peak power density of 4.1 mW cm$^{-2}$. This work underscores the power of heterostructure design to modulate interfacial charge dynamics and offers a promising strategy for cost-effective, energy-efficient, and sustainable e-$NO_3$RR electrocatalysts. Further, Jia et al. further advanced this approach through a ternary $Cu_7$/$Ag_3$–$Ru_3$/C catalyst, where tandem interfaces optimized both nitrite accumulation and hydrogen supply, delivering industrially relevant $NH_3$ yields and long-term durability in membrane electrode assembly devices [2]. Comparable synergy was also observed in Ag-modified $Co_3O_4$ systems, where interfacial electronic interactions stabilized Co species and enhanced nitrate adsorption, while suppressing side reactions such as hydrogen evolution as reported by Fan et al. and Zhang et al. [241,242]. Through a tailored surface engineering strategy, Liu et al. fabricated AuCu@Ag nanowires where sequential Ag deposition precisely mirrored the intrinsic defects of AuCu cores [243]. This defect-enriched core–shell catalyst delivered remarkable e-$NO_3$RR performance with high $NH_3$ yield, selectivity and FE approaching 96%. Theoretical insights confirmed that the cooperative effects of strain modulation and metal coordination reconFig. d the electronic landscape, thereby accelerating intermediate adsorption and reaction kinetics. Beyond achieving exceptional catalytic activity, this work highlights a versatile route for constructing advanced strained core-shell materials for electrochemical applications. Liao et al. presented a novel semiconductor-liquid junction strategy that restructured interfacial charge distribution to overcome mass transfer barriers in electrocatalysis [24]. By inducing a positively charged Helmholtz layer, the system concentrated nitrate ions more than twentyfold, enabling highly efficient conversion to $NH_3$. Using Ag-$MoS_2$ as a model catalyst, near-unity FE and rapid nitrate removal were achieved, even at trace concentrations, vastly outperforming conventional designs. This interfacial engineering concept extends beyond nitrate, offering a versatile framework for electrochemical reduction of various anionic pollutants in sustainable energy and water remediation technologies. Extensive research has established that Ag-based catalysts ranging from nanostructures to alloys and hybrid interfaces are highly promising for sustainable $NH_3$ electrosynthesis. Their unique capacity to reduce energy barriers, stabilize reactive intermediates, and achieve superior FE underscores their critical role in advancing $NO_3^-$ → $NH_3$ conversion, offering a viable pathway toward scalable nitrogen-driven energy and chemical production.

**7.1.4. Other Nobel Metal Catalysts**: Beyond the widely explored Ag- and Pd-based platforms, several noble metals such as Rh, Ir, and Au have demonstrated remarkable e-$NO_3$RR properties, albeit with challenges related to cost and abundance. Among them, Rh has consistently shown superior catalytic behavior across different structural motifs. For instance, Hui et al. constructed Rh nanoflowers comprised of ultrathin nanosheets, achieving an impressive FE of 95% for $NH_3$ production in 0.1 M $Na_2SO_4$ containing 0.1 M $NO_3^-$, notably outperforming conventional Rh nanoparticles (60%) [244]. DFT analysis attributed this improvement to the high density of under-coordinated Rh atoms, which enhance nitrate adsorption and stabilize hydrogenated intermediates. A complementary strategy was proposed by Liu et al. who immobilized Rh clusters and isolated Rh atoms on Cu nanowires [104]. This hybrid system produced a partial current density of 162 mA cm$^{-2}$ with an FE of 93% at −0.2 V vs. RHE, benefiting from a synergistic pathway where *H species generated on Rh were transferred to *NO intermediates stabilized on Cu, thereby accelerating hydrogenation kinetics. One notable feature of Rh is its resilience in acidic electrolytes, where most transition metals lose stability. Exploiting this, Wei et al. fabricated RhNi bimetallenes with a Rh-rich shell and Rh–Ni alloy core (RhNi@Rh BMLs) using cyanogel reduction followed by acid etching [245]. When tested in $HClO_4$ electrolyte containing nitrate, these catalysts achieved nearly quantitative FE (98.4%) and a high $NH_3$ yield of 13.4 mg h$^{-1}$ mgcat$^{-1}$, maintaining continuous activity for 400 h. This work underscores the potential of Rh-based bimetallics for addressing nitrate contamination in acidic industrial effluents [246].

Iridium nanostructures have also been extensively evaluated due to their tunable surface chemistry and durability. Zhu et al. demonstrated that Ir nanotubes (NTs), generated via HEDP-templated self-assembly, offered a porous, defect-rich architecture that enabled an $NH_3$ yield rate of 921 μmol h$^{-1}$ mgcat$^{-1}$ at a low potential of 0.06 V vs. RHE [247]. These NTs also displayed enhanced oxygen evolution reaction performance, with an overpotential of only 245 mV compared to 297 mV for crystalline Ir nanocrystals, highlighting their bifunctional electrochemical utility. At the atomic scale, Chen et al. embedded single Ir atoms in oxygen-deficient amorphous $MoO_3$ ($Ir_1$/a-$MoO_3$) [248]. Here, $Ir_1$–$O_5$ moieties served as active sites, simultaneously suppressing competing hydrogen evolution and enabling near barrierless hydrogenation of NO, ultimately delivering an FE of 93.2% and an $NH_3$ yield rate of 438.8 μmol h$^{-1}$ cm$^{-2}$. Similarly, Jin et al. prepared Ir single atoms on spinel $Co_3O_4$ through a mechanochemical method [249]. The Ir single atom catalyst-$Co_3O_4$ displayed a superior FE of ~98.1% and yield rate of 5.3 mg h$^{-1}$ mgcat$^{-1}$, outperforming Ir nanoclusters on the same support (84.1% FE, 3.4 mg h$^{-1}$ mgcat$^{-1}$). DFT calculations revealed that atomic-scale dispersion facilitated enhanced charge transfer and reduced energy barriers, establishing single-atom Ir sites as highly efficient centers for e-$NO_3$RR. The integration of Au into hybrid systems offers a strategic pathway to improve catalytic efficiency. Zhang et al. reported Au nanowires decorated with $Co_3O_4$ nanosheets, producing an $NH_3$ yield rate of 2.661 mg h$^{-1}$ mgcat$^{-1}$ with stable operation over 12 h, suggesting that noble metal-oxide composites can effectively integrate conductivity and catalytic activity [250]. While the abovementioned some other noble metal catalysts offer invaluable mechanistic insights and demonstrate extraordinary efficiencies, their scarcity and expense hinder deployment at industrial scale [245,248,251–253].

Consequently, research has shifted toward transition metals such as

Cu and Co, which can achieve comparable selectivity at significantly lower cost. Nevertheless, the advances enabled by noble metals ranging from coordination tuning and bimetallic stabilization to single-atom engineering continue to serve as critical design principles for guiding the development of next-generation electrocatalysts for sustainable $NO_3^-$ → $NH_3$ conversion. Noble metals such as Ru, Pd, Ag, Rh, Ir, and Au exhibit unparalleled intrinsic activity, excellent chemical stability, and precise control over reaction intermediates, enabling high FEs, rapid nitrate reduction, and suppression of competing hydrogen evolution. Their merits include tunable electronic structures via alloying or support interactions, abundant low-coordinate and defect-rich sites in nanoscale or amorphous configurations, and versatile single-atom or heterostructure designs that maximize atomic utilization. These characteristics have allowed for industrially relevant $NH_3$ production rates and durable performance across diverse electrolytes and potentials. However, their widespread application is limited by high material costs, scarcity, and complex fabrication procedures required for strain engineering, atomic dispersion, and interface optimization. Additionally, the fine balance between enhancing nitrate adsorption and preventing surface poisoning necessitates precise structural control, which can complicate scalability. Noble metals provide a benchmark for high-efficiency e-$NO_3$RR catalysis, offering critical mechanistic insights and design strategies that continue to inform the development of cost-effective, durable, and high-performance transition-metal and hybrid systems for nitrate-to-$NH_3$ electroreduction [254].

### *7.2. Carbon-Based Electrocatalysts for Electrochemical Nitrate-to-Ammonia Conversion*

Carbon materials have long been recognized as attractive candidates for e-$NO_3$RR to $NH_3$ due to their abundance, low cost, high electrical conductivity, and versatile structural tunability. While pristine carbon often exhibits limited catalytic activity, careful engineering of its surface chemistry, defect structure, and morphology can significantly enhance its performance [255–259]. This section presents a systematic discussion of carbon-based e-$NO_3$RR electrocatalysts, progressing from pure carbon systems to modified and functionalized variants, highlighting the structural and chemical features that govern their electrocatalytic behavior.

**7.2.1. Pure Carbon Materials (Charcoal, Graphite, and Carbon Cloth):** Unmodified carbon allotropes remain the simplest form of e-$NO_3$RR electrodes, yet their performance is strongly influenced by their structural disorder and surface functional groups. Carbon-based electrodes have shown remarkable potential for e-$NO_3$RR due to their tunable structure, surface chemistry, and conductivity. Xue et al. demonstrated charcoal electrodes derived from carbonized wood exhibit high hydrogen-evolution overpotentials, moderately disordered $sp^3$-rich frameworks, and abundant oxygen-containing groups, enabling rapid nitrate conversion, superior $NH_3$ selectivity (up to 98.5%), and competitive production rates that surpass graphite and carbon cloth and approach metal-based catalyst performance [260,261]. The enhanced activity is attributed to high $sp^3/sp^2$ ratios and oxygenated surfaces, which strengthen nitrate adsorption, accelerate nitrite formation, and suppress gaseous nitrogen byproducts. Graphite electrodes can achieve comparable efficiency through electrochemical activation: applying current for 48 hours increases defect density, enriches oxygen functionalities, and reduces interfacial resistance, providing accessible sites for nitrate adsorption and electron transfer as recently reported by Wenda et al [262]. Activated graphite demonstrates nitrate removal rates up to 94.7% with stable $NH_3$ selectivity (82.6%) over prolonged operation (>81 days) and maintains performance when scaled to large electrode areas, rivaling traditional metal-based systems. Wu et al. introduced an alkali-etched microchannel charcoal (AEMC) cathode featuring long, narrow channels (<10 μm radius, >4 cm length) functionalized with oxygen-containing groups that serve as active sites for nitrate reduction [263]. The microchannel architecture constrains diffusion paths, facilitating efficient $NO_3^-$ transport to the reactive surfaces while mitigating electrostatic repulsion. This structural design enabled a nitrate conversion of 70.8% and a FE of 60.4%, with low energy consumption (0.18 kWh/g $NO_3^-$-N) and complete nitrogen formation in chloride-rich media. Achieving a maximum nitrate removal rate of 31.3 mg/(L·h·$cm^2$), the AEMC cathode surpasses many conventional metal electrodes, highlighting the advantage of combining microscale spatial confinement with targeted surface functionalization for high-performance $NO_3^-$ electroreduction. These studies highlight the critical roles of structural defects, surface oxidation, and electrochemical activation in optimizing carbon-based materials for efficient and durable e-$NO_3$RR applications.

**7.2.2. Amorphous and Oxidized Laser-Induced Graphene:** Laser irradiation offers an alternative strategy to introduce structural strain and defects into graphene, thereby enhancing its electrochemical reactivity. Libei et al. synthesized oxidized laser-induced graphene (ox-LIG) and standard LIG from polyimide using $CO_2$-laser irradiation in air or nitrogen [264]. Structural characterization via HRTEM and atomic pair distribution function analysis revealed shorter average C–C bond lengths in ox-LIG (1.44 Å) compared to reduced graphene oxide (1.46 Å) (according to pair distribution function in Fig. 11a), indicative of lattice strain. EPR further confirmed the presence of abundant radicals, which facilitated intermediate adsorption (Fig. 11b). The strained and defect-rich structure of ox-LIG yielded FE exceeding 85% across −0.73 to −0.93 V vs. RHE, with $NH_3$ production rates up to 2.86 mg $cm^{-2}$ $h^{-1}$ approximately 150% higher than rGO. The reduced energy barrier for *NO to *NOH conversion and improved $NO_2OH$ adsorption accounted for the enhanced activity [265–268].

Graphene, composed of $sp^2$-hybridized carbon atoms in a two-dimensional honeycomb lattice, is valued for its high conductivity, large surface area, and tunable edge states. However, its e-$NO_3$RR performance is strongly dependent on defect sites, which enhance the adsorption of *$NO_3$ and *NO intermediates [270,271]. Le et al. developed small-molecule laser-induced graphene (sm-LIG) featuring a mixed amorphous-crystalline architecture, where honeycomb-like nanocrystallites are embedded within disordered carbon polygons [269]. HRTEM (Fig. 11c-f) reveals dense lattice defects and unpaired electrons confirmed by an EPR peak at g = 2.003 (Fig. 11g) absent in graphite. Variations in EPR intensity align with oxygen content, while precursor molecular structures dictate the observed nanostructural differences. Pair distribution functions (PDF) show consistent nearest (~1.4 Å) and next-nearest (~2.5 Å) neighbor distances across samples, yet sm-LIG exhibits reduced long-range order and amorphous traits relative to crystalline graphite. A shift in C–C bond length to larger values (Fig. 11h) further confirms structural disorder. By tuning precursor aromaticity, the crystalline-to-amorphous ratio was adjusted, achieving an $NH_3$ yield of 2.46 mg $h^{-1}$ $cm^{-2}$ with 83.7% FE, demonstrating that precise defect engineering enhances electron transfer and intermediate stabilization for efficient e-$NO_3$RR catalysis [272,273].

**7.2.3. Carbon Nanotubes:** Carbon nanotubes (CNTs) offer a one-dimensional tubular architecture that combines high conductivity with structural robustness. Their unique confinement effect modulates adsorption pathways at the atomic scale, directing the e-$NO_3$RR toward $NH_3$ formation. Comparative studies revealed that pristine multi-walled CNTs (MWCNTs) exhibit notable activity in near-neutral solutions, while single-walled CNTs deliver even higher selectivity and yield [275,276]. Interestingly, the introduction of oxygen or nitrogen dopants into MWCNTs reduced catalytic activity, suggesting that undoped graphitic carbon atoms themselves can serve as active sites. This finding challenges the conventional notion that heteroatom doping is always beneficial for enhancing carbon electrocatalysis [277]. Most recently, Liu et al. developed a metal-free, carbon-based electrocatalyst composed of winged carbon coaxial nanocables (W-CCNs), created by partially unzipping CNTs to form graphene-like “wings” and expose fresh surfaces (Fig. 12a), followed by the deliberate introduction of topological defects [274]. This architecture integrates a conductive CNT core for efficient

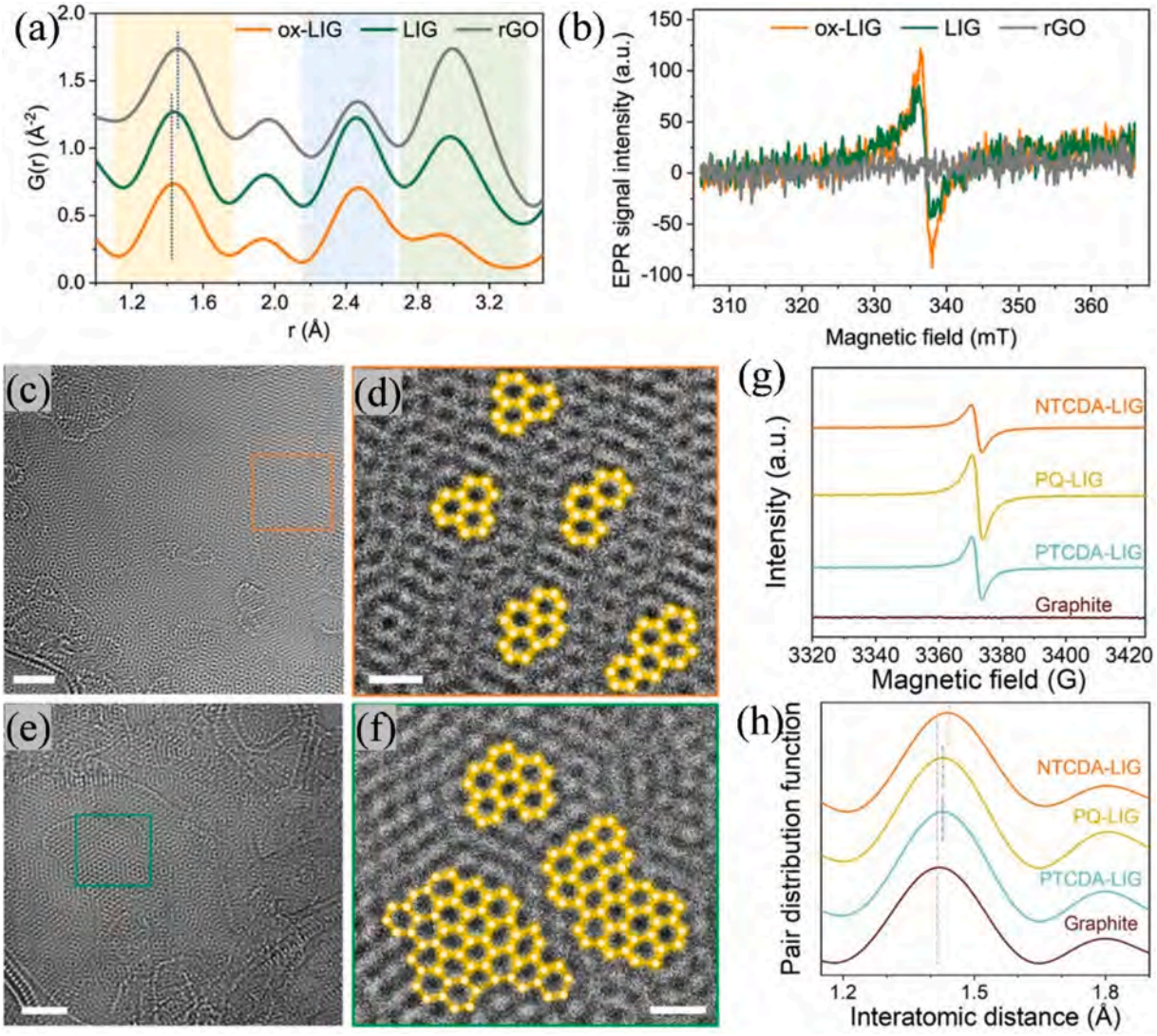



**Fig. 11.** (a) PDF analyses and (b) EPR spectra for ox-LIG, LIG, and rGO. HRTEM images of (c) NTCDA-LIG and (d) PTCDA-LIG with 2 nm scale bars. Magnified views of selected regions for (e) NTCDA-LIG and (f) PTCDA-LIG highlighting six-membered ring domains; scale bars, 0.5 nm. (g) EPR profiles comparing sm-LIGs with a graphite reference. (h) PDF comparisons of sm-LIGs and graphite reference materials. Reproduced with permission from [264,269].

electron transport with an outer shell of defect-rich graphene nanosheets and carbon layers, enabling enhanced $NO_3^-$ adsorption, water dissociation, and N–H bond formation during e-$NO_3$RR (Fig. 12b).

DFT calculations in Fig. 12c identified $C_{577}$ defect sites as the most active, exhibiting the lowest $NO_3^-$ adsorption energy (2.05 eV), outperforming other sites and pristine CNTs. Electrochemical measurements showed a FE of 91.3% and an $NH_3$ yield of 5.41 g $h^{-1}$ $g_{cat}^{-1}$ at −0.3 V, increasing to 88.1 g $h^{-1}$ $g_{cat}^{-1}$ with a $j_{NH_3}$ of 122.4 mA $cm^{-2}$ at −0.5 V (Fig. 12d). These results exceeded those of W-CCNs-850, W-CCNs-1100, and pristine CNTs (Fig. 12e) and remained stable across acidic, neutral, and alkaline media [274]. Benchmarking (Fig. 12f) positioned W-CCNs among the top-performing e-$NO_3$RR catalysts. Further DFT analysis (Fig. 13a-b) confirmed *$NO_3$ adsorption as the RDS, with W-CCNs displaying lower free-energy barriers than CNTs for both adsorption and hydrogenation steps (*NO: 0.16 eV; *NOH: 0.02 eV). Operando FT-IR and DEMS studies revealed a sequential pathway (*$NO_3$ → *$NO_2$ → *NO → *NOH → *N → *NH → *$NH_2$ → $NH_3$), while pH-corrected free-energy profiles in Fig. 13c-d highlighted thermodynamically favorable $NO_3^-$ reduction and *H generation, underpinning the catalyst's high activity over a broad pH range [278,279].

**7.2.4. Engineered Carbon Frameworks:** Carbon architectures with tunable porosity have emerged as versatile platforms for e-$NO_3$RR owing to their capacity to couple efficient ion transport with abundant adsorption sites. Materials such as activated carbon, aerogels, and bio-derived carbons exhibit interconnected pore channels that enhance nitrate accumulation at the catalyst-electrolyte interface and facilitate rapid mass transfer [280]. A representative example is the carbonized eggshell membrane, derived from waste biomass, which, despite a relatively modest surface area, displayed markedly higher nitrate adsorption than conventional activated carbon [281]. Structural characterization revealed a hierarchical pore network, while DFT calculations identified nitrogen moieties within the porous scaffold as key determinants of selective $NO_3^-$ binding. This case underscores the potential of bio-sourced carbons as sustainable, high-selectivity electrode materials, with clear opportunities for further optimization via activation protocols or elemental doping strategies [282,283].

Electronic structure modulation through heteroatom incorporation has proven equally effective in tailoring the catalytic response of carbon frameworks toward nitrate reduction. Substituting lattice carbons with nitrogen, boron, phosphorus, or sulfur alters charge distribution, surface polarity, and intermediate stabilization, collectively improving nitrate chemisorption while suppressing parasitic hydrogen evolution. Nitrogen doping, in particular, is known to introduce functionally distinct sites: pyridinic N enhances nitrate affinity, whereas graphitic N augments

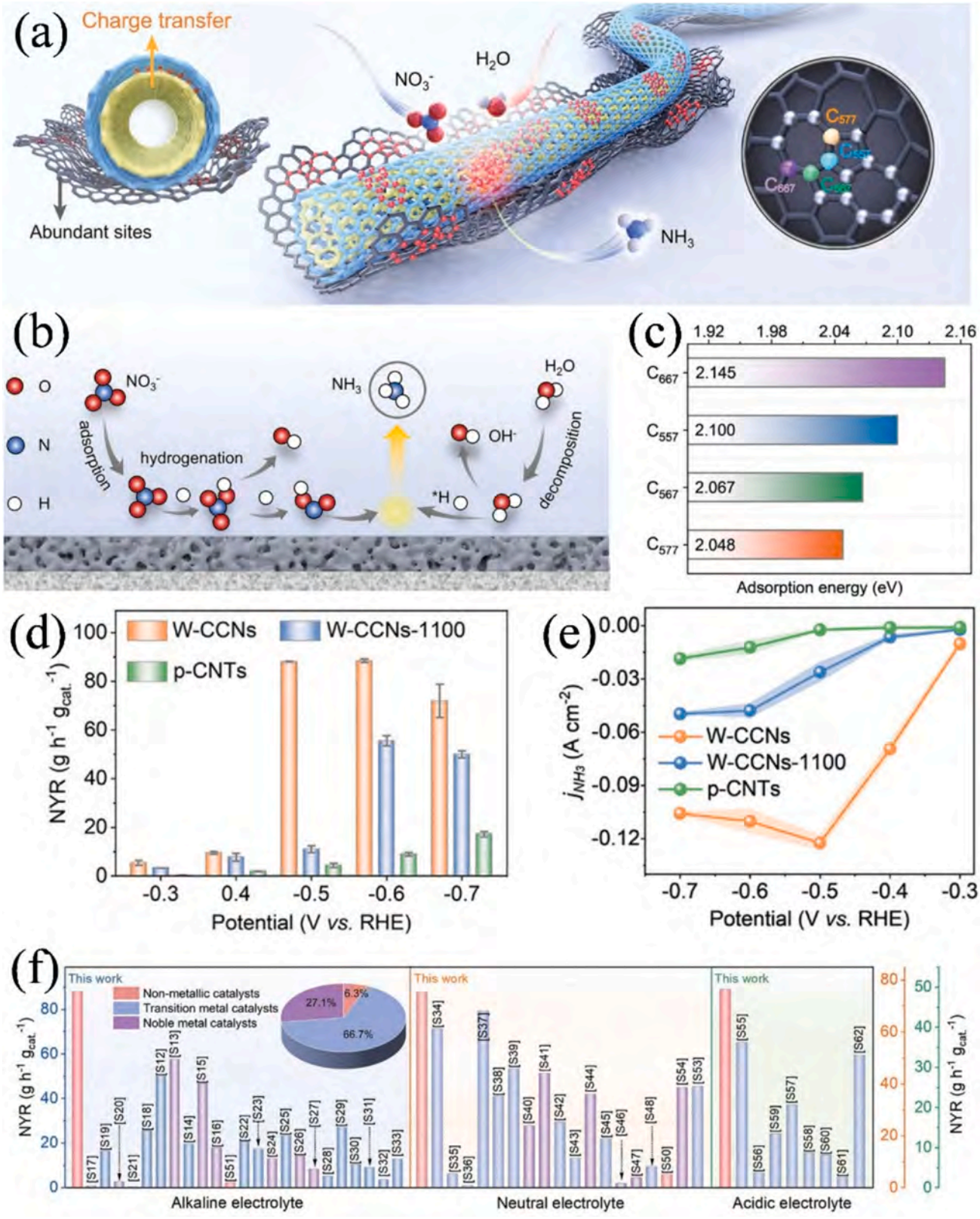



**Fig. 12.** (a) Conceptual schematic of W-CCNs highlighting the potential active sites relevant for e-$NO_3$RR. (b) Illustration of the mechanistic pathway of e-$NO_3$RR occurring on W-CCNs. (c) Computed adsorption energies of the *$NO_3$ intermediate on the W-CCNs surface. (d) Measured $NH_3$ production rates (NYR) and (e) the corresponding current densities for $NH_3$ formation (j$NH_3$) on W-CCNs, W-CCNs-1100, and porous CNTs under varying applied potentials. (f) Comparative analysis of e-$NO_3$RR performance across electrolytes of different pH values, benchmarking W-CCNs against recently reported state-of-the-art catalysts. Reproduced with permission from [274].

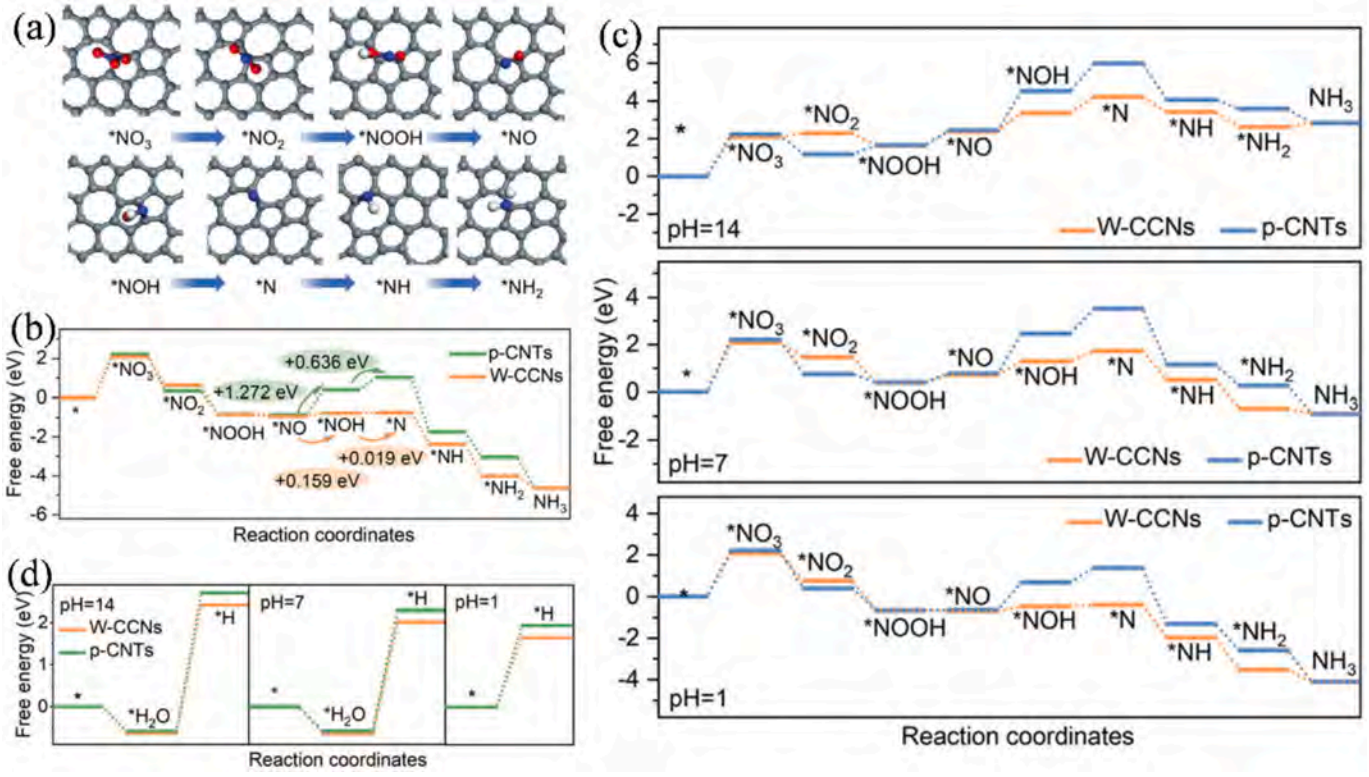



**Fig. 13.** (a) Optimized adsorption geometries of key e-$NO_3$RR intermediates on W CCNs, with atoms represented as C (gray), N (blue), O (red), and H (light white). (b) Free energy pathways for $NH_3$ production from e-$NO_3$RR on porous CNTs and W-CCNs under standard conditions without pH adjustment. (c) Gibbs free energy landscapes for the formation of intermediates during e-$NO_3$RR on W-CCNs and p-CNTs, incorporating pH corrections at 14, 7, and 1. (d) Reaction free energies associated with $H_2$ evolution over W-CCNs and p-CNTs, considering pH-corrected conditions at 14, 7, and 1. Reproduced with permission from [274].

conductivity and reaction kinetics [284]. Boron and phosphorus species disrupt the intrinsic chemical inertness of $sp^2$-carbon, activating the surface for nitrite stabilization and subsequent reduction. In a notable study, boron/oxygen co-doped carbon nitride nanotubes (B/O-CNNTs) synthesized via copolymerization exhibited synergistic modifications of the coordination environment and band structure, while simultaneously introducing frustrated Lewis pairs for nitrate activation [285,286]. This design delivered a FE of 96% and an $NH_3$ yield rate of 211.4 μg $h^{-1}$ $mg^{-1}$ at −1.1 V vs. RHE [287]. The one-dimensional morphology, combined with intrinsic carbon vacancies and dual heteroatom effects, enhanced reactant-active site interactions and electron mobility. Similar doping approaches have also been deployed in carbon-metal hybrid systems, where dopant-metal coordination modulates the d-band center of the metal, further refining catalytic performance [288].

Structural defect engineering provides an additional avenue for maximizing active site density and reactivity. Vacancies, topological distortions, and disordered edge configurations generate localized states that promote nitrate adsorption and facilitate electron injection into key intermediates [289–291]. Oxygen-containing functional groups, such as hydroxyl and carboxyl moieties, further tune hydrophilicity and ionic accessibility. Laser-induced amorphous graphene serves as a compelling example, where lattice disorder, strain, and oxygen functionalities collectively yield near-quantitative FE and an $NH_3$ production rate of 2859 μg $cm^{-2}$ $h^{-1}$ at −0.93 V vs. RHE [264]. X-ray pair distribution function analysis, coupled with high-resolution electron microscopy, revealed that the amorphous carbon network accommodates structural relaxation that stabilizes reaction intermediates. Operando FT-IR and DFT confirmed that these disordered domains act as transient binding pockets, facilitating stepwise reduction. In another instance, a nitrogen-doped carbon catalyst (NHC-1000) with co-engineered quaternary-N sites and nitrogen vacancies achieved 91.2% FE and 2.6 mmol $h^{-1}$ $g^{-1}$ $NH_3$ yield at −0.5 V vs. RHE [203]. Mechanistic modeling identified quaternary nitrogen as critical in accelerating *NO protonation, while adjacent N vacancies promoted *$NH_2$ formation, illustrating the cooperative effects of dual defect centers [26]. By integrating porous network design, heteroatom-induced electronic tuning, and defect-mediated active site generation, carbon-based catalysts can be rationally engineered to balance adsorption, selectivity, and electron transfer. Such multi-faceted structural control provides a pathway toward high-performance, durable, and sustainable electrocatalysts for the $NO_3^-$ → $NH_3$ conversion process [292–297]. Recently, Zhang et al. engineered NbC@CNFs heterostructure as a highly active and durable electrocatalyst for nitrate and nitrite reduction to $NH_3$ [298]. This catalyst demonstrates exceptional electrochemical performance, achieving a FE of 94.4% and an $NH_3$ yield of 30.9 mg $h^{-1}$ $mg_{cat}^{-1}$. In situ electrochemical measurements indicate that nitrite reduction follows the *NO intermediate pathway, corroborated by Gibbs free energy calculations of sequential deoxygenation and hydrogenation steps. Electronic structure analysis shows that the NbC@CNF interface broadens the DOS near the Fermi level, promoting efficient charge transfer and enhanced adsorption of reactive intermediates. Finite element simulations further reveal localized current and electric field accumulation at the NbC nanoparticles, identifying them as the primary active sites. This study provides a mechanistically guided design strategy for stable, high-performance transition metal carbide-carbon heterostructures in sustainable $NH_3$ electrosynthesis [299].

Concluding the above advancements, carbon-based electrocatalysts present a compelling platform for e-$NO_3$RR owing to their intrinsic abundance, high electrical conductivity, and versatile tunability of structure and surface chemistry. Pure carbon allotropes, such as charcoal, graphite, and carbon cloth, offer high stability and scalable performance, particularly when defect sites and oxygen-containing functionalities are optimized to facilitate nitrate adsorption and suppress competing hydrogen evolution. Advanced architectures, including

laser-induced graphene, carbon nanotubes, and engineered porous frameworks, further enhance electron transport, intermediate stabilization, and active site density through defect engineering, heteroatom doping, and hierarchical porosity. These strategies have enabled FEs exceeding 90% and $NH_3$ production rates comparable to or surpassing those of many metal-based catalysts. However, limitations remain, including the inherent inertness of pristine $sp^2$-carbon lattices, the complex synthesis routes required for defect and dopant engineering, and the potential trade-offs between conductivity and functionalization. Moreover, precise control over pore size, defect density, and heteroatom distribution remains challenging, often necessitating cost-intensive or energy-intensive treatments. Despite these drawbacks, the tunable electronic structure, chemical stability, and sustainability of carbon-based materials make them a promising class of catalysts for efficient, selective, and scalable $NO_3^- \rightarrow NH_3$ conversion, particularly when rationally designed with multi-modal structural and chemical modifications.

### 7.3. Non-Nobel Metal-based Materials

Non-noble metals are elemental materials notable for their excellent electrical and thermal conductivity, which arises from their closely packed atomic lattices. These intrinsic properties also endow them with high mechanical strength, ductility, malleability, and metallic reflectivity, making them versatile for electrocatalytic applications. Transition metals such as Cu, Fe, Co, Ni, Bi, and In have gained particular attention for e-$NO_3$RR to $NH_3$ due to their combination of accessibility, low cost, and catalytic efficiency [11,300–302]. These metals facilitate nitrate adsorption and multi-electron transfer processes while suppressing competing reactions like hydrogen evolution, resulting in high selectivity toward $NH_3$. Their surface and electronic structures can be tuned to further enhance activity and durability, making them highly attractive for scalable and sustainable $NH_3$ production. Beyond cost-effectiveness, their abundance and environmentally friendly nature reinforce their suitability for practical wastewater treatment and energy-efficient electrocatalysis [4,303,304]. In the subsequent section, we will present a detailed discussion of several representative non-noble metal catalysts, examining their structural features, reaction pathways, and performance metrics in $NO_3^- \rightarrow NH_3$ conversion.

**7.3.1. Cu based Catalyst:** Copper-based materials have demonstrated remarkable potential for electrochemical $NO_3^- \rightarrow NH_3$ conversion due to their ability to facilitate stepwise reduction of $NO_3^-$ through $NO_2^-$ to $NH_3$ [310–312]. The catalytic performance is strongly influenced by surface exposure, crystal facet orientation, electrode morphology, and local electrolyte conditions as demonstrated by Ren et al (Fig. 14a) [305]. Engineering the surface facets of Cu has proven particularly effective in modulating electronic properties, thereby tuning adsorption energies and intermediate stability as reported by Hu et al [306]. For example, in situ electrochemical reduction of ultrathin copper oxide sheets has yielded Cu nanobelts with controlled (100) and (111) surface terminations. Computational and experimental studies reveal that specific intermediates, such as *N, can stabilize certain facets, enhancing both FE and $NH_3$ production rates as reported by Wang et al [307]. Cu (100)-rich surfaces favor hydroxylamine formation at low potentials, whereas Cu(111)-dominant surfaces enhance $NH_3$ generation under higher applied voltages, highlighting the importance of facet-specific surface design (Fig. 14b-c).

Single-atom Cu catalysts represent another frontier, offering maximal atom utilization and highly tunable electronic structures [313]. Tonghe et al. reported coordination with nitrogen in carbon supports (Cu-N-C) creates well-defined active sites that strongly adsorb $NO_3^-$ and $NO_2^-$ while facilitating multi-step hydrogenation sequences (*NO → *HNO → *$H_2$NO → *$H_2$NOH) [308,314]. The system sustained a FE exceeding 92% over multiple reaction cycles, confirming its robustness under prolonged operation. Computational insights revealed that the catalytic performance originates from the intimate coordination between copper and nitrogen centers (Fig. 14d). In particular, the Cu-$N_2$ configuration provides favorable adsorption sites for nitrate and nitrite intermediates, ensuring efficient electron transfer and facilitating their stepwise conversion. This optimized interaction between Cu and N ultimately drives the selective formation of $NH_3$ and nitrogen with remarkable efficiency. Wang et al. shows structural modifications, including low-coordinated Cu-$N_3$ or pyridine-rich $CuN_4$ sites on high-curvature nitrogen-doped carbon nanotubes, optimize reaction kinetics by lowering energy barriers for the RDS, yielding high $NH_3$ selectivity and production rates (Fig. 14e) [309,315,316].

Constructing heterostructures provides an effective means to modulate electronic interactions and facilitate rapid charge redistribution at the interface, which collectively strengthen catalytic activity and improve selectivity toward $NH_3$ in the e-$NO_3$RR. For instance, Qi *et al.* elucidated the pivotal role of interfacial coupling in enhancing the e-$NO_3$RR performance of $Cu_{1.5}Mn_{1.5}O_4/CeO_2$ heterostructured nanofibers [317]. The strong electronic interactions established at the $Cu_{1.5}Mn_{1.5}O_4/CeO_2$ interface, driven by the dynamic redox equilibrium between $Ce^{3+}$ and $Ce^{4+}$ species, create an energetically favorable charge-transfer region that accelerates surface reaction kinetics. DFT calculations further reveal that the $Cu_{1.5}Mn_{1.5}O_4/CeO_2$ heterostructure exhibits a balanced nitrate adsorption energy and the lowest energy barrier for the potential-determining step compared with pristine $Cu_{1.5}Mn_{1.5}O_4$ and physically mixed $Cu_{1.5}Mn_{1.5}O_4/CeO_2$ composites. This interface-engineered architecture demonstrates outstanding e-$NO_3$RR activity, achieving a remarkable FE of 93.07 ± 1.45% at −0.481 V vs RHE and an exceptional $NH_3$ yield rate of 48.06 ± 1.32 mg $cm^{-2}$ $h^{-1}$ at −0.681 V vs RHE. In addition, the $Cu_{1.5}Mn_{1.5}O_4/CeO_2$ heterostructure exhibits superior glycerol oxidation reaction (GOR) activity, enabling a coupled e-$NO_3$RR–GOR configuration for energy-efficient and sustainable $NH_3$ production. More recently, Wang et al. developed a highly efficient Cu@CNFs electrocatalyst for the e-$NO_3$RR [282]. The exposed d-orbitals of copper facilitate strong adsorption of nitrate and promote its stepwise deoxygenation and hydrogenation, leading to a high $NH_3$ yield of 24.22 mg $h^{-1}$ $mg_{cat}^{-1}$ and a FE of 86.38% at −1.2 V vs. RHE. Mechanistic analysis identifies the *NO–*N intermediate as the RDS, with an energy barrier of only 0.79 eV, highlighting the pivotal role of copper's electronic structure in enhancing nitrate activation and accelerating $NH_3$ formation. This effort provides a strategic framework for the rational design of transition-metal-based electrocatalysts with optimized electronic properties for selective and efficient nitrate-to- $NH_3$ conversion.

Copper clusters combine the advantages of high surface density, rapid charge transfer, and robust chemical stability. Facet-controlled nanoclusters, such as Cu nanodisks exposing (111) planes, promote $NO_3^-$ adsorption and sequential N–O bond cleavage, efficiently generating $NH_3$ reported by Keming et al [318]. Supporting Cu clusters on MOFs prevents aggregation and ensures uniform activity demonstrated by Yan et al [319], while bimetallic designs such as Ag-Cu clusters enhance synergistic effects, accelerate intermediate hydrogenation, and suppress side reactions confirmed by Guanyu et al [320]. Atomic-precision clusters expose accessible Cu-Ag sites that further improve catalytic performance relative to monometallic analogs. The progression from facet-engineered Cu nanostructures to single-atom catalysts and finely tuned clusters underscores the central role of precise atomic and electronic control in promoting $NO_3^-$ adsorption, electron transfer, and multi-step hydrogenation [2]. Such design strategies collectively enable high FE, superior $NH_3$ yield, and operational stability, establishing copper-based materials as leading candidates for sustainable nitrate reduction [19,321,322].

**7.3.2. Fe based Catalyst:** Iron-based catalytic systems have steadily advanced as practical platforms for nitrate reduction, owing to their natural abundance, low cost, and alignment with environmentally sustainable chemistry [323–326]. At the simplest level, nanoscale zero-valent iron has shown remarkable promise in purifying groundwater and industrial effluents by reducing nitrate and related pollutants, simultaneously oxidizing into ferrous and ferric ions [327]. This

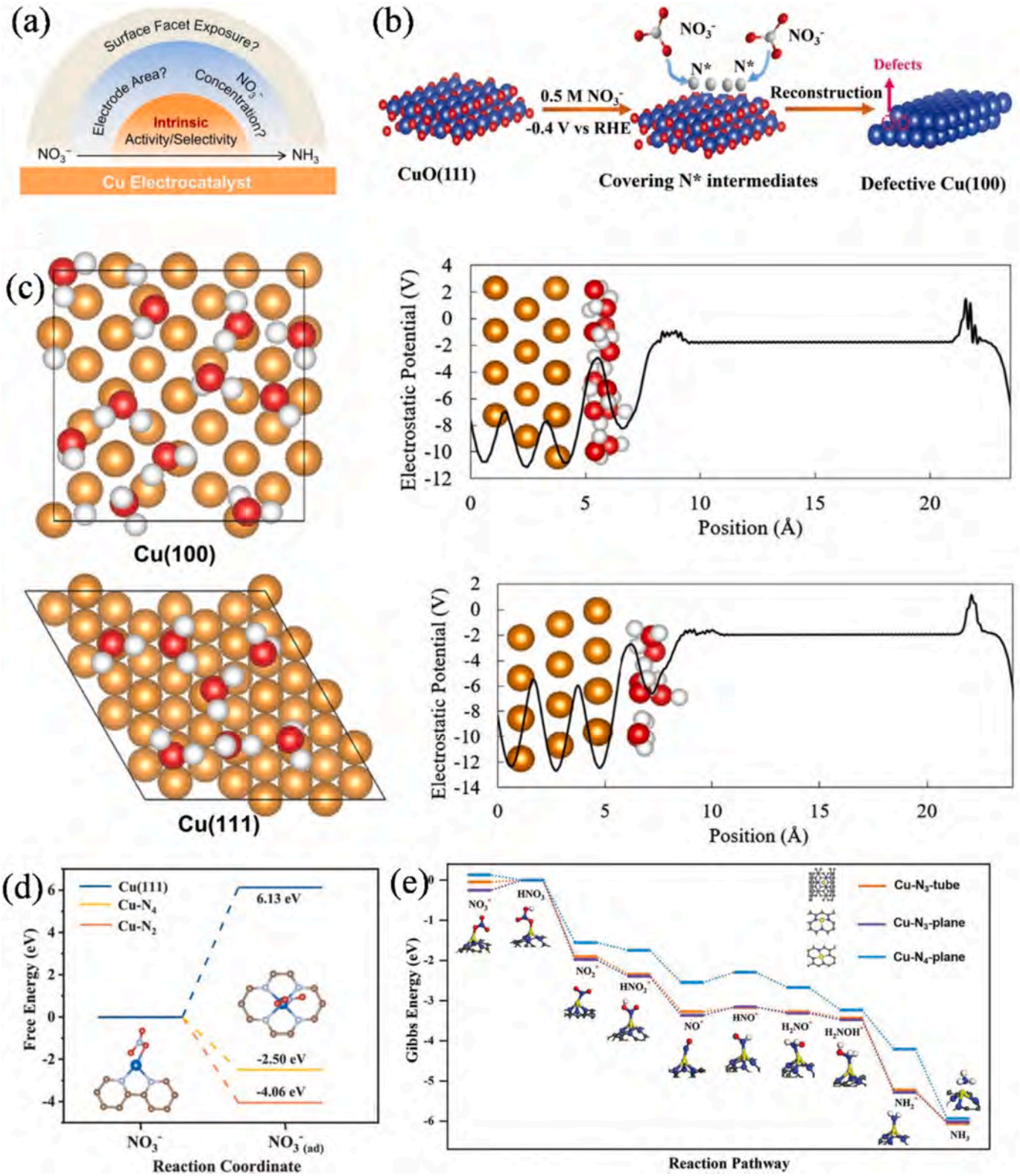



**Fig. 14.** (a) Conceptual representation of the intrinsic activity and selectivity of Cu based electrocatalysts. (b) Illustration of e-$NO_3$RR intermediate (N*) adsorption dynamics influenced by facet exposure on CuO(111) nanobelts during nitrate reduction. (c) Relaxed slab models for Cu(100) and Cu(111) incorporating explicit water layers and implicit solvation effects, with potential energy profiles (color scheme: Cu-brown, O-red, H-white). (d) Computed adsorption free energies of $NO_3^-$ on Cu(111), Cu-$N_4$, and Cu-$N_2$ surfaces (C-brown, N-blue, Cu-gray, O-red). (e) Proposed e-$NO_3$RR reaction pathways highlighting Cu-$N_3$-tube (orange), Cu-$N_3$-plane (purple), and Cu-$N_4$-plane (blue) configurations with corresponding energy profiles. Reproduced with permission from [305–309].

reaction not only supports pollution control but also plays a role in sustaining the nitrogen cycle. More recently, integrating low-valence iron into structured supports such as nickel phosphide nanosheets has further enhanced activity and selectivity toward $NH_3$ production [328,329]. A major step forward has been the emergence of iron single-atom catalysts, where isolated iron centers suppress competing nitrogen pathways that usually occur through N–N coupling. These atomically dispersed sites display far greater $NH_3$ yields compared with iron nanoparticles [330,331]. Xu et al. develop a hollow carbon framework decorated with iron atoms coordinated to nitrogen and phosphorus

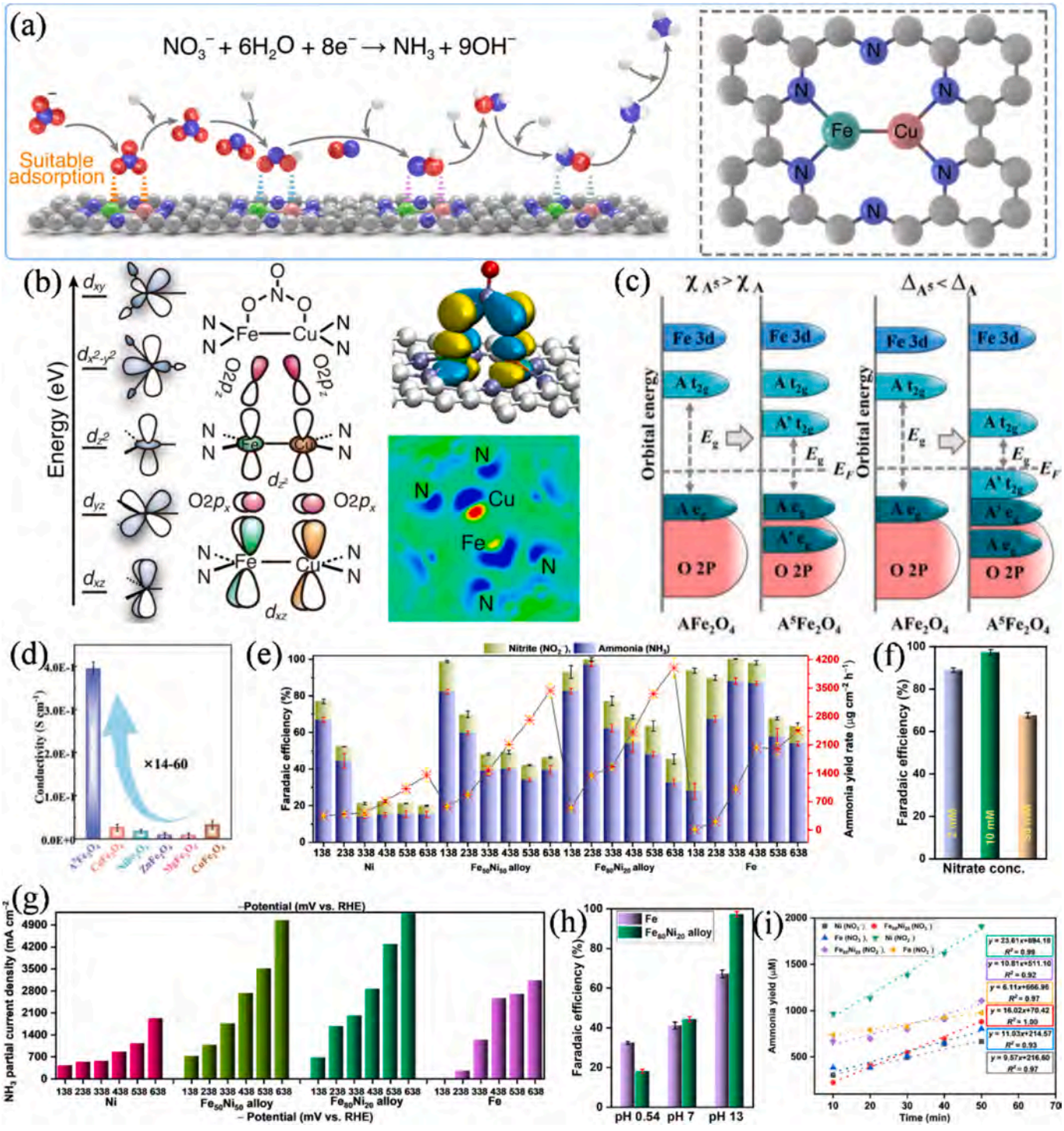



**Fig. 15.** (a) Stepwise schematic of $NO_3^-$ electroreduction to $NH_3$. (b) Molecular orbital mapping illustrating the "Y-type" triple coordination of metal 3d orbitals, their interaction with nitrate Wannier orbitals, and the electron density distribution over the Fe/Cu dimer plane. (c) Diagram depicting the incorporation of a higher-electronegativity transition metal, which narrows the bandgap by introducing intermediate electronic states between the original eg and $t_2g$ orbitals. (d) Measured electronic conductivity of various spinel oxide catalysts. (e) FEs for $NH_3$ and $NO_2^-$ generation and $NH_3$ yield rates at multiple applied potentials for Ni, $Fe_{50}Ni_{50}$, $Fe_{80}Ni_{20}$, and pure Fe catalysts. (f) $NH_3$ FEs at −0.238 V (vs. RHE) across different nitrate concentrations. (g) Calculated $NH_3$ partial current densities for each catalyst as a function of applied potential. (h) $NH_3$ FEs under acidic, neutral, and alkaline conditions at −0.238 V (vs. RHE). (i) Time-dependent electrolysis profiles for $NO_3^-$ and $NO_2^-$ reduction on Ni, Fe, and $Fe_{80}Ni_{20}$ catalysts at −0.238 V (vs. RHE). Reproduced with permission from [148,333,334].

showed that introducing phosphorus disrupted charge symmetry, creating asymmetric atomic environments that favored nitrate adsorption and stabilized reaction intermediates [330]. Similarly, Song et al. recently introduced a hybrid electrocatalyst in which isolated iron sites were integrated with carbon-encapsulated iron phosphide nanoparticles. This structural design effectively modulated charge distribution and tailored electronic states, thereby enhancing intermediate adsorption and achieving markedly improved conversion efficiency [331,332].

Beyond isolated sites, pairing two different metals has offered additional opportunities. An example is the dual iron-copper catalyst anchored on nitrogen-doped graphene recently reported by Zhang et al [148]. which displayed high activity by lowering the barrier for the initial nitrate reduction step and promoting subsequent hydrogenation (Fig. 15a). The cooperative orbital interaction between the two metals provided stronger binding of nitrate and more efficient charge transfer, as illustrated in Fig. 15b. Progress has also been achieved with high-entropy nanocages by Tang et al. where iron was combined with several other metals to create active centers of reduced symmetry that improved water dissociation and hydrogen delivery [335]. These materials delivered exceptionally high $NH_3$ selectivity and yield. Compound-based systems extend the scope further. Qi et al. designed ultrathin spinel oxides containing iron and multiple additional cations achieved metal-like conductivity and adjustable electronic states [333], both of which enhanced catalytic performance (Fig. 15c-d). Another notable design involved an iron boride catalyst developed by Zhang et al, where iron sites facilitated water activation while boron sites strongly bound nitrate, creating a cooperative mechanism [336]. This dual-site process achieved efficient hydrogen migration and substantially lowered the energy barrier for conversion.

Majhi et al. demonstrated highly effective bimetallic Fe–Ni alloys electrocatalyst for $NO_3^- \rightarrow NH_3$ conversion, with $Fe_{80}Ni_{20}$ delivering the most outstanding performance [334]. This composition reached a FE of 97.28±1.36% and an $NH_3$ yield of 3999.1±242.59 μg $h^{-1}$ $cm^{-2}$ at −0.238 $V_{RHE}$ (Fig. 15e). Notably, the catalyst preserved strong selectivity even under dilute nitrate conditions of 2 mM (Fig. 15f), while the corresponding current density for $NH_3$ production is depicted in Fig. 15g. Performance comparisons under different pH environments revealed that $Fe_{80}Ni_{20}$ far outperformed pure Fe, achieving nearly complete efficiency in alkaline medium (97.28±1.36% at pH 13 versus 67.24±1.94% for Fe) (Fig. 15h). Mechanistic analysis suggested a division of roles within the alloy: Fe centers predominantly drive nitrate adsorption and its reduction to nitrite, whereas Ni sites accelerate the subsequent hydrogenation step leading to $NH_3$ formation (Fig. 15i). These developments from nanoscale zero-valent iron to single-atom systems, bimetallic structures, and entropy-stabilized compounds demonstrate a logical progression in catalyst design. Each stage strategically addressed critical challenges such as selectivity, adsorption strength, and multi-electron transfer, establishing iron-based materials as some of the most versatile and high-performing candidates for electrochemical $NO_3^- \rightarrow NH_3$ transformation [337–340].

**7.3.3. Co based Catalyst:** Cobalt-based architectures represent a particularly dynamic class of electrocatalysts for nitrate reduction, owing to their ability to undergo electronic reconstruction, expose facet-specific active sites, and stabilize multiple nitrogen intermediates along complex reduction pathways [341–344]. Subtle variations in surface crystallography exert profound influence over product distribution. For instance, Zhu et al confirmed $Co_3O_4$ with dominant (111) planes preferentially channels electron transfer toward $NH_3$ formation, whereas (100) and (001) facets present a more balanced adsorption environment that supports parallel reduction routes [345]. These trends originate from facet-dependent modulation of the cobalt d-band and its overlap with the antibonding orbitals of nitrate-derived species, as substantiated by DFT simulations that map changes in free-energy landscapes [346]. In parallel, the coexistence of $Co^{2+}$ and $Co^{3+}$ states impart redox flexibility, where lower-valent sites facilitate hydrogenation of *NO to *NOH while higher-valent centers provide stronger anchoring for $*NO_3$ and $*NO_2$ [347,348]. Engineering the distribution of oxidation states through vacancy introduction, electronic doping, or heterointerface construction has therefore emerged as a powerful strategy for steering selectivity and accelerating turnover [349,350].

Catalyst reconstruction involves dynamic surface and structural transformations under reaction conditions, critically impacting catalytic activity and durability. For instance, Shi et al. revealed that during the e-$NO_3$RR, cobalt-based catalysts experience dynamic surface reconstruction arising from an imbalance between the electrons consumed in $NO_3^-$ reduction and those delivered by the external bias [351]. To address this intrinsic instability, a $Co_6Ni_4$ heterostructured catalyst was rationally designed to inhibit Co surface reconfiguration and ensure structural integrity during prolonged operation. The incorporation of Ni atoms precisely modulates the electronic landscape of Co, preserving its electron-rich nature and expediting interfacial charge transfer. Additionally, the Co/Ni heterointerfaces and Ni-enriched domains exhibit enhanced $NO_3^-$ adsorption capacity and favorable binding energetics toward reaction intermediates, enabling a more efficient tandem reduction sequence from $NO_3^-$ to $NO_2^-$ and ultimately $NH_3$. As a result, the $Co_6Ni_4$ catalyst achieved an impressive FE above 90% over a wide potential range (−0.176 to −0.576 V), demonstrating outstanding catalytic activity and stability [351]. By demonstrating the critical impact of interfacial electronic modulation and structural stabilization on suppressing catalyst reconstruction, the study provides a strategic framework for developing durable and efficient electrocatalysts for sustainable e-$NO_3$RR $NH_3$ synthesis.

Defect engineering provides an additional degree of freedom in tuning catalytic functionality [352]. Oxygen vacancies not only lower the potential required for N–O bond scission but also generate localized electronic states that enhance conductivity and stabilize partially reduced nitrogen intermediates [353,354]. In situ and operando spectroscopies corroborate these effects, revealing that vacancy-rich cobalt oxides sustain stronger $*NO_2$ and $*NH_2$ binding while simultaneously facilitating charge migration across the lattice [355]. Incorporating heteroatoms further expands the electronic design space. Transition-metal dopants can shift the cobalt d-band center to rationally tune adsorption strength, whereas nonmetal dopants such as nitrogen polarize the coordination environment and accelerate interfacial charge redistribution, both of which translate into higher FE toward $NH_3$ [356–358]. More recently, atomically dispersed Co centers and framework-derived cobalt catalysts have demonstrated unique electronic configurations that differ from bulk oxides or metallic phases, producing exceptionally high selectivity for $NH_3$ by stabilizing hydrogenated intermediates while suppressing competing hydrogen evolution [359].

Likewise, formation of cobalt-based heterostructures or Schottky-type junctions induces interfacial charge transfer and internal electric fields that accelerate electron flow and promote directional reaction kinetics. Most recently, Qi *et al.* reported a continuous-fiber Co/$In_2O_3$ heterostructure exploiting the Mott-Schottky effect to enhance e-$NO_3$RR [360]. The optimized Co/$In_2O_3$-1 catalyst delivers an exceptional $NH_3$ yield of 70.1 mg $cm^{-2}$ $h^{-1}$ at −0.8 V vs. RHE and a FE of 93.34% at 0 V vs. RHE, outperforming both pristine Co, $In_2O_3$, and most previously reported Co-based heterostructures. Mechanistic investigations reveal that the Mott-Schottky interface drives **preferential electron transfer,** creating electron-rich Co sites and hole-rich $In_2O_3$ facets, thereby optimizing active-site utilization. This interfacial electronic modulation substantially lowers the reaction energy barrier for nitrate reduction, enhancing both catalytic activity and selectivity. The study underscores the effectiveness of Mott-Schottky heterojunction engineering as a rational strategy for designing high-performance, sustainable electrocatalysts for $NH_3$ synthesis. Introducing n-type or p-type semiconducting domains enables the construction of Mott–Schottky heterojunctions, where interfacial charge redistribution gives rise to the characteristic Mott–Schottky effect [361,362]. Xiaoya et al. reported a Co@$TiO_2$

nanobelt array integrated on a n-type titanium substrate as an efficient platform for electrocatalytic nitrate reduction [363]. The intimate contact between metallic cobalt and semiconducting $TiO_2$ establishes a Schottky junction, giving rise to a built-in electric field that lowers the kinetic barrier of the RDS while enhancing nitrate adsorption. Benefiting from this interfacial electronic modulation, the catalyst delivers a FE of 96.7% and an $NH_3$ yield of 800 μmol $h^{-1}$ $cm^{-2}$ under neutral conditions, and further demonstrates robust electrochemical durability over a 50-hour continuous operation. Yu et al. engineered Co/p-type CoO nanosheet arrays that exhibit superior $NO_3^- \rightarrow NH_3$ electrocatalysis, with a FE of 93.8% and $NH_3$ selectivity of 91.2%, markedly higher than Co-only nanosheets [364]. Mechanistic studies, including $^{15}N$ isotope labeling, $^1H$ NMR, in situ FTIR, DEMS, and DFT simulations revealed that the Schottky interface induces electron depletion on Co, facilitating selective nitrate reduction while suppressing hydrogen evolution and side-product formation. This interfacial electron modulation underpins the exceptional efficiency and selectivity toward $NH_3$ production. Such architectures minimize parasitic reactions, stabilize dynamic oxidation states under bias, and improve operational durability. These advancements underscore cobalt's exceptional versatility as a e-$NO_3$RR catalyst. Through concerted control over surface termination, valence-state distribution, defect density, and interfacial electronic coupling, it is possible to finely regulate adsorption energetics and reaction pathways. The integration of these atomic- to mesoscale design principles has positioned cobalt-based materials as leading candidates for electrochemical $NH_3$ production under sustainable conditions [365,366].

**7.3.4. Ni based Catalysts:** Nickel-based electrocatalysts have emerged as promising candidates for nitrate reduction due to their

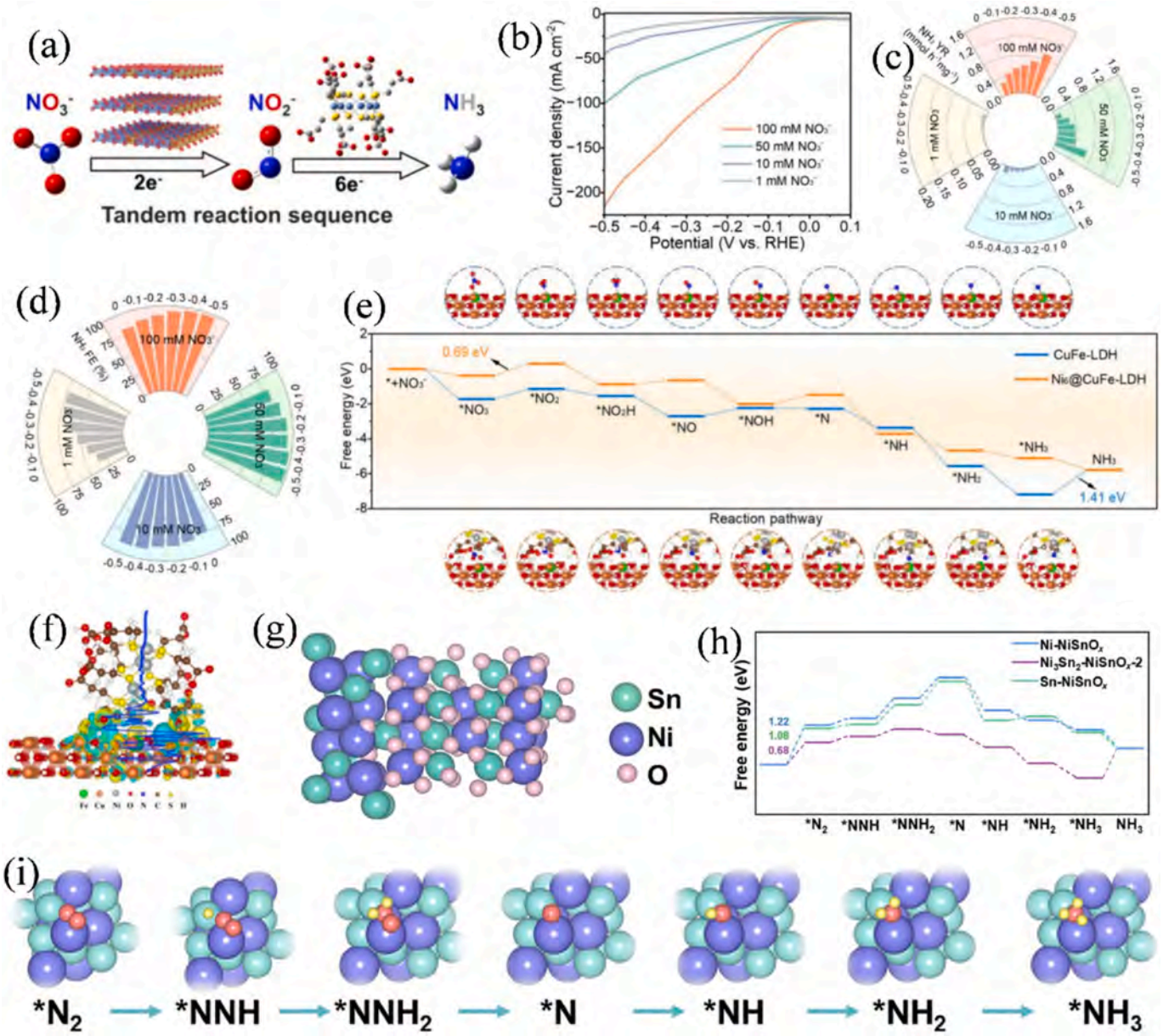



**Fig. 16.** (a) Schematic illustration of the tandem catalytic pathways for nitrate electroreduction to $NH_3$ over $Ni_6$@CuFe-LDH electrocatalysts. (b) LSV profiles. (c) $NH_3$ generation rates and (d) corresponding FEs. (e) Calculated free-energy landscapes for CuFe-LDH and $Ni_6$@CuFe-LDH. (f) Charge density redistribution and planar-averaged charge density plots (blue curve) for $Ni_6$@CuFe-LDH, where the dashed line denotes the Fermi level (iso-surface = 0.001 e/$bohr^3$). Yellow regions represent electron accumulation, while cyan regions indicate electron depletion. (g) Optimized structural configurations of $Ni_3Sn_2$–$NiSnO_x$ alloy-oxide catalysts. (h) Free-energy profiles of e-NRR pathways on $Ni_3Sn_2$–$NiSnO_x$. (i) Simplified mechanistic scheme depicting the stepwise conversion of $NO_3^- \rightarrow NH_3$ on $Ni_3Sn_2$–$NiSnO_x$ catalysts. Reproduced with permission from [371,372].

distinctive electronic configurations and intrinsic catalytic activity. However, their performance is often constrained by rigid coordination environments, limiting nitrogen adsorption and activation. Yao et al. addressed this limitation by in-situ synthesizing $Ni_2P$ on Ni foam with a (111) facet, producing a catalyst that combines metallic conductivity, low impedance, super-hydrophilicity, and abundant surface-active sites, enabling efficient $NO_3^-$ adsorption, hydrogen evolution, and selective $NH_3$ formation [367,368]. Some recent works such as Jia et al. engineered $TiO_{2-x}$ nanotubes enriched with oxygen vacancies, which promote $NO_3^-$ activation by weakening N–O bonds, as confirmed by DFT and DEMS analyses, thereby enhancing $NO_3^- \rightarrow NH_3$ conversion [89,172]. Bimetallic systems further illustrate the advantage of Ni integration. Fang et al. fabricated CuNi alloys on N-doped carbon films, identifying $Cu_{0.43}Ni_{0.57}$/NC as optimally active [369]. Ni incorporation reduces the energy barrier for $*NO_2 \rightarrow *NO$ conversion, boosting overall reactivity. Wang et al. demonstrated that $Cu_{50}Ni_{50}$ alloys shift the potential-determining step from nitrate adsorption to $*NH_2$ hydrogenation, simultaneously increasing nitrate adsorption energy, resulting in sixfold higher activity than pure Cu [370]. $Ni_2P$/NF electrodes also achieved remarkable selectivity and FE (89.1% and 99.2%, respectively).

Employing cluster-centered and dual-site approaches has been shown to further elevate electrocatalytic efficiency. Gu et al. reported $Ni_6$@CuFe-LDH composites, where the incorporation of $Ni_6$ clusters strategically shifts the RDS of nitrate electroreduction from $*NH_3$ desorption to $*NO_3 \rightarrow *NO_2$ conversion, achieving a FE of 97% [371]. The composites were synthesized via electrostatic interactions and evaluated in 1 M KOH, where linear sweep voltammetry (LSV) measurements show that current density scales with $NO_3^-$ concentration, indicating an enhanced $NH_3$ production rate (Fig. 16a-b). Fig. s 16c-d illustrate the concentration-dependent e-$NO_3$RR performance, highlighting that $Ni_6$ clusters facilitate $*NH_3$ desorption through entropic compensation, thereby modulating adsorption strength and accelerating catalytic turnover. Free energy profiles for CuFe-LDH (Fe site) and $Ni_6$@CuFe-LDH (Ni site) are depicted in Fig. 16e. Although $Ni_6$ incorporation increases d–p orbital overlap near the Fermi level, COHP and PDOS analyses reveal that net bonding is weakened, favoring $*NH_3$ desorption. Charge density difference and planar-average charge analyses in Fig. 16f confirm enhanced interfacial electron redistribution, demonstrating the synergistic electronic effects of $Ni_6$ clusters in promoting efficient $NO_3^- \rightarrow NH_3$ conversion [371,373].

Zhu et al. demonstrated that $Ni_3Sn_2$-$NiSnO_x$ alloy-oxide catalysts achieve exceptional nitrate hydrogenation performance by leveraging the electronic and structural synergy between Ni and high-valent Sn [372]. The incorporation of Sn tunes Ni d-band center, suppressing the competing HER and enhancing FE, while the alloy-oxide interface creates additional active sites that stabilize $N_2$ and reaction intermediates (Fig. 16g-h). DFT calculations reveal a bifunctional mechanism in Fig. 16i. $N_2$ is activated at Ni sites, whereas adjacent Sn-modified regions promote selective hydrogenation through *H adsorption. This spatial separation facilitates the formation of $*N_2H_x$ intermediates, releases distal $NH_3$, and completes the catalytic cycle, highlighting the cooperative interface as the key to high selectivity and sustained catalytic activity [374,375]. Zhao et al. reported Ni–Mo alloys, showing bifunctional synergy where Ni facilitates $H_2O$ dissociation for proton supply, while Mo promotes nitrate adsorption and *NH hydrogenation, delivering superior $NH_3$ yields [376].

CuO/$NiO_x$-based catalysts also showcase synergistic performance. Zhang et al. synthesized CuO/$NiO_x$ on carbon paper, where Cu enhances nitrate adsorption and NiO catalyzes water splitting to generate hydrogen radicals, achieving ~97.9% FE [377]. Mo et al. reported plasma-treated NiO/Cu/$Cu_2O$ nanowires (p-CuNi@NF), facilitating proton supply for efficient nitrate hydrogenation, with FE of 97.5% and yield of 470 μmol h−1 $cm^{-2}$ [378]. Quan et al. stabilized low-valent $Cu\delta^+$ in Cu@NiO/NF electrodes, improving charge transfer and hydrogen radical generation, achieving 95.7% FE and 0.85 mg $h^{-1}$ $cm^{-2}$ $NH_3$ yield [379]. Ni and NiO-based electrocatalysts outperform monometallic or Cu-based systems by enabling tunable electronic structures, enhanced nitrate adsorption, and efficient hydrogen generation, while suppressing side reactions. Despite these advantages, challenges remain in precisely controlling coordination flexibility and active site distribution to maximize selectivity and long-term stability, offering a roadmap for rational design of high-performance $NO_3^- \rightarrow NH_3$ conversion catalysts.

**7.3.5. Other non-noble metal catalysts**: The pursuit of efficient, selective, and sustainable pathways for the electrochemical conversion of $NO_3^- \rightarrow NH_3$ has drawn significant research attention, particularly through the design of non-noble metal catalysts that provide a practical alternative to scarce and costly noble metals [56]. Among the notable advances, Zhang and co-workers pioneered nitrogen-doped carbon supports decorated with atomically dispersed bismuth centers, achieving near-complete $NH_3$ selectivity [380]. The outstanding performance was credited to the ability of isolated Bi atoms to stabilize key hydrogenated intermediates while suppressing side reactions, showing how coordination tuning can transform an earth-abundant element into a highly efficient catalyst. Expanding on this principle of structural control, Pan et al. studied nickel phosphide catalysts and revealed that the exposure of the (001) crystal facet provided the most favorable environment for nitrate adsorption and reduction [381]. Their work demonstrated the crucial role of crystallographic orientation in optimizing both activity and selectivity.

Defect engineering has also proven to be a powerful design tool. Jia et al. reported oxygen-deficient $TiO_{2-x}$ nanotube arrays, where oxygen vacancies enhanced electron transport and simultaneously created adsorption sites with high affinity for nitrate [89]. These effects translated into improved $NH_3$ yields and revealed the importance of defect-induced electronic modulation. Similarly, Deng et al. developed edge-anchored Bi–C single-atom catalysts, where bismuth atoms stabilized along carbon edges produced unique coordination environments that significantly lowered the barriers for hydrogenation and improved stabilization of intermediates [382]. This precise atomic placement provided another strong example of how structural engineering can tailor activity and selectivity.

Despite these advances, the challenges facing non-noble metal systems are considerable. Bismuth-based catalysts show excellent selectivity and their overall activity is often constrained by sluggish electron transfer, limiting achievable current densities. Long-term stability is another obstacle, for example Bi can be oxidized to $Bi_2O_3$, $TiO_{2-x}$ is prone to re-oxidation, and indium species can dissolve under operational conditions [383,384]. These transformations compromise durability and reduce catalytic efficiency. Even in stable frameworks, adsorption energy remains a delicate balance. Pan et al. observed that although $Ni_2P$ (001) promoted nitrate adsorption, excessively strong binding could trap intermediates, hindering turnover and reducing catalytic rates [381].

The role of electronic structure in defining performance is further highlighted by bismuth oxide and oxyhalide systems. Materials such as δ-$Bi_2O_3$, BiO, $BiVO_4$, and $Bi_2MoO_6$ possess conduction band levels insufficiently negative to drive efficient nitrate reduction. This mismatch suppresses selectivity and instead promotes byproducts such as nitrite, nitric oxide, and nitrous oxide. These findings illustrate the persistent challenge of electronic misalignment, insufficient adsorption prevents nitrate activation, whereas excessive binding fosters side reactions and incomplete reduction [385–388].

Extending this exploration to indium-based systems, Han et al. used DFT to analyze indium atomic chains anchored to carbon edges [389]. Their study revealed how electronic states varied depending on whether chains aligned with armchair or zigzag edges, shaped by distinct “p–p” coupling modes. While armchair edges induced $sp^2$ hybridization with localized electron density, zigzag edges promoted $sp^3$ hybridization and continuous electron bands. These differences proved decisive indium chains on zigzag edges displayed superior nitrate adsorption, ultralow

activation barriers (0.28 and 0.09 eV), and higher selectivity under neutral and alkaline conditions, effectively coupling nitrate reduction with hydrogen evolution. This work established indium atomic chains as promising candidates for selective and efficient $NO_3^-$ → $NH_3$ electrocatalysis [390].

Nazari et al. introduced an innovative route through the use of Bi–Ga liquid metal alloys [391]. By cooling the alloy under controlled conditions and applying electrical current, they generated Bi nanostructures with tunable morphologies ranging from platelets and rolled nanosheets to nanoparticles. Bi nanoparticles demonstrated the best performance for nitrate reduction, and when integrated into graphene liquid crystals, they self-assembled into layered scaffold electrodes. This architecture ensured uniform Bi dispersion, prevented catalyst aggregation, and improved ion accessibility. With the further integration of 3D printing, the system achieved high stability and industrially relevant current densities exceeding 300 mA $cm^{-2}$, offering a scalable strategy for $NH_3$ electrosynthesis [391].

Based on the recent progress, these studies build a coherent picture of the promise and challenges in designing non-noble catalysts for $NO_3^-$ → $NH_3$. These systems provide clear advantages such as abundant, structurally tunable, electronically versatile, and capable of achieving remarkable selectivity when carefully engineered. Yet persistent obstacles remain, slow electron transfer, structural instability, unfavorable band alignments, and competing side reactions continue to limit large-scale application [12,392,393]. The path forward requires integrating these lessons into rational design such as optimizing adsorption energies, stabilizing active sites through structural and electronic engineering, coupling advanced fabrication strategies, self-assembly and strain modulation. If these hurdles can be overcome, non-noble metal catalysts could progress from academic demonstrations to practical platforms, offering a sustainable and economically viable pathway for green $NH_3$ production.

### 7.4. Metal Oxide-based Materials

Metal oxides have emerged as versatile electrocatalysts for nitrate-to-$NH_3$ conversion owing to their tunable oxidation states, abundant surface oxygen vacancies, and strong adsorption capability for nitrate intermediates. Their intrinsic stability under harsh electrochemical conditions and relatively low cost make them attractive candidates compared with noble metals [396]. Defect engineering, heterostructure construction, and nanoscale tailoring have emerged as effective strategies to enhance catalytic activity and selectivity. Nonetheless, inherent limitations such as slow charge transport, poor electronic conductivity, and competitive side reactions continue to impede the realization of maximum efficiency. While these drawbacks hinder large-scale deployment, rational modifications such as doping, conductive supports, and hybridization strategies continue to improve their catalytic performance, positioning metal oxides as promising but still evolving materials in this field. Recent progress in the field has also shed light on the potential of metal oxide-based materials, and some of these notable advancements are outlined below.

**7.4.1. Titanium Oxide-based Metal Catalyst**: Titanium dioxide ($TiO_2$) is a widely studied titanium-based oxide, existing as rutile and anatase (tetragonal) and brookite (orthorhombic). The vacant 3d orbitals provide effective pathways for electron transfer, allowing $TiO_2$ to act as both an electron acceptor and transporter [396,397]. Although $TiO_2$ is chemically stable and corrosion-resistant, its intrinsic wide bandgap and limited surface-active sites restrict conductivity and electrocatalytic activity. To overcome these limitations, strategies such as creating oxygen vacancies, introducing heteroatoms, or loading metal co-catalysts (Pd, Cu, Pt) have been employed. These modifications enhance electron density, increase active sites, and improve adsorption and activation of nitrogen species ($N_2$, NO, $NO_2^-$), leading to significantly improved performance in e-$NO_3$RR and $NH_3$ synthesis [398–400]. Guo et al. fabricated a free-standing Pd/$TiO_2$ nanoarray catalyst demonstrating exceptional electrocatalytic $NO_3^-$ → $NH_3$ conversion under ambient conditions [394]. Pd doping enhances electron capture at active sites (Fig. 17a), which suppresses intermediate adsorption, and promotes $NO_3^-$ reduction. The catalyst shows a larger electrochemically active surface area (137.8 $cm^2$ vs. 115.5 $cm^2$ for $TiO_2$) and higher current densities in LSV measurements (Fig. 17b). Maximum $NH_3$ production occurs at −0.8 V vs. RHE, achieving 1.12 mg·$cm^{-2}$·$h^{-1}$ (0.066 mmol·$cm^{-2}$·$h^{-1}$), 92.1% FE, and 99.6% nitrate conversion (Fig. 17c-e). Tafel analysis in Fig. 17f confirm accelerated nitrate oxidation reaction kinetics. Integration into a Zn–nitrate battery enables simultaneous electricity generation (0.87 mW·$cm^{-2}$) and $NH_3$ synthesis (81.3% FE). Similarly, trace Cu doping (0.02%) improved conductivity and generated additional oxygen vacancies, enhancing nitrate removal and $NH_3$ selectivity [401]. Jia et al. demonstrated that hydrogen-annealed $TiO_2$ with abundant oxygen vacancies captures $NO_3^-$ efficiently, weakening N–O bonds and improving $NH_3$ selectivity [89]. DEMS and DFT analyses confirmed that $NO_3^-$ occupies these vacancies, modulating intermediate–catalyst interactions to suppress byproduct formation.

Beyond its role as a structural support, $TiO_2$ demonstrates notable activity as a co-catalyst in electrochemical processes. Fan et al. anchored Co nanoparticles on $TiO_2$ nanobelt arrays, forming Schottky contacts that generated a built-in electric field, promoting electron delocalization and achieving 800 μmol $h^{-1}$ $cm^{-2}$ $NH_3$ yield with 96.7% FE at -1 V versus RHE [363]. Cu clusters on oxygen-deficient $TiO_{2-x}$ nanosheets enhanced $NO_3^-$ adsorption and accelerated dissociation, achieving 81.34% FE at −0.95 V versus RHE [196]. Yang et al. proposed a sequential active-site-switching mechanism for Cu/Fe hetero-nanoparticle-supported $TiO_2$, where $NO_3^-$ initially adsorbs on Fe sites, reduces to $NO_2^-$, then transfers across the Cu/Fe interface and completes reduction on Cu sites [395]. This pathway enabled an $NH_3$ yield of 505.73 μg·$h^{-1}$·$cm^{-2}$ with 91.2% FE at −1.4 V vs. SCE. Electron transfer occurs via partially occupied Fe–O/Fe–N d–p π antibonding orbitals, while Cu 3d–O/N π antibonding states are fully occupied, leading to weak $NO_3^-$ adsorption and facile $NH_3$ desorption (Fig. 17g). Energy calculations confirm that Fe-$TiO_2$ favors $NO_3^-$ adsorption (−1.34 eV), whereas Cu–$TiO_2$ facilitates $NH_3$ desorption (0.35 eV), with Cu/Fe-$TiO_2$ balancing both processes (Fig. 17h). Integrating in situ ATR-SEIRAS with DFT results, the author further proposed the sequential active-site-switching pathway as the governing mechanism for e-$NO_3^-$RR on Cu/Fe–$TiO_2$ (Fig. 17i).

Structurally, $TiO_2$ exhibits valence bands from O 2p orbitals and conduction bands from Ti 3d orbitals, with empty 3d orbitals providing electron transport channels. However, its wide bandgap (3.0–3.2 eV) limits conductivity, and the limited number of active sites hinders catalytic efficiency [397,402]. Engineering oxygen vacancies or loading $TiO_2$ with metallic cocatalysts (e.g., Pd, Cu, Pt) tunes lattice oxygen electron density, increases active site density, and facilitates electron transfer to reaction intermediates [397,402,403]. Oxygen-vacancy-rich $TiO_{2-x}$ maintained 85% FE and 87.1% selectivity after eight cycles, with DEMS and theoretical studies confirming vacancy-mediated N–O bond weakening [89]. Wu et al. observed that PdCu nanoparticles on defective $TiO_2$ enhanced $NH_3$ yield (112–322.7 μmol $h^{-1}$ $cm^{-2}$) and selectivity (34.6–80.1%) through promoted electron transfer to $NO_3^-$ and strengthened Ti–O interactions, as supported by DFT calculations [404,405].

The design of heterostructure catalysts offers significant improvements in performance through synergistic effects. For instance, Co/$TiO_2$ heterointerface with Schottky interfaces, achieving high FE and 800 μmol $h^{-1}$ $cm^{-2}$ $NH_3$ yield [363]. Zhao et al. decorated $TiO_2$ nanobelts with $CoS_2$ nanoparticles, obtaining 538.21 μmol $h^{-1}$ $cm^{-2}$ yield and 92.8% FE at −0.70 V versus RHE [406]. He et al. employed $Fe_3O_4$-decorated $TiO_2$ nanobelts, achieving 729 μmol $h^{-1}$ $cm^{-2}$ $NH_3$ with 88.4% FE [407]. Chandan et al. examined $TiO_2$ supports prepared under various drying conditions for Pt impregnation in NO–$H_2$ reactions, showing that rutile-rich $TiO_2$ with lower surface area exhibited higher catalytic activity due to superior Pt dispersion, strong metal-support interactions, and optimal acidic sites [408]. Wu et al. incorporated hydrothermal carbon

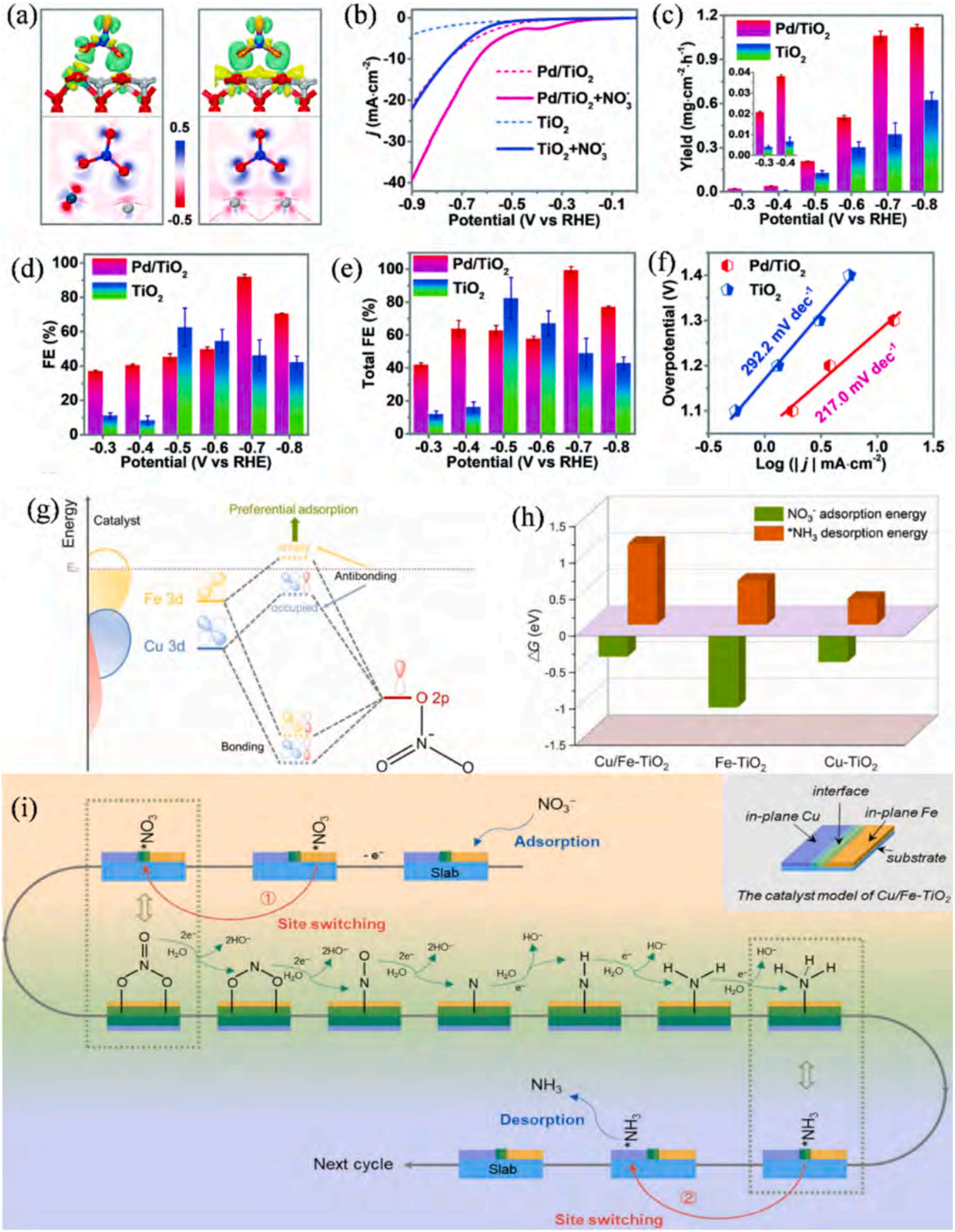



**Fig. 17.** (a) Three- and two-dimensional electron density difference maps of the optimized $Pd/TiO_2$–$NO_3^-$ and $TiO_2$–$NO_3^-$ configurations. (b) LSV responses of $TiO_2$ and $Pd/TiO_2$ in Ar-saturated electrolyte with and without 0.25 M $NO_3^-$. (c) $NH_3$ production rates, (d) FEs toward $NH_3$, and (e) overall FEs for $TiO_2$ versus $Pd/TiO_2$. (f) Tafel slopes for $NO_3^- \rightarrow NH_3$ on $TiO_2$ and $Pd/TiO_2$. (g) Conceptual representation of metal–O bond formation, with EF denoting the Fermi level. (h) Calculated free-energy profiles for $NO_3^-$ adsorption and $*NH_3$ desorption on Cu/Fe $TiO_2$, Cu–$TiO_2$, and Fe–$TiO_2$. (i) Proposed optimal pathway for $NO_3^-$ reduction, highlighting a sequential active-site switching mechanism across the Cu/Fe hetero-interface of Cu/Fe–$TiO_2$. Reproduced with permission from [394,395].

interlayers into $TiO_2$@C/$Fe_2O_3$ nanosheets, enhancing charge transfer and oxygen vacancy concentration, improving $NO_3^-$ adsorption and $NH_4^+$ yield to 0.2176 mmol $h^{-1}$ $cm^{-2}$ with 85.3% FE [409]. Yang et al. anchored Au nanoclusters on $TiO_2$ nanosheets, achieving 91% FE and 1923 μg $h^{-1}$ $mg^{-1}$ $NH_3$ yield, demonstrating the integration of e-$NO_3$RR with energy storage applications [410]. More recently, Liang *et al.* developed a three-dimensional $TiO_2$@CoFe-layered double hydroxide (LDH) hybrid on titanium plate as a highly selective electrocatalyst for the nitrite reduction reaction under alkaline conditions [411]. The catalyst delivers an outstanding $NH_3$ yield of 1056.4 μmol·$h^{-1}$·$cm^{-2}$ with a FE of 97.4% at −0.6 V vs. RHE, significantly surpassing pristine $TiO_2$ and CoFe-LDH electrodes. The $TiO_2$@CoFe-LDH/titanium plate architecture promotes efficient generation and utilization of surface hydrogen intermediates (*H_ads), accelerating $NO_2^-$ hydrogenation and sustaining $NH_3$ FE above 87% across various applied potentials. Long-term operation over 60 hours in simulated wastewater demonstrates robust stability and practical applicability. This work underscores the importance of interface engineering and active site enrichment in designing high-performance nitrite reduction reaction electrocatalysts for sustainable $NH_3$ production.

Performance can be significantly improved through the synergistic application of magnetic field regulation and heteroatom tailoring. Wang et al. demonstrated that Fe single-atom-dispersed $TiO_2$ catalysts exhibited a 3.1-fold $NH_3$ yield increase under an external magnetic field due to spin-polarized electron transfer [412]. Tongxu et al. prepared Co/$TiO_2$ nanosheets achieving 97.4% $NH_3$ FE with formation rates of 0.223-0.348 mmol $cm^{-2}$ $h^{-1}$ at −0.72 to −1.12 V versus RHE [413]. Wu et al. constructed layered Ti-Mn oxides, improving proton supply, electron transfer, and $NO_x$ hydrogenation, achieving 86.7% FE and 19.8 mg $h^{-1}$ $cm^{-2}$ nitrate reduction [414]. Lin et al. developed Co and GO co-doped $TiO_2$, achieving 7.424 mg $h^{-1}$ $cm^{-2}$ $NH_3$ yield and 56.5% FE at −1.1 V, where DFT analysis confirmed improved conductivity and uniform active site distribution [415]. Oxygen vacancy engineering, heteroatom doping, and nanoscale structural control emerge as critical strategies for enhancing electron transport, reactant adsorption, and $NH_3$ selectivity, establishing $TiO_2$-based materials as highly effective electrocatalysts for sustainable $NO_3^-$ → $NH_3$ conversion [416].

**7.4.2. Iron Oxides and Iron Hydroxides**: Fe-based oxides are widely studied electrocatalysts due to their abundance, tunable electronic structure, and multiple valence states. They occur in various crystalline forms, including pyrite (FeO), magnetite ($Fe_3O_4$), hematite (α-$Fe_2O_3$), and γ-$Fe_2O_3$ with either cubic or close-packed hexagonal structures. In these oxides, iron typically exists in +2 and +3 valence states. The $Fe^{2+}$ ion, with six 3d electrons, can adopt either high-spin or low-spin configurations, whereas $Fe^{3+}$, with a half-filled 3d orbital, possesses unpaired electrons that impart stronger magnetic characteristics [11]. This electronic configuration not only enhances charge transport but also enables efficient electron exchange during e-$NO_3$RR, where the $Fe^{2+}$/$Fe^{3+}$ redox cycle plays a central role in facilitating electron transfer to nitrate intermediates [417]. Despite these advantages, Fe-based oxides are prone to surface reconstruction during long-term operation, which can degrade their catalytic activity. To address these challenges, researchers have explored strategies such as morphology engineering, heteroatom doping, and interface construction to enhance both activity and durability. For instance, Li et al. reported the in-situ growth of $Fe_2O_3$ nanorod arrays on carbon cloth, achieving high conductivity and an $NH_3$ yield of 1.577 W/m at −0.90 V vs RHE [144]. The redox transition between $Fe^{2+}$ and $Fe^{3+}$ promoted continuous electron transfer, enabling efficient nitrate reduction with stable performance over several hours.

Doping has proven particularly effective in modulating the electronic environment of Fe oxides. Zhang et al. demonstrated that cobalt incorporation into Fe@$Fe_2O_3$, derived from a metal-organic framework, shifted the d-band center of Fe, thereby improving $NH_3$ selectivity to nearly 100% and enhancing long-term stability beyond 32 hours [418]. Similarly, Wang et al. achieved a substantial improvement in catalytic efficiency by introducing copper into $Fe_3O_4$, which strengthened the adsorption and activation of nitrate and its intermediates, ultimately lowering the reaction energy barrier [419]. Other works have further highlighted the role of composite structures and multicomponent systems. Fan et al. synthesized $Fe_3O_4$ particles directly on stainless steel substrates, which exhibited a FE of 91.5% and an $NH_3$ yield of 596.76 μmol $h^{-1}$ $cm^{-2}$ [420]. The high catalytic activity was attributed to favorable thermodynamics and a reduced barrier for the RDS. Soniya et al. designed a γ-$Fe^2O^3$/boron carbon nitride (BCN) composite catalyst that delivered a FE of 95% and excellent stability over 24 hours [421]. DFT analyses indicated that strong charge transfer between γ-$Fe_2O_3$ and BCN stabilized the active sites, explaining the enhanced performance. Further advancements were made by Ran et al. who introduced Mo and S co-doping into $Fe_3O_4$ grown on foam Fe substrates [422]. The resulting Mo-S-$Fe_3O_4$@FF nanoplates exhibited synergistic effects among Fe, Mo, and S, achieving high FE (91.3%) and $NH_3$ production rates of 123.8 μmol $h^{-1}$ $cm^{-2}$. DFT calculations and in-situ Raman spectroscopy confirmed strong electron transfer and the creation of Lewis acid-base sites that facilitated both nitrate adsorption and water dissociation. In another approach, Zhou et al. engineered mesoporous $FeO_x$ using SBA-15 templating, significantly increasing surface area and charge transfer efficiency [417]. A novel pre-activation strategy allowed modulation of the $Fe^{3+}$/$Fe^{2+}$ ratio, yielding optimized adsorption-desorption dynamics for nitrate reduction. The catalyst achieved an $NH_3$ yield rate of 255.40 μmol $cm^{-2}$ $h^{-1}$ with a FE above 91%, demonstrating that coupling geometric confinement with electronic regulation can overcome conventional catalytic scaling limits.

The introduction of ternary configurations marks an important step forward in catalyst design. Kang et al. fabricated a CuZnFe layered double hydroxide catalyst supported on carbon cloth [423]. This material delivered a FE of 95%, an $NH_3$ yield of 51 mg $h^{-1}$ $cm^{-2}$, and long-term durability exceeding 100 hours. Operando spectroscopic analyses revealed that dynamic reconstruction of the catalyst generated synergistic active sites, where Cu facilitated nitrate-to-nitrite reduction and Fe enabled nitrite-to- $NH_3$ conversion, with Zn leaching further exposing active surfaces. Defect engineering offers another effective strategy. Liu et al. synthesized FeOOH nanorods enriched with oxygen vacancies, which exhibited an $NH_3$ yield of 2419 μg $h^{-1}$ $cm^{-2}$ and a FE of 92% [424]. DFT calculations revealed that oxygen vacancies lowered the energy barrier for the potential-determining step and simultaneously suppressed competing hydrogen evolution, thereby improving $NO_3^-$ → $NH_3$ selectivity. Perovskite-type oxides have also been exploited. Yin et al. introduced A-site deficiencies in $LaFeO_{3-\delta}$, generating oxygen vacancies that promoted nitrate adsorption and weakened N–O bonds, thereby enhancing $NH_3$ production [425]. The optimized catalyst ($La_{0.9}FeO_{3-\delta}$) achieved an $NH_3$ yield of 1024.8 μg $h^{-1}$ $cm^{-2}$ and a maximum FE of 78.1%. Zhao et al. constructed a $Fe_2O_3$/ZnO heterojunction that significantly improved interfacial electron transfer and exposed additional active sites [426]. This catalyst exhibited a FE of 97.4% and an $NH_3$ yield of 6327.2 μg $h^{-1}$ $cm^{-2}$, with DFT calculations confirming that the heterostructure reduced the energy barrier for the RDS. Above studies underscore that while Fe-based oxides are intrinsically less active than noble metals, their tunable electronic structure, abundance, and adaptability to structural and compositional engineering make them highly promising for sustainable $NO_3^-$ → $NH_3$ conversion. Advances in doping, defect engineering, heterostructure design, and electronic regulation continue to expand the scope of Fe-based oxides as cost-effective, stable, and high-performance electrocatalysts [427,428].

**7.4.3. Co Oxide and Doped Co Oxide**: Cobalt-based catalysts have swiftly risen to prominence as leading materials for the e-$NO_3$RR. Their unique advantage lies in the rare union of earth-abundant availability, remarkable electronic flexibility, and catalytic adaptability, enabling them to deliver high selectivity and activity while remaining cost-effective. The capacity of cobalt to finely adjust electronic states and expose dense arrays of active centers ensures not only the efficient conversion of $NO_3^-$ → $NH_3$ but also a significant suppression of the

competing HER. As a result, cobalt-based systems consistently exhibit outstanding FE, high $NH_3$ production rates, and robust performance over prolonged operation [15]. One of the central scientific puzzles has been identifying the precise cobalt species responsible for catalytic activity. He et al. provided a landmark study by systematically comparing spinel oxides such as $Co_3O_4$, $MgCo_2O_4$, and $CoAl_2O_4$ [429]. Their findings established octahedral cobalt ($Co_{Oh}$) as the dominant catalytic site, whereas tetrahedral cobalt ($Co_{Td}$) played an almost negligible role. The introduction of oxygen vacancies ($O_v$) was shown to significantly boost the reactivity of $Co_{Oh}$ by modulating its electronic configuration and reducing the energy barrier of the rate-limiting step (Fig. 18a-b). Interestingly, substitution with $Cu^{2+}$ produced a volcano-shaped activity trend, emphasizing that deliberate electronic tuning of $Co_{Oh}$ is the key to maximizing catalytic efficiency (Fig. 18c). Moreover, Kaiwen et al. demonstrated that both Co and CoP catalysts follow a relay-like mechanism at low overpotentials, involving spontaneous redox transitions, electrochemical regeneration of metallic Co, and subsequent hydrogenation of $NO_2^-$ [21]. At higher potentials, however, a direct hydrogenation route became dominant. Notably, CoP@Co surpassed pure Co in efficiency because electron donation from its phosphide core enhanced *H generation while suppressing hydrogen gas release (Fig. 16d-f).

Beyond tuning active sites, the rational control of catalyst morphology has proven essential for optimizing activity and selectivity. Lin et al. reported that dense membranous cobalt films achieved nearly 100% FE at −0.2 V vs. RHE [431], while Deng et al. showed that cobalt nanoarrays facilitated water dissociation, expediting both *H adsorption and nitrate conversion in alkaline electrolytes [432]. Building upon this, the transformed $Co(OH)_2$ nanosheets into metallic $Co^0$ nanoarrays via in situ reduction, producing extraordinary $NH_3$ yields exceeding 10 mmol $h^{-1}$ $cm^{-2}$ with an achievement underscoring the power of controlled structural design [432]. Conductive support materials further enhance catalytic behavior. Xie et al. demonstrated that Co nanoparticles immobilized on biomass-derived carbon reached 93.4% FE with excellent long-term stability [433]. Similarly, Chen et al. designed Co/N-doped carbon nanospheres using adenine-based MOFs achieved an impressive FE of 96.5% and an $NH_3$ yield rate of 758.0 μmol $h^{-1}$ $mgcat.^{-1}$, even under extended electrolysis conditions [108].

The deliberate integration of alloying and heteroatom doping unlocks a new horizon of catalytic tunability. Xiaoya et al. showed that Pd-doped $Co_3O_4$ nanoarrays benefited from Pd-induced shifts in the cobalt d-band center, enhancing $NO_3^-$ adsorption and reducing reaction barriers [434]. Qiao et al. demonstrated that Ni doping drove surface reconstruction into $Co_yNi_{1-y}(OH)_2$ phases, improving *NOH stabilization and suppressing HER, which delivered efficiencies above 94% (Fig. 18g-j) [430]. Meanwhile, Xia et al. developed CoW foams, where charge redistribution between Co and W significantly improved intermediate adsorption, yielding $NH_3$ production rates above 160 mg $h^{-1}$ $cm^{-2}$ with nearly perfect selectivity [435]. Defect modulation has emerged as a powerful approach, yielding substantial enhancements in catalyst behavior. Zhao et al. synthesized oxygen-vacancy-rich $Co_3O_4$/Co nanosheets that enhanced $NO_3^-$ adsorption and lowered the energy barrier for *NO conversion [436]. Extending this idea, Deng et al. produced Co-vacancy-rich $Co_3O_4$ arrays, which consistently delivered FE values above 97% and markedly outperformed vacancy-free analogues [355]. Among cobalt compounds, cobalt phosphides (CoP) remain especially compelling because of their adaptable electronic structures. Li et al. showed that CoP alloy films supported on Ti plates performed exceptionally in neutral conditions [437]. Ye et al. demonstrated that CoP nanosheets on carbon cloth could reach nearly 100% FE [113], while Kui et al. introduced hollow CoP nanospheres confined in carbon nanosheets, striking a fine balance between *H generation and consumption [438]. Mechanistic insights from Kaiwen et al. revealed that CoP surfaces dynamically reconstruct into $Co(OH)_2$ intermediates, which revert to metallic Co under operational conditions [21]. Consistently, CoP@Co surpassed both Co and $Co_3O_4$ in catalytic efficiency.

The synergistic advantages inherent in bimetallic and multimetallic systems have also been recognized. Kouer et al. prepared Cu–Co branched nanowires in which Co(111) facilitated the $NO_3^-$ to $NO_2^-$ step, while Cu(111) drove subsequent hydrogenation, enabling gram-scale production with >91% FE [149]. Fang et al. fabricated $Cu_{50}Co_{50}$ nanosheets that optimized the adsorption energies of both $*NO_3$ and *H, achieving ultrahigh current densities and nearly 100% FE [170]. Rundong et al. expanded the concept with Bi–Co corridor structures, producing FEs of 99.5% and remarkable stability [439]. Self-assembly strategies have further broadened design options. Zhang et al. embedded CoP nanoparticles in Zn–ZIF matrices, where electrostatic interactions enhanced nitrate transport and $NH_4^+$ release [20]. Kim et al. integrated polyaniline with $Co_3O_4$/CNT composites, creating nitrate-rich microdomains that reduced energy requirements while increasing efficiency [440]. Han et al. later proposed a three-step relay pathway, optimized through Ru–Co hollow nanostructures, with $Ru_{15}Co_{85}$ achieving FE values close to 97% alongside long-term durability and energy efficiencies above 40% [441].

Interfacial engineering enables precise control of interfaces to improve functionality. Yunfei et al. reported that $CoO_X/Fe_3O_4$-90, containing interfacial oxygen vacancies, delivered 82.22% FE at −0.9 V and an $NH_3$ yield of 1.09 mmol $h^{-1}$ $cm^{-2}$ at −1.1 V [442]. Their work revealed that a balanced oxygen vacancy concentration enhances electron transfer and optimizes $NO_3^-$ adsorption configurations, though excess vacancies risk catalyst poisoning by strong NO* binding. Wang et al. developed Pd-$CoO_x$ catalysts via electrodeposition, achieving nearly 99% FE [443]. The $CoO_x$ promoted $Pd^{2+}$ formation and facilitated $NO_3^-$ adsorption, while simultaneously lowering intermediate energy barriers. Sun et al. synthesized CuCo–CoO composites with dual alloy–oxide functionalities, producing $NH_3$ at 12.63 mmol $h^{-1}cm^{-2}$ and maintaining high stability over 48 h [444]. Liu et al. designed amorphous a-CoO/$Cu_2O$ heterojunctions, where synergistic cascade effects enabled FE up to 95.72% and outstanding yield rates. Further advances include Shi et al.'s $Co_6Ni_4$ heterostructures, where Ni tuned Co's electronic states to prevent unwanted reconstruction, enabling FEs above 90% over a wide potential window [351]. Dai et al. constructed CoO/B heterojunctions that exposed abundant active sites, achieving 29.42 mg $h^{-1}$ $mgcat^{-1}$ yields with 95.41% FE [445]. Li et al. introduced Cu–Co nanoparticles on porous carbon, obtaining 9114.1 μg $h^{-1}$ $cm^{-2}$ yields with confirmed 15N isotope labeling [25]. Xue et al. reported np-CuCo catalysts that dynamically evolved into Cu/CoOOH heterostructures during operation, enhancing $*NO_2$ binding and lowering energy barriers [446]. Zhong et al. fabricated tribenzaldehyde (TTA)- terephthalohydrazide (TPH)-CuCo catalysts with tandem sites, reaching 20.8 $mgh^{-1}cm^{-2}$ yields and unraveling cascade mechanisms through in situ characterization [150]. Xu et al. introduced $Mo^{5+}$ into $Co_3O_4$ to form $CoMoO_4$, achieving yields of 1481.49 μg $h^{-1}$ $mg^{-1}$cat with a unique mechanistic pathway involving *NO → *NHO intermediates [447].

The above advancements reveal the extraordinary versatility of cobalt-based catalysts. From defect-rich oxides and phosphides to bimetallic frameworks and heterostructures, cobalt materials offer a vast design space that integrates morphology, doping, electronic tuning, and self-assembly [448,449]. Yet, despite these advances, open questions remain about the true active species and mechanistic intricacies. Progress will depend on bridging operando spectroscopic insights with theoretical modeling, ultimately guiding the rational design of next-generation cobalt catalysts for sustainable and scalable $NH_3$ synthesis.

**7.4.4. Spinel Oxide Catalyst**: The catalytic versatility of spinel oxides has recently drawn significant attention for e-$NO_3$RR, with both compositional tuning and defect engineering strategies proving highly effective. A range of studies demonstrate how structural modulation, cation substitution, and facet exposure can dramatically alter performance [450–453]. Hu et al. revealed that the performance of $Co_3O_4$ is intrinsically dependent on the coordination environment of cobalt [429]. Their work showed that nitrate reduction occurs preferentially at octahedral Co ($Co_{Oh}$) sites rather than tetrahedral ones ($Co_{Td}$). During

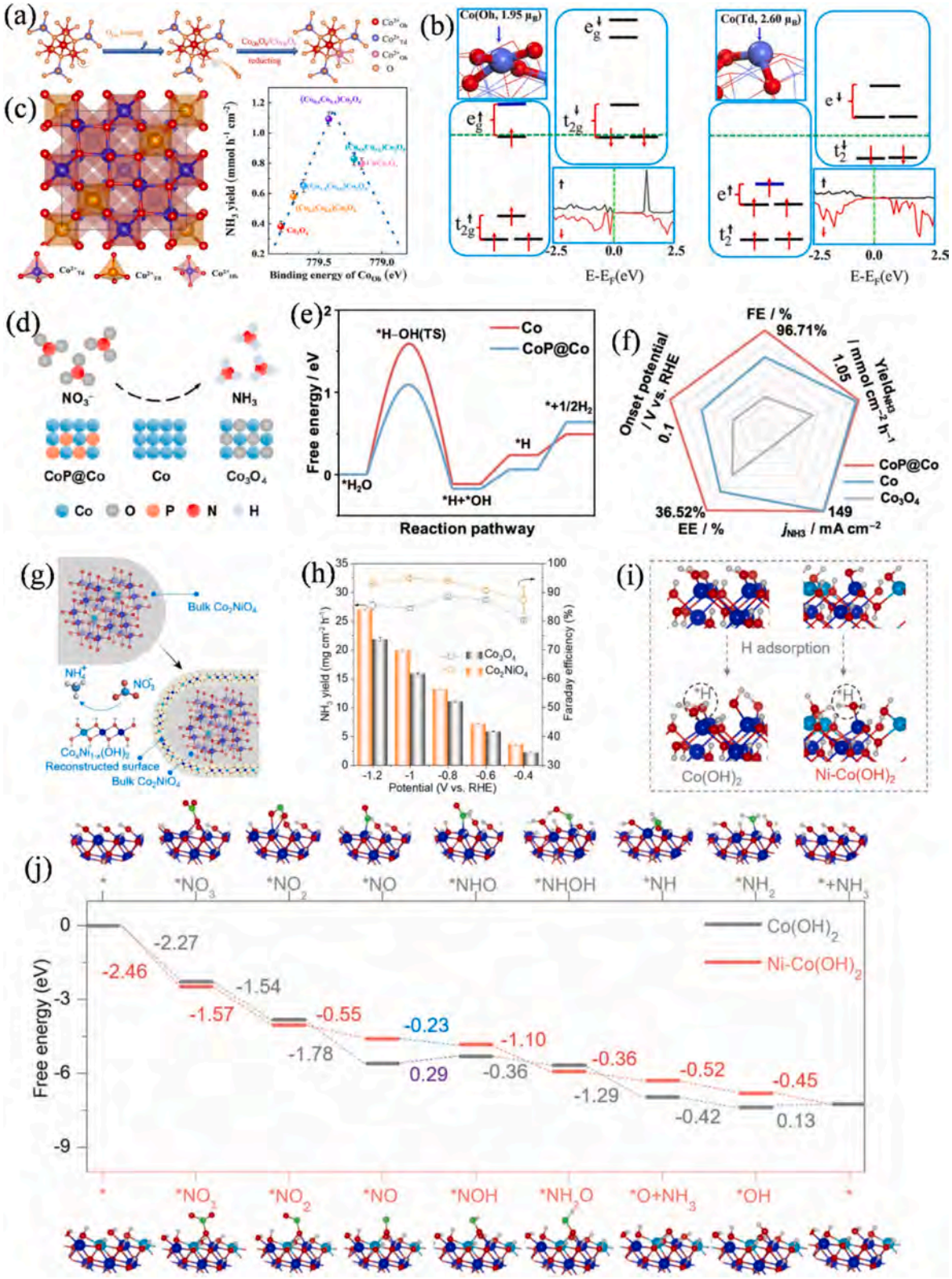



**Fig. 18.** (a) Schematic representation of the generation pathway for $Co^{2+}_{Oh}$-$O_v$. (b) Spin-polarized crystal-field splitting diagrams for $Co_{Oh}$ and $Co_{Td}$, alongside their local coordination geometry, intrinsic magnetic moment (single Co atom), and projected density of states (DOS) (Co 3d). The Fermi energy is indicated by green dashed lines across both the crystal-field and DOS plots. (c) Crystal framework of $Co_{Oh}$ and the volcano-type correlation observed between $NH_3$ production rates and the binding energies. (d) Comparative schematic of CoP@Co, metallic Co, and $Co_3O_4$ in nitrate reduction activity (NRA) testing. (e) Free-energy profiles of hydrogen evolution (HER) on CoP@Co and metallic Co. (f) Consolidated metrics $FE_{NH3}$, $Yield_{NH3}$, $j_{NH3}$, and $EE_{NH3}$ at both the optimum and onset potentials across model catalysts for NRA. (g) Conceptual scheme of surface restructuring on $Co_2NiO_4$ electrodes during e-$NO_3$RR. (h) Experimental comparison of $NH_3$ yields and FEs for $Co_2NiO_4$ and $Co_3O_4$ under varying applied potentials. (i) Structural models for H adsorption on oxygen sites of pristine $Co(OH)_2$ (101) and Ni doped $Co(OH)_2$ (101) slabs (color coding: dark blue = Co, red = O, cyan-blue = Ni). (j) Energy diagrams outlining e-$NO_3$RR pathways on undoped versus Ni-modified $Co(OH)_2$. Reproduced with permission from [21,429,430].

operation, $Co_{Oh}O_6$ sites undergo electrochemical transformation into oxygen-deficient $Co_{Oh}O_5$ configurations, which emerge as the true active centers. Importantly, partial substitution of $Co_{Td}$ sites with $Cu^{2+}$ cations optimizes the local electronic structure of $Co_{Oh}$, leading to a volcano-shaped activity trend. Remarkably, $(Cu_{0.6}Co_{0.4})Co_2O_4$ reached a FE of 96.5% with an $NH_3$ yield of 1.09 mmol $h^{-1}$ $cm^{-2}$ at −0.45 V vs RHE, surpassing most reported non-precious electrocatalysts [429]. Surface orientation also governs activity, as demonstrated by Zhu et al. who identified the {111} facet of $Co_3O_4$ as the most favorable surface for alkaline nitrate reduction [345]. Structural evolution studies indicated that under electrochemical conditions, $Co_3O_4$ dynamically transforms into defect-rich $Co_3O_{4-x}$–$O_v$ and $Co(OH)_2$ phases, with the {111} surface generating oxygen vacancies at the fastest rate. DFT calculations confirmed that $O_v$ formation on {111} reduces the free energy barrier of $*NH_2$ formation from 1.81 eV to −0.53 eV, enabling highly selective $NH_3$ production. Indeed, the {111} facet achieved a yield rate of 35.2 ± 0.6 mg $h^{-1}$ $cm^{-2}$ and an FE of 99.1 ± 1.8% at −0.6 V vs RHE [454,455].

Tailoring spinel frameworks through cation substitution has proven highly effective in modulating their catalytic properties. Xupings's group systematically synthesized $MCo_2O_4$ spinel oxides (M = Ni, Fe, Zn) on carbon cloth and demonstrated that these catalysts consistently achieved higher FE (>95%) than pristine $Co_3O_4$ [454,456]. Among them, $NiCo_2O_4$ delivered an outstanding $NH_3$ yield of 17.52 mg $h^{-1}$ $cm^{-2}$ at −0.6 V vs RHE, which was attributed to improved electronic conductivity and reduced overpotential [172]. Another work showed that $CoMn_2O_4$ embedded in carbon nanofibers reached 1041.1 μg $h^{-1}$ $cm^{-2}$ with 92.4% FE at −0.7 V, where strong interactions between the oxide and carbon facilitated electron delocalization, simultaneously suppressing HER and enhancing nitrate conversion [454]. Beyond cobalt spinels, $Fe_3O_4$ and its derivatives have also been investigated. Xuping's group reported that $Fe_3O_4$ particles achieved an $NH_3$ yield of 10.145 mg $h^{-1}$ $cm^{-2}$ with 91.5% FE at −0.5 V vs RHE in alkaline conditions [420]. Subsequent modification with low-content Cu (6.1 wt%) by Jing et al. and boosted FE to nearly 100% by strengthening nitrate adsorption and lowering the limiting potential of the RDS [419]. In parallel, $Fe_3O_4$–$TiO_2$ hybrids demonstrated significantly improved performance in neutral media, reaching 12.393 mg $h^{-1}$ $cm^{-2}$ at −0.9 V, outperforming both pristine components reported by Xun et al [407]. More recently, He *et al.* developed a La-$Co_3O_4$ nanowire array anchored on carbon cloth as a highly efficient electrocatalyst for e-$NO_3$RR [457]. The La-$Co_3O_4$/carbon cloth electrode achieves an outstanding $NH_3$ FE of 96.36% and a production rate of 537.44 μmol·$h^{-1}$·$cm^{-2}$, markedly surpassing the undoped $Co_3O_4$ analogue (87.78%, 279.4 μmol·$h^{-1}$·$cm^{-2}$). DFT analyses indicate that La doping enhances nitrate adsorption and optimizes proton-coupled electron transfer pathways, thereby facilitating the hydrogenation process and selectively promoting $NH_3$ formation. Furthermore, the La-$Co_3O_4$/carbon cloth electrode functions as an effective cathode in a Zn–$NO_3^-$ battery, delivering a peak power density of 9.86 mW·$cm^{-2}$. This work underscores the strategic utility of rare-earth element doping in tailoring electronic structure and active site reactivity, offering a promising avenue for the rational design of $Co_3O_4$-based electrocatalysts for high-efficiency and sustainable e-$NO_3$RR.

Defect modulation has become a powerful strategy in tailoring catalyst behavior. Lai et al. developed Zn-deficient $ZnCo_2O_4$ ($VZn$–$ZnCo_2O_4$) through electrochemical etching, generating extensive lattice distortion and abundant active sites [26]. The defective catalyst achieved a maximum FE of 94.5% and an $NH_3$ production rate of 2.79 mg $h^{-1}$ $cm^{-2}$ at −0.5 V vs RHE. Theoretical calculations confirmed that Zn vacancies enhanced nitrate adsorption and reduced the energy barrier for the RDS ($*NH_2O$ → $*NH_2OH$) from 0.44 eV to 0.24 eV, while simultaneously suppressing HER. A Zn-$NO_3^-$ battery incorporating this catalyst further demonstrated its potential in practical energy systems. High-entropy oxides have also expanded the design paradigm. Shi et al. reported that (Mn, Fe, Co, Ni, Cu)3O4 exhibited exceptional electrocatalytic activity for $NH_3$ oxidation in non-aqueous systems [458]. This material displayed an onset potential nearly 0.2 V lower than the most active single-metal counterpart and achieved >85% FE toward $N_2$ formation. XPS analysis suggested that the balanced d-band structure of Mn and Cu stabilized the catalyst, enabling long-term activity. These diverse strategies from facet engineering and cation substitution to defect creation and entropy-driven design underscore the versatility of spinel oxides for $NO_3^-$ → $NH_3$ conversion. The convergence of electronic structure modulation, defect stabilization, and dynamic phase evolution points toward rational strategies for next-generation electrocatalyst development.

**7.4.5. Perovskites Oxide Catalysts**: Perovskite oxides have recently emerged as a versatile class of catalysts for the e-$NO_3$RR to $NH_3$, owing to their flexible lattice composition and ability to accommodate oxygen defects and variable valence states. While the structural adaptability of the $ABO_3$ framework provides a foundation for catalyst design, recent progress has been driven primarily by targeted compositional engineering and mechanistic studies [459,460]. In particular, systematic investigations by several researchers have collectively advanced the understanding of how oxygen vacancy density, cation substitution, A-site deficiency, and nanoparticle exsolution can be harnessed to enhance the performance [3,461]. Hui et al. investigated a series of lanthanum-based perovskite oxides, specifically $LaCrO_3$, $LaMnO_3$, $LaFeO_3$, and $LaCoO_3$, and observed a performance trend of $LaCrO_3$ < $LaMnO_3$ < $LaFeO_3$ < $LaCoO_3$ [462]. The superior performance of $LaCoO_3$ was attributed to its higher oxygen vacancy concentration, which facilitated the RDS of nitrate reduction, namely the conversion of adsorbed nitric acid intermediates to nitrite. The present study achieved FE close to 90%, establishing oxygen vacancy engineering as a decisive factor in promoting selective $NH_3$ production. Notably. $LaCoO_3$ with its hexagonal phase and highest oxygen vacancy concentration exhibited the best catalytic performance. DFT analysis confirmed that oxygen vacancies stabilize intermediates and reduce energy barriers for the successive reduction steps. Qi et al. synthesized copper-, manganese-, and cobalt-doped $LaFeO_3$ and found that copper-doping achieved the highest performance due to the cooperative redox activity of copper ions and increased oxygen vacancy concentration, producing $NH_3$ yield rates up to 1005 μg $h^{-1}cm^{-2}$ [463]. The author further extended this approach by introducing lanthanum deficiency into $LaFeO_3$, thereby significantly increasing oxygen vacancy density and suppressing the competing hydrogen evolution reaction. This modification yielded enhanced selectivity for $NH_3$ formation, underscoring the critical role of A-site non-stoichiometry in tuning electronic structure and defect chemistry. Recently, Lv et al. strategically engineered oxygen vacancies in $LaMnO_3-\delta$ nanofibers through A-site La deficiency, copper doping, and controlled hydrogen etching, yielding a gradient distribution of defects [464]. The optimized catalyst, etched $La_{0.9}Mn_{0.5}Cu_{0.5}O_3-\delta$, possessing the highest oxygen vacancy density, delivers a remarkable $NH_3$ FE of 90.1% and an $NH_3$ yield of 28.1 mg $h^{-1}$ $mg_{cat}^{-1}$. The results indicate that nitrate reduction proceeds efficiently on the catalyst surface, with sequential deoxygenation and hydrogenation processes facilitated by the defect-rich structure. DFT calculations show a favorable nitrate adsorption free energy of −0.14 eV on $La_{0.9}Mn_{0.5}Cu_{0.5}O_3-\delta$, with d-band centers of La and Cu at −1.97 eV and −2.66 eV, respectively, highlighting strong electronic interactions between reactive intermediates and active sites. The concentration of oxygen vacancies is directly correlated with enhanced electrocatalytic performance. Increased electronic conductivity along the nanofibers promotes charge accumulation and accelerates electron transfer, further improving e-$NO_3$RR. This effort demonstrates a rational defect-engineering strategy in perovskite oxides, emphasizing the synergistic effect of oxygen vacancies and transition metal doping in achieving high-efficiency, stable electrocatalysis.

Engineering oxygen vacancies in perovskite oxide with in-situ embedded metallic nanoparticles optimizes the interfacial electronic structure, enhancing active site availability and promoting efficient nitrate reduction. Hu et al. developed FeCo alloy nanoparticles via exsolution from Co-doped $Sm_{0.9}FeO_3$ nanofibers with abundant oxygen

vacancies, establishing an efficient electrocatalyst for e-$NO_3$RR [465]. The catalyst delivers a maximum FE of 90.3 % and an $NH_3$ production rate of 17.2 mg $h^{-1}$ $mg^{-1}_{cat}$ at −0.9 V, while retaining remarkable stability under prolonged electrolysis. The synergistic interplay between exsolved FeCo and oxygen vacancy enhances nitrate adsorption, optimizes electron distribution, and lowers the energy barrier of the potential-determining step, favoring the $NH_2OH$-mediated reaction pathway. Finite-element simulations reveal that charge density and current are concentrated on the FeCo nanoparticles along the nanofibers, confirming their role as the principal active sites. This approach demonstrates the effectiveness of integrating defect engineering with controlled nanoparticle exsolution to maximize active site exposure and electronic modulation for high-performance $NH_3$ electrosynthesis. More recently, Xu et al. demonstrated that PdNi alloy nanocrystals, generated via Pd deposition on $La_{0.52}Ca_{0.28}Ni_{0.06}Ti_{0.94}O_3$ perovskite oxide nanofibers, function as highly efficient electrocatalysts for the e-$NO_3$RR [466]. The catalyst delivers an exceptional $NH_3$ yield of 21.13 mg $h^{-1}$ $mg^{-1}_{cat}$ (≈4226 mg $h^{-1}$ $mg^{-1}$ Pd) and a maximum FE of 98.78 % at −1.0 V. Theoretical analyses reveal that the interface between the PdNi nanocrystals and the oxygen-vacancy-rich perovskite enhances nitrate adsorption and hydrogenation while suppressing the HER, effectively lowering the energy barrier of the potential-determining step. By harnessing the synergy between perovskite oxides and metallic nanophases, the e-$NO_3$RR can be significantly optimized, offering a compelling strategy.

Doping strategies have also been widely explored to optimize B-site electronic properties. Gong et al. investigated cobalt, nickel, and zinc dopants in $LaCu_2O_4$ and demonstrated that cobalt doping yielded the strongest metal-oxygen hybridization, which improved adsorption of intermediates and enhanced $NH_3$ selectivity [467]. He further correlated metal-oxygen hybridization strength directly with nitrate coverage, identifying $La_2Cu_{0.8}Co_{0.2}O_4$ as the most favorable composition for selective nitrate reduction. A-site engineering has proven equally effective. Liu et al. synthesized cobalt-based perovskites with controlled A-site deficiencies, specifically $(Ba_{0.5}Sr_{0.5})_{1-x}Co_{0.8}Fe_{0.2}O_{3-\delta}$, which enabled systematic tuning of oxygen vacancy density and electronic band positions [468]. The optimized composition with a 15% deficiency achieved nearly 98% FE and maintained stability over 200 hours of operation. The improvement was attributed to stronger nitrate adsorption at vacancy sites combined with electronic redistribution caused by A-site deficiency.

Structural reconstruction and nanoparticle exsolution strategies have been shown to further enhance performance. $BiFeO_3$ nanosheets were reported to reconstruct into amorphous phases during electrocatalysis, achieving FE up to 96.8% [469]. Hu et al. developed SmFeCoO nanofibers that enabled the in situ exsolution of FeCo alloy nanoparticles, where oxygen vacancies improved conductivity and nitrate adsorption [465]. Xu et al. designed PdNi-decorated perovskites using exsolution, which achieved nearly 99% FE and high $NH_3$ yield rates [466]. Computational results confirmed that the synergy between the exsolved nanoparticles and the perovskite lattice reduced the energy barriers for nitrate reduction. More recently, Feng et al. expanded this research beyond lanthanum- and cobalt-based systems by developing $NbWO_6$ nanosheets with abundant oxygen vacancies [397]. The defect states shifted the Fermi level toward the conduction band minimum, imparting metallic conductivity and enhanced nitrate adsorption. This led to substantially lower adsorption energies and improved selectivity toward $NH_3$ compared to pristine $NbWO_6$, demonstrating the broader applicability of oxygen vacancy engineering in unconventional perovskite systems.

Based on the above recent achievements, it can be readily understood that perovskite oxides can be precisely engineered through oxygen vacancy creation, A- and B-site modification, and dynamic structural reconstruction to achieve outstanding catalytic performance in the electrochemical reduction of $NO_3^- \rightarrow NH_3$. Similarly, cobalt- and iron-based oxides, spinels, and doped metal oxides demonstrate exceptional versatility, offering tunable electronic structures, abundant active sites, and defect-rich surfaces that enhance nitrate adsorption, electron transfer, and selective hydrogenation pathways. The deliberate design of heterostructures, alloying, and nanoparticle exsolution further amplifies synergistic effects, leading to high FEs, elevated $NH_3$ yield rates, and long-term operational stability. These materials benefit from earth-abundant availability and cost-effectiveness compared with noble metals, while strategies such as oxygen vacancy engineering and interface optimization effectively suppress competing hydrogen evolution reactions. However, challenges remain such as slow intrinsic electron transport, potential surface reconstruction, and partial instability under prolonged operation can limit large-scale applicability. Despite these limitations, recent advances highlight a promising path forward where rational structural, compositional, and electronic tuning can unlock next-generation electrocatalysts. These developments underscore the substantial potential of perovskite, cobalt, iron, and spinel oxide-based materials as high-performance, scalable, and sustainable platforms for electrochemical nitrate-to-$NH_3$ conversion, paving the way for practical $NH_3$ synthesis under ambient conditions [470].

## 8. Conclusion and Future Perspectives

The e-$NO_3$RR has emerged as a transformative strategy at the intersection of environmental remediation and sustainable energy conversion. Beyond offering an eco-friendly alternative to the Haber–Bosch process, e-$NO_3$RR directly addresses nitrate contamination in water systems while generating $NH_3$ as a value-added chemical and energy carrier. This review has provided a comprehensive overview of recent progress in catalyst design, mechanistic understanding, system optimization, and advanced characterization, with emphasis on nanostructured materials, synergistic interfacial effects, and computational insights. Collectively, these advances underscore the immense promise of nanomaterials in tailoring electronic configurations, stabilizing reaction intermediates, and driving selectivity toward $NH_3$ under practical conditions. Table 2 outlines a consolidated comparison of benchmark catalysts, highlighting representative examples across diverse catalyst classes.

Despite encouraging achievements, the transition from laboratory success to scalable technology requires addressing several grand challenges:

***Mechanistic Clarity and Active Site Identification***: Despite substantial advancements in the design and development of electrocatalysts, the fundamental mechanisms underlying the e-$NO_3$RR to $NH_3$ remain incompletely understood. The presence of competing pathways including $NO_2^-$ formation, NO intermediates, and hydrogen-assisted side reactions obscures the origins of selectivity and constrains rational optimization of catalytic performance. Transient intermediates, dynamic surface restructuring, and electronic modulation of active sites critically govern reaction kinetics, intermediate stability, and product distribution. Achieving mechanistic clarity thus requires the integration of advanced in situ and operando spectroscopic techniques, such as Raman spectroscopy, XAS, FTIR, DEMS, and electrochemical scanning tunneling/transmission electron microscopy (EC-STM/TEM), with ab initio calculations, DFT, and machine-learning-assisted simulations. These synergistic approaches enable real-time monitoring of reaction intermediates, precise identification of site-specific activity, and direct correlation between surface structure, electronic states, and catalytic function. At the atomic level, strategies including defect engineering, heterostructure and composite catalyst fabrication, and interface modulation provide precise control over active site density, electronic structure, and adsorption energies of nitrate and intermediate species. Hierarchical porosity, surface functionalization, and tailored nanostructuring enhance mass transport, facilitate reactant accessibility, suppress side reactions, and favor selective $NH_3$ generation. Moving forward, rational catalyst design guided by predictive modeling and artificial intelligence will be pivotal for selecting optimal catalytic

**Table 2**
Benchmark advanced catalysts and their achievements in e-$NO_3$RR.

| No | Name of Catalyst | Over potential | $NH_3$ Yield rate | FE (%) | Ref |
|---|---|---|---|---|---|
| 1 | CuPd(3:1) | −0.46 $V_{RHE}$ | 784.37 $\mu g h^{-1} mg_{cat}^{-1}$ | 90.02% | [224] |
| 2 | B/Fe-$Co_2P$ HNCs | / | 22.67 mg $h^{-1}$ $mg_{cat}^{-1}$ | 97.54% | [478] |
| 3 | $A^5Fe_2O_4$ | / | 2.1 mmol $h^{-1}$ $cm^{-2}$ | 98.10% | [333] |
| 4 | $Fe_3O_4$/SS | −0.5 $V_{RHE}$ | 10145 $\mu g h^{-1} cm^{-2}$ | 91.50% | [479] |
| 5 | $Bi_1Pd$ | / | 33.8 mg $h^{-1}$ $cm^{-2}$ | 100% | [232] |
| 6 | $Fe_2P$ | / | 4.25 mg $h^{-1}$ $cm^{-2}$ | 96.00% | [480] |
| 7 | Nano-Ag | −0.33 $V_{RHE}$ | / | 96.40% | [481] |
| 8 | La-$Co_3O_4$/CC | / | 537.44 μmol $h^{-1}$ $cm^{-2}$ | 96.36% | [457] |
| 9 | $V_{Cu}$-$Au_1Cu$ | / | 555 μg $h^{-1}$ $cm^{-2}$ | 98.70% | [482] |
| 10 | $ZnCo_2O_4$ | −0.6 $V_{RHE}$ | 2100 $\mu g h^{-1} mg^{-1}$ | 95.40% | [483] |
| 11 | $FeB_2$ | / | 25.5 mg $h^{-1}$ $cm^{-2}$ | 96.80% | [336] |
| 12 | $FeNi_{500}$/FF | / | 0.21 mg $h^{-1}$ $cm^{-2}$ | 97.20% | [484] |
| 13 | $Cu_2O$(100) | −0.6 $V_{RHE}$ | 743 $\mu g h^{-1} mg_{cat}^{-1}$ | 82.30% | [485] |
| 14 | $Ni_2FeP$@NC | / | 0.47 mmol $h^{-1}$ $cm^{-2}$ | 93.00% | [486] |
| 15 | $Fe_3O_4$/SS | / | 10.1 mg $h^{-1}$ $cm^{-2}$ | 91.50% | [420] |
| 16 | Cu@Th-BPYDC | 0 $V_{RHE}$ | 225.3 $\mu mol h^{-1} cm^{-2}$ | 92.50% | [487] |
| 17 | NGQDs-Fe | / | 15.41 mmol $h^{-1}$ $cm^{-2}$ | 93.00% | [488] |
| 18 | $Fe_3O_4$@$TiO_2$/TP | / | 210.8 mg $h^{-1}$ $cm^{-2}$ | 88.40% | [407] |
| 19 | SWCNT | −0.85 $V_{RHE}$ | / | 90.00% | [129] |
| 20 | CoP-CNS | / | 3.06 mg $h^{-1}$ $cm^{-2}$ | 93.30% | [438] |
| 21 | $Ni_1Cu$ | / | 326.7 μmol $h^{-1} cm^{-2}$ | 99.00% | [489] |
| 22 | Cu-NBs-100 | −.15 $V_{RHE}$ | 650 $mmol h^{-1} g_{cat}^{-1}$ | 95.30% | [490] |
| 23 | Fe/Cu-HNG | / | 1.08 mmol $h^{-1}$ $mg^{-1}$ | 92.51% | [148] |
| 24 | Co-P/TP | / | 0.42 mg $h^{-1}$ $cm^{-2}$ | 93.60% | [437] |
| 25 | Pd–$MnO_2$-$O_v$/Ni foam | −0.85 $V_{Ag/AgCl}$ | 641 $mg N m^{-2} h^{-1}$ | 87.64% | [491] |
| 26 | $v_{Co}$-$Co_3O_4$/CC | / | 6.5501 mg $h^{-1}$ $cm^{-2}$ | 97.20% | [355] |
| 27 | Fe@C-900 | / | 12 082 μg $h^{-1}$ $cm^{-2}$ | 99.00% | [492] |
| 28 | Cu@$Cu_{2+1}O$ NWs | −1.2 $V_{SCE}$ | 576.53 $\mu g h^{-1}$ | 87.07% | [314] |
| 29 | α-$Fe_2O_3$-Ni-CB | / | 5160 μg $h^{-1}$ $cm^{-2}$ | 94.60% | [493] |
| 30 | $Co_3O_4$/Co | / | 4.43 mg $h^{-1}$ $cm^{-2}$ | 88.70% | [436] |
| 31 | CoP PANSs | −0.5 $V_{RHE}$ | 19.28 $mg h^{-1} mg_{cat}^{-1}$ | 94.24% | [494] |
| 32 | $Ru_{15}Co_{85}$ | 0.4 $V_{RHE}$ | 4.28 mmol $h^{-1}$ $cm^{-2}$ | 97.00% | [441] |
| 33 | $Co_2NiO_4$ | / | 13.24 mg $h^{-1}$ $cm^{-2}$ | 94.00% | [430] |
| 34 | dr-Cu NPs | −1.3 $V_{SCE}$ | 781.25 $\mu g h^{-1} mg^{-1}$ | 85.47% | [495] |
| 35 | Cu-$Co_3O_4$/NF | / | 1.29 mg $h^{-1}$ $cm^{-2}$ | 92.40% | [496] |
| 36 | Nano Ni | / | 15.49 mmol $h^{-1}$ $cm^{-2}$ | 93.00% | [497] |
| 37 | Pd-$Co_3O_4$/TM | / | 12.67 mg $h^{-1}$ $cm^{-2}$ | 95.00% | [434] |
| 38 | Pd nanocrystalline | −0.7 $V_{RHE}$ | 0.5485 $mmol h^{-1} cm^{-2}$ | 79.91% | [498] |
| 39 | $CoO_x$ nanosheets | −0.3 $V_{RHE}$ | 82.4 $mg h^{-1} mg_{cat}^{-1}$ | 93.40% | [499] |
| 40 | Ti | / | 1.85 mg $h^{-1}$ $cm^{-2}$ | 82.00% | [106] |
| 41 | $(Cu_{0.6}Co_{0.4})Co_2O_4$ | / | 18.53 mg $h^{-1}$ $cm^{-2}$ | 96.50% | [429] |
| 42 | Charcoal electrode | −3.6 $V_{Hg/Hg2SO4}$ | 0.325 $mmol L^{-1} h^{-1} cm^{-2}$ | 96.00% | [260] |
| 43 | Cu nanosheets | −0.15 $V_{RHE}$ | 390.1 $\mu g mg^{-1}{}_{Cu} h^{-1}$ | 99.70% | [500] |
| 44 | Nano-Ag | / | 16.38 mg $h^{-1}$ $cm^{-2}$ | 89.60% | [481] |
| 45 | CoW/CF | / | 164.3 mg $h^{-1}$ $cm^{-2}$ | 98.10% | [435] |
| 46 | Ir NTs | 0.06 $V_{RHE}$ | 921 $\mu g h^{-1} mg_{cat}^{-1}$ | 84.70% | [501] |
| 47 | Cu-PTCDA | −0.4 $V_{RHE}$ | 436 ± 85 $\mu g h^{-1} cm^{-2}$ | 85.90% | [266] |
| 48 | Oxide-derived Co | / | 47.65 mg $h^{-1}$ $cm^{-2}$ | 92.40% | [502] |
| 49 | Co+Bi@Cu NW | / | 1.86 mg $h^{-1}$ $cm^{-2}$ | 99.50% | [439] |
| 50 | $TiO_2$ nanotube | −1.6 $V_{SCE}$ | 0.045 $mmol h^{-1} mg^{-1}$ | 85.00% | [89] |
| 51 | Cu/Cu–$Mn_3O_4$ NSAs/CF | −1.3 $V_{SCE}$ | 0.21 $mmol h^{-1} cm^{-2}$ | 92.40% | [503] |
| 52 | DM-Co | / | 1.2 mmol $h^{-1}$ $cm^{-2}$ | 100% | [346] |
| 53 | $Cu_{50}Co_{50}$ | / | 82.11 mg $h^{-1}$ $cm^{-2}$ | 100% | [170] |
| 54 | In–S–G | −0.5 $V_{RHE}$ | 220 $mmol h^{-1} g_{cat}^{-1}$ | 75.00% | [504] |
| 55 | Fe-$MoS_2$ | −0.48 $V_{RHE}$ | 510 $\mu g h^{-1} cm^{-2}$ | 98.00% | [193] |
| 56 | Pd/NF | / | 1.52 mmol $h^{-1}$ $cm^{-2}$ | 78.00% | [222] |
| 57 | CuCo NW | / | 71.4 mg $h^{-1}$ $cm^{-2}$ | 90.10% | [149] |
| 58 | Ir NTs | 0.06 $V_{RHE}$ | 921 $\mu g h^{-1} mg_{cat}^{-1}$ | 84.70% | [481] |
| 59 | $Fe_3O_4$/SS | −0.5 $V_{RHE}$ | 10145 $\mu g h^{-1} cm^{-2}$ | 91.50% | [479] |
| 60 | Co NA | / | 10.4 mmol $h^{-1}$ $cm^{-2}$ | 98.00% | [432] |
| 61 | Co-NAs | / | 176.8 mg $h^{-1}$ $cm^{-2}$ | 98.00% | [432] |
| 62 | BCN-Cu | −0.6 $V_{RHE}$ | 3358.74 $\mu g h^{-1} cm^{-2}$ | 98.23% | [505] |
| 63 | CoP NRs | −0.5 $V_{RHE}$ | 30.1 $mg h^{-1} mg_{cat}^{-1}$ | 97.10% | [506] |
| 64 | V-Cu NAE | / | 14.3 mg $h^{-1}$ $cm^{-2}$ | 93.70% | [292] |
| 65 | FOSP-Cu-X | / | 101.4 μmol $h^{-1}$ $cm^{-2}$ | 93.90% | [507] |
| 66 | CoP PANSs | −0.5 $V_{RHE}$ | 19.28 $mg h^{-1} mg_{cat}^{-1}$ | 94.24% | [494] |
| 67 | Fe-$MoS_2$ | −0.48 $V_{RHE}$ | 510 $\mu g h^{-1} cm^{-2}$ | 98.00% | [193] |
| 68 | cd-Pd/$Cu_2O$ NPs | / | 9.52 mg $h^{-1}$ $cm^{-2}$ | 95.80% | [508] |
| 69 | Cu/$Cu_2O$ NWAs | / | 4.08 mg $h^{-1}$ $cm^{-2}$ | 95.80% | [81] |
| 70 | Fluorine-doped carbon | −0.7 $V_{RHE}$ | 23.8 $mmol h^{-1} g_{cat}^{-1}$ | 20.00% | [509] |
| 71 | Ru/POC | / | 0.66 mmol $h^{-1}$ $cm^{-2}$ | 98.00% | [510] |
| 72 | $Ru_1Cu_{10}$/rGO | / | 6.46 mg $h^{-1}$ $cm^{-2}$ | 98.00% | [210] |
| 73 | CuNi NPs/CF | / | 94.57 mg $h^{-1}$ $cm^{-2}$ | 97.00% | [511] |
| 74 | $Fe_3C$/NC | −0.5 $V_{RHE}$ | 0.476 $mmol h^{-1} cm^{-2}$ | 96.70% | [512] |

(*continued on next page*)

**Table 2** (*continued*)

| No | Name of Catalyst | Over potential | $NH_3$ Yield rate | FE (%) | Ref |
|---|---|---|---|---|---|
| 75 | FOSP-Cu-0.1 | / | 1.72 mg $h^{-1}$ $cm^{-2}$ | 93.90% | [507] |
| 76 | Cu-NB-100 | / | 6.5 mmol $h^{-1}$ $cm^{-2}$ | 95.00% | [513] |
| 77 | Rh@Cu-0.6% | / | 21.59 mg $h^{-1}$ $cm^{-2}$ | 93.00% | [104] |
| 78 | OD-Cu | −0.20 $V_{RHE}$ | 1.1 mmol $h^{-1}$ $cm^{-2}$ | 92.00% | [59] |
| 79 | Rh NFs | / | 0.25 mg $h^{-1}$ $cm^{-2}$ | 95.00% | [244] |
| 80 | Ru-ST-12 | / | 1.17 mmol $h^{-1}$ $cm^{-2}$ | 100% | [155] |
| 81 | O-$PdFe_3$.mCNFs | / | 17.17 mg $h^{-1}$ $cm^{-2}$ | 96.50% | [231] |
| 82 | Co–P/TP | −0.6 $V_{RHE}$ | 416.0 ± 7.2 μg $h^{-1}$ $cm^{-2}$ | 93.60% | [437] |
| 83 | $a_1$-Ru-CNTs | −0.2 $V_{RHE}$ | 362.75 μg $h^{-1}$ $cm^{-2}$ | 80.60% | [213] |

motifs, alloy compositions, and surface modifications. These efforts are expected to accelerate the development of highly selective, efficient, and durable electrocatalysts, ultimately enabling sustainable and scalable $NH_3$ production from nitrate-contaminated sources while resolving critical mechanistic challenges in the field.

***Catalyst Innovation Beyond Incremental Modifications*:** Although considerable progress has been made in the development of carbon-based hybrids, transition-metal alloys, and noble-metal nanostructures, achieving consistently high FEs in the e-$NO_3$RR remains limited by challenges such as long-term stability, scalability to industrially relevant current densities, and sustained catalytic durability. Conventional strategies based on incremental modifications, including minor doping or superficial functionalization, have largely reached a performance plateau, underscoring the need for transformative approaches that fundamentally reimagine catalyst architectures. Recent advancements indicate that defect engineering, strain modulation, multi-component frameworks, heterostructure integration, and high-entropy alloy designs can synergistically optimize electronic structures, adsorption energetics, and the local reaction environment of active sites, thereby enhancing selectivity, accelerating reaction kinetics, and suppressing competing side reactions. Simultaneously, tailoring hierarchical porosity, surface morphology, and interfacial properties improves reactant accessibility, facilitates efficient mass transport, and stabilizes active sites under prolonged operation. Looking ahead, rational catalyst design guided by computational modeling, data-driven simulations, and artificial intelligence offers unprecedented opportunities to predict optimal active site configurations, alloy compositions, and surface modifications, accelerating the discovery of high-performance electrocatalysts. Integrating these approaches with scalable, energy-efficient, and application-oriented deployment strategies provides a clear roadmap for next-generation nitrate-to-$NH_3$ electrolysis platforms that simultaneously address efficiency, selectivity, durability, and practical feasibility. By transcending incremental improvements, the field is positioned to realize catalysts capable of robust, sustainable, and industrially relevant $NH_3$ production from nitrate-contaminated sources while overcoming fundamental performance limitations.

***System and Process Engineering*:** The predominance of H-type electrochemical cells in laboratory-scale studies has created a significant translational gap between academic findings and industrial implementation of the e-$NO_3$RR. While these cells provide a controlled environment to investigate fundamental mechanisms and material performance, they fail to replicate the mass transport limitations, electrolyte dynamics, and continuous operation conditions characteristic of industrial-scale systems. To bridge this gap, the development and deployment of flow-electrolyzers, membrane-electrode assemblies, and modular reactor architectures are paramount, as they enable enhanced reactant delivery, improved mass transport, and sustained catalyst utilization under continuous operation. Tailored reactor design, including optimization of electrode geometry, flow patterns, and electrolyte distribution, is essential to ensure uniform reaction kinetics and minimize concentration gradients that can limit $NH_3$ yield and selectivity.

Beyond reactor design, integrating hybrid or photo-assisted electrochemical systems offers a promising strategy to reduce the energy barrier of nitrate reduction, facilitating near-ambient operation and improving overall process energy efficiency. Coupling advanced catalyst architectures with continuous-flow systems allows for the precise control of reaction environments, promoting efficient desorption of intermediates, suppression of side reactions, and prolonged catalyst stability. Additionally, the selective capture and pre-concentration of nitrate from real wastewater streams can mitigate the detrimental effects of competing ions and organic matter, enhancing $NH_3$ production efficiency and system resilience under practical conditions.

Future process engineering must also consider scalable deployment, energy sustainability, and economic feasibility. Reactor designs should be compatible with high-capacity electrocatalysts while maintaining low energy consumption and minimal operational complexity. Integration with downstream $NH_3$ recovery technologies, such as selective adsorption or membrane-assisted separation, ensures high-purity product generation while minimizing losses and environmental impact. Furthermore, dynamic operational strategies, including potential pulsing, flow modulation, or hybrid electrochemical-photocatalytic operation, can further optimize catalyst performance, reduce deactivation, and enhance process throughput. By coupling advanced catalyst development with carefully engineered system architectures, continuous-flow nitrate-to-$NH_3$ electrolysis can transition from proof-of-concept studies to industrially viable platforms, enabling sustainable nitrogen utilization with high efficiency, selectivity, and operational reliability.

***Performance in Realistic Conditions*:** Significant advancements have been achieved in the development of electrocatalysts for $NO_3^- \rightarrow NH_3$. However, most reported studies have been conducted under idealized conditions, employing electrolytes with elevated nitrate concentrations, tightly controlled pH, and minimal interference from extraneous ions. In practical scenarios, nitrate-contaminated waters and industrial effluents present far more complex and challenging environments, characterized by low nitrate levels (typically <1.5 mM), variable pH, the presence of competing anions (e.g., $Ca^{2+}$, $Mg^{2+}$, $HCO_3^-$), organic pollutants (such as phenols, urea, and pharmaceutical residues), and natural organic matter (humic and fulvic acids). These factors profoundly impact nitrate adsorption, activation, and reduction kinetics at the catalyst interface, often resulting in decreased activity, lower $NH_3$ selectivity, and the formation of undesirable byproducts. To address these challenges, the design of robust, selective, and resilient electrocatalysts is imperative. Tailored strategies including hierarchical porous architectures, nanostructured surfaces, and engineered active sites can enhance reactant accessibility, facilitate rapid electron transfer, and mitigate active site blockage by adsorbed intermediates. Surface functionalization, protective coatings and dynamic operational protocols, such as pulsed potential or periodic electrode regeneration, further improve catalyst longevity by promoting desorption of intermediates and minimizing surface poisoning. Additionally, pre-concentration and selective capture of nitrate via adsorption or ion-exchange techniques can locally enhance reactant availability, suppress interference from competing species, and improve overall reaction kinetics in low-concentration media.

Beyond material considerations, effective deployment of e-$NO_3$RR in real-world systems necessitates integrated reactor and process engineering. Continuous-flow electrodes, microfluidic platforms, and membrane-assisted architectures enable enhanced mass transport,

uniform reactant distribution, and stable local pH environments. Coupling these systems with downstream $NH_3$ recovery strategies such as membrane-based separation or selective adsorption ensures high recovery efficiency, minimal product loss, and production of high-purity $NH_3$ suitable for industrial application. Furthermore, integration with renewable energy sources or hybrid photo-assisted electrochemical approaches can reduce energy consumption and facilitate operation under near-ambient conditions, enhancing overall sustainability.

Bridging the gap between laboratory-scale performance and industrial relevance requires a comprehensive, multi-dimensional approach. This includes the development of durable, highly selective catalysts, optimization of reactor configurations to overcome mass transport limitations, and careful consideration of complex water chemistries with coexisting ions and organic constituents. Pilot-scale validation using real wastewater streams is critical to assess long-term catalyst performance, identify potential fouling or deactivation mechanisms, and evaluate the economic and energetic feasibility of scalable e-$NO_3$RR systems. Only through such an integrated framework can e-$NO_3$RR transition from controlled laboratory studies to robust, large-scale applications, enabling sustainable and practical nitrogen recovery.

***Value-Chain Integration and Emerging Applications*:** Integrating e-$NO_3$RR into broader chemical and industrial value chains offers a transformative pathway for sustainable $NH_3$ and chemical production. Coupling nitrate reduction with complementary processes, such as $CO_2$ reduction or nitrogen fixation, enables the simultaneous generation of high-value nitrogenous and carbon-based products including urea, hydroxylamine, and ammonium carbamate, key intermediates for fertilizers, pharmaceuticals, and fine chemicals. This approach maximizes economic value while promoting resource efficiency. Effective integration requires electrocatalysts that combine high $NH_3$ selectivity with compatibility for sequential or concurrent reaction pathways, maintaining FE in complex, multi-component systems. Hierarchical and hybrid catalyst architectures, alongside defect-engineered surfaces, provide tunable electronic structures, abundant active sites, and enhanced mass transport, facilitating efficient reaction kinetics and improved selectivity. Embedding e-$NO_3$RR into closed-loop nitrogen management systems advances circular economy principles. Nitrate-rich wastewater or agricultural runoff can be converted into $NH_3$ for fertilizer production, transforming pollutant remediation into resource valorization, minimizing environmental nitrogen losses, and mitigating eutrophication.

Practical implementation demands system-level optimization, including selective nitrate capture from dilute sources, energy-efficient reactor design, and downstream $NH_3$ recovery via membrane separation, ion-selective adsorption, or electrochemical stripping. Coordinated operation of these processes ensures robust performance in complex matrices containing competing ions, organics, and fluctuating pH. These strategies position e-$NO_3$RR not only as a sustainable $NH_3$ production technology but also as a cornerstone of next-generation chemical and environmental engineering solutions.

***Scalability and Industrial Feasibility*:** The industrial implementation of e-$NO_3$RR hinges on scalable catalyst production, electrode durability, and cost-effectiveness, which collectively dictate the economic viability and environmental footprint of large-scale $NH_3$ synthesis. For practical deployment, catalysts and electrodes must combine high performance with long-term stability, resisting deactivation under corrosive environments and dynamic operating conditions. Surface engineering, protective coatings, and corrosion-resistant materials can prolong operational lifetimes, while strategies such as potential modulation or pulsed operation can regenerate active sites and mitigate byproduct accumulation.

Industrial-scale reactors require optimized architectures for uniform mass transport, efficient electrolyte flow, and effective nitrate delivery to catalytic sites. Coupling these reactors with energy-efficient $NH_3$ recovery technologies including membrane separation, ion-selective adsorption, or electrochemical stripping ensures high product purity and minimal losses. Utilizing renewable electricity further reduces the carbon footprint, advancing sustainable chemical manufacturing goals.

Despite these advancements, challenges remain in scaling nanostructured catalysts, maintaining long-term stability in complex wastewater matrices, and assessing economic feasibility. Pilot-scale demonstrations, supported by in-situ characterization and performance monitoring, are essential to translate laboratory successes into commercially viable e-$NO_3$RR systems. Addressing these factors will enable sustainable $NH_3$ production from nitrate-rich resources while advancing circular nitrogen management.

## 9. Outlook

The development of e-$NO_3$RR is entering a critical phase where the integration of fundamental mechanistic understanding with practical engineering solutions will define its future trajectory. Recent progress in catalyst design including atomic-level tailoring, defect modulation, and hybrid material architectures has revealed new pathways to enhance reaction kinetics and selectivity, yet translating these findings into stable, scalable, and economically viable systems remains a significant challenge. Optimizing the accessibility of active sites, improving charge and mass transport, and suppressing parasitic reactions are central to achieving high FE under realistic operational conditions. Equally important is the adaptation of these catalysts to complex nitrate-containing streams, where coexisting ions, organic molecules, and natural contaminants can interfere with reaction pathways and impede performance. Future research should focus on strategies that not only enhance catalyst robustness but also selectively capture and deliver nitrate to reactive sites, ensuring consistent activity and $NH_3$ yield across variable water matrices. Coupling these approaches with efficient $NH_3$ separation and recovery methods will be critical for realizing integrated, sustainable systems capable of minimizing product losses and maintaining high purity.

Advancing e-$NO_3$RR also demands a deeper understanding of dynamic reaction mechanisms under operational conditions. Real-time, high-resolution characterization techniques, combined with data-driven modeling, can provide insights into intermediate formation, active site utilization, and degradation processes, guiding the rational design of more resilient and selective catalysts. Furthermore, evaluating the scalability, energy efficiency, and environmental footprint of these systems will be essential for bridging laboratory demonstrations with practical implementation, enabling the technology to move beyond proof-of-concept studies toward industrial relevance. Ultimately, the promise of e-$NO_3$RR lies not only in efficient $NH_3$ production but also in contributing to a circular nitrogen economy. By converting nitrate pollutants into valuable chemical feedstocks, this technology exemplifies a sustainable approach to resource recovery, offering both environmental and societal benefits. Realizing this vision will require coordinated advances in materials science, electrochemical engineering, and system-level integration, positioning e-$NO_3$RR as a transformative platform for green $NH_3$ synthesis and nitrogen management.

## Declaration of competing interest

The authors affirm that no financial or personal relationships exist that could have inappropriately influenced the research and findings presented in this work.

## Acknowledgements

The author gratefully acknowledges Prof. Bo Weng for valuable guidance and constructive suggestions during the preparation of this work. All authors have significant contribution in the reported work. The authors appreciate the Fundamental Research Funds for the Central Universities (No. 2232024D-31), the National Natural Science Foundation of China (grant 22005046).

## Data availability

No data was used for the research described in the article.

## References


[1] C. Wang, Y. Luo, J. Liu, R. Zhu, P. Zhao, L. Fu, J. Vela, H.-J.S. Fan, Inorg. Chem. 64 (32) (2025) 16277–16288.
[2] R. Jia, X. Zhang, L. Gan, M. Tahir, Z.-F. Huang, L. Pan, R. Gao, C. Shi, X. Zhang, G. Yang, J.-J. Zou, J. Mater. Chem. A 13 (2025) 5732–5743.
[3] M. Humayun, Z. Li, M. Israr, A. Khan, W. Luo, C. Wang, Z. Shao, Chem. Rev. 125 (2025) 3165–3241.
[4] T. Hou, T. Shan, H. Rong, J. Zhang, ChemSusChem 18 (2025) e202402331.
[5] I.M.U. Hasan, N. Xu, Y. Liu, M.Z. Nawaz, H. Feng, J. Qiao, Electrochem. Energy Rev. 7 (2024) 36.
[6] H. Zhang, H. Wang, X. Cao, M. Chen, Y. Liu, Y. Zhou, M. Huang, L. Xia, Y. Wang, T. Li, D. Zheng, Y. Luo, S. Sun, X. Zhao, X. Sun, Adv. Mater. 36 (2024) 2312746.
[7] J. Liang, Z. Li, L. Zhang, X. He, Y. Luo, D. Zheng, Y. Wang, T. Li, H. Yan, B. Ying, S. Sun, Q. Liu, M.S. Hamdy, B. Tang, X. Sun, Chem 9 (2023) 1768–1827.
[8] L. Ouyang, J. Liang, Y. Luo, D. Zheng, S. Sun, Q. Liu, M.S. Hamdy, X. Sun, B. Ying, Chin. J. Catal. 50 (2023) 6–44.
[9] Y. Pan, H.-M. Xu, H.-R. Zhu, C.-J. Huang, Z.-J. Zhang, G.-R. Li, J. Mater. Chem. A 13 (2025) 21181–21232.
[10] S.M. Gowdru, P.H. Nagaraju, Y.-C. Chen, K.-C. Wu, C.-C. Chang, D.-Y. Wang, Chem. Commun. 61 (2025) 6965–6968.
[11] G. Ding, Z. Wang, Q. Jiang, ChemCatChem 17 (2025) e202402050.
[12] J. Ni, Z. Shi, Y. Wang, J. Yang, H. Wu, P. Wang, M. Xiao, C. Liu, W. Xing, eScience 5 (2025) 100295.
[13] J. Chen, A. Wu, Y. Xie, Y. Zhang, H. Zheng, W. Teng, Electrochem. Commun. 177 (2025) 107964.
[14] B. Bai, Y. Wan, W. Yan, J. Zhang, 2D Materials 12 (2025) 022006.
[15] X. Meng, X. Tan, Y. Ma, A.A. Obisanya, J. Wang, Z. Xiao, D. Wang, Adv. Funct. Mater. 35 (2025) 2418492.
[16] J. Zhou, S. Gao, G. Hu, Energy Fuel 38 (2024) 6701–6722.
[17] K. Zhang, Y. Liu, Z. Pan, Q. Xia, X. Huo, O.C. Esan, X. Zhang, L. An, EES Catal. 2 (2024) 727–752.
[18] J. Li, S. Chen, F. Quan, G. Zhan, F. Jia, Z. Ai, L. Zhang, Chem 6 (2020) 885–901.
[19] C. Lin, W. Li, H. Chen, J. Feng, M. Zhu, J. Shi, M. Li, B. Hou, Z. Wang, X. Chen, J. Liu, W. Yan, Adv. Sci. 12 (2025) 2502262.
[20] C. Zhang, Y. Zhang, R. Deng, L. Yuan, Y. Zou, T. Bao, X. Zhang, G. Wei, C. Yu, C. Liu, Adv. Mater. 36 (2024) 2313844.
[21] K. Yang, S.-H. Han, C. Cheng, C. Guo, T. Li, Y. Yu, J. Am. Chem. Soc. 146 (2024) 12976–12983.
[22] N. Han, W. Zhang, J. Wu, K. Chu, S. Feng, S. Wang, A.R. Puente-Santiago, J. Long, B. Weng, B.-L. Su, Angew. Chem. Int. Ed. 64 (2025) e202504601.
[23] X. Zhao, F. Yin, N. Liu, G. Li, T. Fan, B. Chen, J. Mater. Sci. 52 (2017) 10175–10185.
[24] W. Liao, J. Wang, Y. Tan, X. Zi, C. Liu, Q. Wang, L. Zhu, C.-W. Kao, T.-S. Chan, H. Li, Y. Zhang, K. Liu, C. Cai, J. Fu, B. Xi, E. Cortés, L. Chai, M. Liu, Nat. Commun. 16 (2025) 5715.
[25] D. Li, S. Zhang, Z. Mao, M. Liu, K. Hu, D. Zhao, Z. Qv, L. Zhou, T. Shi, RSC Adv. 15 (2025) 9461–9466.
[26] Q. Lai, Z. Liu, A. Akasa, X. Zhao, R. Wei, X.-W. Gao, T.M. Al Wafi, Q. Gu, W.-B. Luo, Chem. Eng. J. 520 (2025) 166332.
[27] N. Han, W. Guo, L. Fan, Y. Yan, B. Weng, J.E. Huang, J. Wu, P.-Y. Tang, Y. Bai, Y.-M. Zheng, S. Wang, X. Zhang, B.-L. Su, Adv. Mater. 37 (2025) e00900.
[28] J. Wei, Y. Li, H. Lin, X. Lu, C. Zhou, Y.-y. Li, Environmental Science and Ecotechnology, 20 (2024) 100383.
[29] K. Chu, B. Weng, Z. Lu, Y. Ding, W. Zhang, R. Tan, Y.-M. Zheng, N. Han, Adv. Sci. 12 (2025) 2416053.
[30] C. Smith, A.K. Hill, L. Torrente-Murciano, Energy Environ. Sci. 13 (2020) 331–344.
[31] K. Harun, S. Adhikari, H. Jahromi, RSC Adv. 10 (2020) 40882–40893.
[32] D.R. MacFarlane, P.V. Cherepanov, J. Choi, B.H.R. Suryanto, R.Y. Hodgetts, J. M. Bakker, F.M. Ferrero Vallana, A.N. Simonov, Joule 4 (2020) 1186–1205.
[33] Q. Xu, L. Zhang, J. Zhang, J. Wang, Y. Hu, H. Jiang, C. Li, EnergyChem 4 (2022) 100087.
[34] Y. Xu, S. Cai, B. Chi, Z. Tu, Int. J. Hydrog. Energy 50 (2024) 548–591.
[35] S. Shiva Kumar, V. Himabindu, Materials Science for Energy Technologies 2 (2019) 442–454.
[36] I. Vincent, D. Bessarabov, Renew. Sust. Energ. Rev. 81 (2018) 1690–1704.
[37] A.M. Couper, D. Pletcher, F.C. Walsh, Chem. Rev. 90 (1990) 837–865.
[38] A. Wiebe, T. Gieshoff, S. Möhle, E. Rodrigo, M. Zirbes, S.R. Waldvogel, Angew. Chem. Int. Ed. 57 (2018) 5594–5619.
[39] J. Wang, Electrochim. Acta 26 (1981) 1721–1726.
[40] R. Ramachandran, T.-W. Chen, S.-M. Chen, G.P. Gnana Kumar, M. Chinnasamy, N. Biruntha Devi, T.-W. Tseng, Int. J. Electrochem. Sci. 12 (2017) 1572–1588.
[41] D.M. Heard, A.J.J. Lennox, Angew. Chem. Int. Ed. 59 (2020) 18866–18884.
[42] C. Costentin, J.-M. Savéant, 116 Proceedings of the National Academy of Sciences USA, 2019, pp. 11147–11152.
[43] M.M. Baizer, J.H. Stocker, J. Electrochem. Soc. 121 (1974) 134C.
[44] G.V. Govindaraju, G.P. Wheeler, D. Lee, K.-S. Choi, Chem. Mater. 29 (2017) 355–370.
[45] Y.A. Lyon, A.A. Roberts, D.R. McMillin, J. Chem. Educ. 92 (2015) 2130–2133.
[46] Y. Yu, P. Guo, J.-S. Zhong, Y. Yuan, K.-Y. Ye, Organic Chemistry Frontiers 7 (2020) 131–135.
[47] A. Fattah-alhosseini, M. Karbasi, A. Fardosi, M. Kaseem, Ceram. Int. 50 (2024) 25822–25831.
[48] H. Zhao, W. Xu, M. Li, Z. Meng, I. Ullah, M.Z. Nawaz, J. Wang, C. Wang, P.K. Chu, J. Power Sources 626 (2025) 235793.
[49] S. Verma, X. Lu, S. Ma, R.I. Masel, P.J.A. Kenis, Phys. Chem. Chem. Phys. 18 (2016) 7075–7084.
[50] E. Coulon, J. Pinson, J.-D. Bourzat, A. Commerçon, J.P. Pulicani, Langmuir 17 (2001) 7102–7106.
[51] D. Bélanger, J. Pinson, Chem. Soc. Rev. 40 (2011) 3995–4048.
[52] B.K. Peters, K.X. Rodriguez, S.H. Reisberg, S.B. Beil, D.P. Hickey, Y. Kawamata, M. Collins, J. Starr, L. Chen, S. Udyavara, K. Klunder, T.J. Gorey, S.L. Anderson, M. Neurock, S.D. Minteer, P.S. Baran, Science 363 (2019) 838–845.
[53] H. Tateno, K. Nakabayashi, T. Kashiwagi, H. Senboku, M. Atobe, Electrochim. Acta 161 (2015) 212–218.
[54] A.J.J. Lennox, J.E. Nutting, S.S. Stahl, Chem. Sci. 9 (2018) 356–361.
[55] K. Chen, D. Xue, J. Mater. 1 (2015) 170–187.
[56] R.D. Little, K.D. Moeller, Chem. Rev. 118 (2018) 4483–4484.
[57] J.K. Nørskov, T. Bligaard, J. Rossmeisl, C.H. Christensen, Nat. Chem. 1 (2009) 37–46.
[58] H. Wang, L. Wang, Q. Wang, S. Ye, W. Sun, Y. Shao, Z. Jiang, Q. Qiao, Y. Zhu, P. Song, D. Li, L. He, X. Zhang, J. Yuan, T. Wu, G.A. Ozin, Angew. Chem. Int. Ed. 57 (2018) 12360–12364.
[59] J. Yuan, Z. Xing, Y. Tang, C. Liu, ACS Appl. Mater. Interfaces 13 (2021) 52469–52478.
[60] T.A. Ivandini, T. Watanabe, T. Matsui, Y. Ootani, S. Iizuka, R. Toyoshima, H. Kodama, H. Kondoh, Y. Tateyama, Y. Einaga, J. Phys. Chem. C 123 (2019) 5336–5344.
[61] J. Xu, Y. Yokota, R.A. Wong, Y. Kim, Y. Einaga, J. Am. Chem. Soc. 142 (2020) 2310–2316.
[62] P. Sabatier, La catalyse en chimie organique, C. Béranger (1920). https://books.google.co.jp/books/about/La_catalyse_en_chimie_organique.html?id=pIcMAQAAIAAJ&redir_esc=y.
[63] N. Dubouis, A. Grimaud, Chem. Sci. 10 (2019) 9165–9181.
[64] Y. Liu, X. Li, Q. Zhang, W. Li, Y. Xie, H. Liu, L. Shang, Z. Liu, Z. Chen, L. Gu, Z. Tang, T. Zhang, S. Lu, Angew. Chem. Int. Ed. 59 (2020) 1718–1726.
[65] Y. Wang, C. Wang, M. Li, Y. Yu, B. Zhang, Chem. Soc. Rev. 50 (2021) 6720–6733.
[66] C.J.M. van der Ham, M.T.M. Koper, D.G.H. Hetterscheid, Chem. Soc. Rev. 43 (2014) 5183–5191.
[67] Z. Wang, D. Richards, N. Singh, Catalysis Science & Technology 11 (2021) 705–725.
[68] L. Mi, Q. Huo, J. Cao, X. Chen, H. Yang, Q. Hu, C. He, Adv. Energy Mater. 12 (2022) 2202247.
[69] L. Grimaud, S. Lakhdar, M.R. Vitale, Current Opinion in Electrochemistry 40 (2023) 101307.
[70] X. Zhang, L. Han, H. Chen, S. Wang, Chin. Chem. Lett. 33 (2022) 1117–1130.
[71] A. Bagger, Current Opinion in Electrochemistry 40 (2023) 101339.
[72] I. Katsounaros, Current Opinion in Electrochemistry 28 (2021) 100721.
[73] I. Katsounaros, M.C. Figueiredo, F. Calle-Vallejo, H. Li, A.A. Gewirth, N. M. Markovic, M.T.M. Koper, J. Catal. 359 (2018) 82–91.
[74] G.E. Dima, A.C.A. de Vooys, M.T.M. Koper, J. Electroanal. Chem. 554-555 (2003) 15–23.
[75] M. Duca, M.C. Figueiredo, V. Climent, P. Rodriguez, J.M. Feliu, M.T.M. Koper, J. Am. Chem. Soc. 133 (2011) 10928–10939.
[76] M. Teng, J. Ye, C. Wan, G. He, H. Chen, Ind. Eng. Chem. Res. 61 (2022) 14731–14746.
[77] X. Zhang, Y. Wang, C. Liu, Y. Yu, S. Lu, B. Zhang, Chem. Eng. J. 403 (2021) 126269.
[78] T. Chen, H. Li, H. Ma, M.T.M. Koper, Langmuir 31 (2015) 3277–3281.
[79] E. Pérez-Gallent, M.C. Figueiredo, I. Katsounaros, M.T.M. Koper, Electrochim. Acta 227 (2017) 77–84.
[80] J.-X. Liu, D. Richards, N. Singh, B.R. Goldsmith, ACS Catal. 9 (2019) 7052–7064.
[81] Y. Wang, W. Zhou, R. Jia, Y. Yu, B. Zhang, Angew. Chem. Int. Ed. 59 (2020) 5350–5354.
[82] M. Karamad, T.J. Goncalves, S. Jimenez-Villegas, I.D. Gates, S. Siahrostami, Faraday Discuss. 243 (2023) 502–519.
[83] M.T. de Groot, M.T.M. Koper, J. Electroanal. Chem. 562 (2004) 81–94.
[84] H. Niu, Z. Zhang, X. Wang, X. Wan, C. Shao, Y. Guo, Adv. Funct. Mater. 31 (2021) 2008533.
[85] M. Duca, M.T.M. Koper, Energy Environ. Sci. 5 (2012) 9726–9742.
[86] Z. Wu, Y. Song, Y. Liu, W. Luo, W. Li, J. Yang, Chem Catalysis 3 (2023).
[87] X. Lv, T. Mou, J. Li, L. Kou, T. Frauenheim, Adv. Funct. Mater. 32 (2022) 2201262.
[88] D. Liu, L. Qiao, S. Peng, H. Bai, C. Liu, W.F. Ip, K.H. Lo, H. Liu, K.W. Ng, S. Wang, X. Yang, H. Pan, Adv. Funct. Mater. 33 (2023) 2303480.
[89] R. Jia, Y. Wang, C. Wang, Y. Ling, Y. Yu, B. Zhang, ACS Catal. 10 (2020) 3533–3540.
[90] V. Rosca, G.L. Beltramo, M.T.M. Koper, J. Electroanal. Chem. 566 (2004) 53–62.
[91] W. Chen, A. Yu, Z.-J. Sun, B.-Q. Zhu, J. Cai, Y.-X. Chen, Current Opinion in Electrochemistry 14 (2019) 113–123.
[92] L. Sivachandiran, F. Thevenet, A. Rousseau, D. Bianchi, Appl. Catal. B Environ. 198 (2016) 411–419.
[93] W. Ding, K. Yan, Y. Li, C. Hu, H. Yi, C. Liu, C. Wang, C. Zhou, D. Ma, J. Environ. Chem. Eng. 12 (2024) 114694.
[94] V.I. Kravtsov, V.V. Malev, Russ. J. Electrochem. 43 (2007) 981–982.

[95] A. Manzo-Robledo, C. Lévy-Clément, N. Alonso-Vante, Electrochim. Acta 117 (2014) 420–425.
[96] I. Katsounaros, G. Kyriacou, Electrochim. Acta 52 (2007) 6412–6420.
[97] M. Fedurco, P. Kedzierzawski, J. Augustynski, J. Electrochem. Soc. 146 (1999) 2569.
[98] T.Y. Safonova, O.A. Petrii, J. Electroanal. Chem. 448 (1998) 211–216.
[99] J. Guo, M.J. Liu, C. Laguna, D.M. Miller, K.S. Williams, B.D. Clark, C. Muñoz, S. J. Blair, A.C. Nielander, T.F. Jaramillo, W.A. Tarpeh, Energy Environ. Sci. 17 (2024) 8787–8800.
[100] Z. Wu, Y. Song, Y. Liu, W. Luo, W. Li, J. Yang, Chem Catalysis 3 (2023) 100786.
[101] J. Yang, P. Sebastian, M. Duca, T. Hoogenboom, M.T.M. Koper, Chem. Commun. 50 (2014) 2148–2151.
[102] Q. Li, G.-h. Liu, L. Qi, H. Wang, G. Xian, Sci. Total Environ., 896 (2023) 165169.
[103] L. Su, K. Li, H. Zhang, M. Fan, D. Ying, T. Sun, Y. Wang, J. Jia, Water Res. 120 (2017) 1–11.
[104] H. Liu, X. Lang, C. Zhu, J. Timoshenko, M. Rüscher, L. Bai, N. Guijarro, H. Yin, Y. Peng, J. Li, Z. Liu, W. Wang, B.R. Cuenya, J. Luo, Angew. Chem. Int. Ed. 61 (2022) e202202556.
[105] Z.-Y. Wu, M. Karamad, X. Yong, Q. Huang, D.A. Cullen, P. Zhu, C. Xia, Q. Xiao, M. Shakouri, F.-Y. Chen, J.Y. Kim, Y. Xia, K. Heck, Y. Hu, M.S. Wong, Q. Li, I. Gates, S. Siahrostami, H. Wang, Nat. Commun. 12 (2021) 2870.
[106] J.M. McEnaney, S.J. Blair, A.C. Nielander, J.A. Schwalbe, D.M. Koshy, M. Cargnello, T.F. Jaramillo, ACS Sustain. Chem. Eng. 8 (2020) 2672–2681.
[107] J. Yan, H. Xu, L. Chang, A. Lin, D. Cheng, Nanoscale 14 (2022) 15422–15431.
[108] J. Chen, T. Gong, Q. Hou, J. Li, L. Zhang, D. Zhao, Y. Luo, D. Zheng, T. Li, S. Sun, Z. Cai, Q. Liu, L. Xie, M. Wu, A.A. Alshehri, X. Sun, Chem. Commun. 58 (2022) 13459–13462.
[109] H. Liu, J. Qin, J. Mu, B. Liu, J. Colloid Interface Sci. 636 (2023) 134–140.
[110] K. Wu, C. Wu, W. Bai, N. Li, Y. Gao, L. Ge, Colloids Surf. A Physicochem. Eng. Asp. 663 (2023) 131089.
[111] X. Zhang, X. Han, Y. Wei, X. Wang, N. Zhang, J. Bao, G. He, Chem. Eng. J. 428 (2022) 132660.
[112] A. Irfan, I. Ullah, M. Li, X. Peng, S. Ali, M.Z. Nawaz, P. Zhong, R. Che, Adv. Mater. 37 (2025) 2509246.
[113] S. Ye, Z. Chen, G. Zhang, W. Chen, C. Peng, X. Yang, L. Zheng, Y. Li, X. Ren, H. Cao, D. Xue, J. Qiu, Q. Zhang, J. Liu, Energy Environ. Sci. 15 (2022) 760–770.
[114] H. Zhang, G. Wang, C. Wang, Y. Liu, Y. Yang, C. Wang, W. Jiang, L. Fu, J. Xu, J. Electroanal. Chem. 910 (2022) 116171.
[115] Y. Huang, C. He, C. Cheng, S. Han, M. He, Y. Wang, N. Meng, B. Zhang, Q. Lu, Y. Yu, Nat. Commun. 14 (2023) 7368.
[116] Q. Wu, X. Fan, K. Liu, X. Quan, Y. Liu, Appl. Catal. B Environ. Energy 361 (2025) 124597.
[117] W. Liao, J. Wang, G. Ni, K. Liu, C. Liu, S. Chen, Q. Wang, Y. Chen, T. Luo, X. Wang, Y. Wang, W. Li, T.-S. Chan, C. Ma, H. Li, Y. Liang, W. Liu, J. Fu, B. Xi, M. Liu, Nat. Commun. 15 (2024) 1264.
[118] F.-Y. Chen, Z.-Y. Wu, S. Gupta, D.J. Rivera, S.V. Lambeets, S. Pecaut, J.Y.T. Kim, P. Zhu, Y.Z. Finfrock, D.M. Meira, G. King, G. Gao, W. Xu, D.A. Cullen, H. Zhou, Y. Han, D.E. Perea, C.L. Muhich, H. Wang, Nat. Nanotechnol. 17 (2022) 759–767.
[119] H.W. Kroto, J.R. Heath, S.C. O'Brien, R.F. Curl, R.E. Smalley, Nature 318 (1985) 162–163.
[120] V. Georgakilas, J.N. Tiwari, K.C. Kemp, J.A. Perman, A.B. Bourlinos, K.S. Kim, R. Zboril, Chem. Rev. 116 (2016) 5464–5519.
[121] M. Javed, Y. Sui, M.Z. Nawaz, Y. Wang, J. Yating, Z. Cai, B. Xu, ACS EST Water 2 (2022) 873–882.
[122] C.-G. Han, Y.-B. Zhu, L. Yang, J. Chen, S. Liu, H. Wang, Y. Ma, D. Han, L. Niu, Energy Environ. Sci. 17 (2024) 1559–1569.
[123] G.M. Callicó, Nat. Photonics 11 (2017) 332–333.
[124] M. Javed, S. Pirah, Y. Xiao, Y. Sun, Y. Ji, M.Z. Nawaz, Z. Cai, B. Xu, ACS Omega 6 (2021) 35104–35111.
[125] Y. Sun, M. Javed, Y. Ji, M.Z. Nawaz, Y. Wang, Z. Cai, B. Xu, Sol. Energy Mater. Sol. Cells 245 (2022) 111836.
[126] Y. Lu, Y. Lu, Z. Niu, J. Chen, Adv. Energy Mater. 8 (2018) 1702469.
[127] Y. Chen, Q. Zhou, G. Zhao, Z. Yu, X. Wang, S.X. Dou, W. Sun, Adv. Funct. Mater. 28 (2018) 1705583.
[128] H. Huang, M. Yan, C. Yang, H. He, Q. Jiang, L. Yang, Z. Lu, Z. Sun, X. Xu, Y. Bando, Y. Yamauchi, Adv. Mater. 31 (2019) 1903415.
[129] N.J. Harmon, C.L. Rooney, Z. Tao, B. Shang, N. Raychaudhuri, C. Choi, H. Li, H. Wang, ACS Catal. 12 (2022) 9135–9142.
[130] S. Mukherjee, D.A. Cullen, S. Karakalos, K. Liu, H. Zhang, S. Zhao, H. Xu, K. L. More, G. Wang, G. Wu, Nano Energy 48 (2018) 217–226.
[131] M.Z. Nawaz, L. Xu, X. Zhou, K.H. Shah, J. Wang, B. Wu, C. Wang, Materials Advances 2 (2021) 6031–6038.
[132] S. Sharma, B.G. Pollet, J. Power Sources 208 (2012) 96–119.
[133] W. Li, Z. Pan, Z. Huang, Q. Zhou, Y. Xu, S. Wu, C. Chen, Y. Lin, G. Hu, Int. J. Hydrog. Energy 43 (2018) 9777–9786.
[134] R.M. Abdel Hameed, A.E. Fetohi, R.S. Amin, K.M. El-Khatib, Appl. Surf. Sci. 359 (2015) 651–663.
[135] W. Ul Hasan, M. Li, W. Xu, Z. Meng, M.Z. Nawaz, J. Wang, C. Wang, P. Zhong, P. K. Chu, ACS Appl. Energy Mater. 7 (2024) 9267–9278.
[136] M.Z. Nawaz, L. Xu, X. Zhou, K.H. Shah, M. Yaqub, J. Wang, B. Wu, C. Wang, ACS Applied Electronic Materials 3 (2021) 4151–4161.
[137] W. Ahmad, M.U. Rehman, M.Z. Nawaz, V. Laxmi, J. Huang, Y. Wu, Z. Wang, F. Yi, Q. Liang, Y.Y. Illarionov, ACS Appl. Mater. Interfaces 17 (2025) 56308–56319.
[138] M.Z. Nawaz, W. Ahmad, U. Younis, A. Khaleeq, W. Ul Hasan, R.Z.A. Manj, M. S. Saleem, I. Ullah, A. Irfan, I.M. Ul Hasan, M. Yaqub, H.M.N.U.H.K. Asghar, G. Naz, M. Li, C. Wang, Y. Illarionov, Mater. Res. Bull. 193 (2026) 113648.
[139] W. Ahmad, M.Z. Nawaz, J. Kazmi, U. Younis, Y. Illarionov, Z. Wang, Adv. Opt. Mater. 13 (2025) e01067.
[140] G. Naz, H. Khursheed, A. Hussain, H.M.A. Sharif, M. Arshad, F.K. Butt, M. Z. Nawaz, A.A. Hendi, M.M. Almoneef, M.A. Awad, Mater. Today Commun. 40 (2024) 110106.
[141] J. Zhang, M.Z. Nawaz, X. Zhou, L. Xu, J. Wu, C. Wang, Chem. Lett. 52 (2023) 365–369.
[142] M.Z. Nawaz, L. Xu, X. Zhou, J. Li, K.H. Shah, J. Wang, B. Wu, C. Wang, ACS Appl. Mater. Interfaces 14 (2022) 19659–19671.
[143] G.M. Swain, Adv. Mater. 6 (1994) 388–392.
[144] T. Li, C. Tang, H. Guo, H. Wu, C. Duan, H. Wang, F. Zhang, Y. Cao, G. Yang, Y. Zhou, ACS Appl. Mater. Interfaces 14 (2022) 49765–49773.
[145] Y. Liu, B. Deng, K. Li, H. Wang, Y. Sun, F. Dong, J. Colloid Interface Sci. 614 (2022) 405–414.
[146] Y. Song, D. Johnson, R. Peng, D.K. Hensley, P.V. Bonnesen, L. Liang, J. Huang, F. Yang, F. Zhang, R. Qiao, A.P. Baddorf, T.J. Tschaplinski, N.L. Engle, M. C. Hatzell, Z. Wu, D.A. Cullen, H.M. Meyer, B.G. Sumpter, A.J. Rondinone, Sci. Adv. 4 (2018) e1700336.
[147] M. Fu, Y. Mao, H. Wang, W. Luo, Y. Jiang, W. Shen, M. Li, R. He, Chin. Chem. Lett. 35 (2024) 108341.
[148] S. Zhang, J. Wu, M. Zheng, X. Jin, Z. Shen, Z. Li, Y. Wang, Q. Wang, X. Wang, H. Wei, J. Zhang, P. Wang, S. Zhang, L. Yu, L. Dong, Q. Zhu, H. Zhang, J. Lu, Nat. Commun. 14 (2023) 3634.
[149] K. Zhang, P. Sun, Y. Huang, M. Tang, X. Zou, Z. Pan, X. Huo, J. Wu, C. Lin, Z. Sun, Y. Wan, X. Zhang, L. An, Adv. Funct. Mater. 34 (2024) 2405179.
[150] J. Zhong, H. Duan, M. Cai, Y. Zhu, Z. Wang, X. Li, Z. Zhang, W. Qu, K. Zhang, D. Han, D. Cheng, Y. Shen, M. Xie, E. Cortes, D. Zhang, Angew. Chem. Int. Ed. 64 (2025) e202507956.
[151] L. Li, C. Tang, D. Yao, Y. Zheng, S.-Z. Qiao, ACS Energy Lett. 4 (2019) 2111–2116.
[152] L. Zhou, C.E. Boyd, Aquaculture 450 (2016) 187–193.
[153] M. Yasir, Z. Zhao, Y. Hu, X. Zhang, H. Wang, Nano Energy 135 (2025) 110693.
[154] J. Yang, H. Qi, A. Li, X. Liu, X. Yang, S. Zhang, Q. Zhao, Q. Jiang, Y. Su, L. Zhang, J.-F. Li, Z.-Q. Tian, W. Liu, A. Wang, T. Zhang, J. Am. Chem. Soc. 144 (2022) 12062–12071.
[155] J. Li, G. Zhan, J. Yang, F. Quan, C. Mao, Y. Liu, B. Wang, F. Lei, L. Li, A.W. M. Chan, L. Xu, Y. Shi, Y. Du, W. Hao, P.K. Wong, J. Wang, S.-X. Dou, L. Zhang, J. C. Yu, J. Am. Chem. Soc. 142 (2020) 7036–7046.
[156] J. Yano, V.K. Yachandra, Photosynth. Res. 102 (2009) 241–254.
[157] J. Timoshenko, B. Roldan Cuenya, Chem. Rev. 121 (2021) 882–961.
[158] X. Chen, S. Lv, J. Kang, Z. Wang, T. Guo, Y. Wang, G. Teobaldi, L.-M. Liu, L. Guo, Proceedings of the National Academy of Sciences USA 120 (2023) e2306841120.
[159] M. Wang, S. Liu, H. Ji, T. Yang, T. Qian, C. Yan, Nat. Commun. 12 (2021) 3198.
[160] K. Chu, Y. Luo, P. Shen, X. Li, Q. Li, Y. Guo, Adv. Energy Mater. 12 (2022) 2103022.
[161] P. Shen, X. Li, Y. Luo, N. Zhang, X. Zhao, K. Chu, Appl. Catal. B Environ. 316 (2022) 121651.
[162] R. Daiyan, T. Tran-Phu, P. Kumar, K. Iputera, Z. Tong, J. Leverett, M.H.A. Khan, A. Asghar Esmailpour, A. Jalili, M. Lim, A. Tricoli, R.-S. Liu, X. Lu, E. Lovell, R. Amal, Energy Environ. Sci. 14 (2021) 3588–3598.
[163] J. Zhao, Y. Yuan, F. Zhao, W. Han, Q. Yuan, M. Kou, J. Zhao, C. Chen, S. Wang, Appl. Catal. B Environ. 340 (2024) 123265.
[164] D. Yao, C. Tang, L. Li, B. Xia, A. Vasileff, H. Jin, Y. Zhang, S.-Z. Qiao, Adv. Energy Mater. 10 (2020) 2001289.
[165] Y. Wan, H. Zhou, M. Zheng, Z.-H. Huang, F. Kang, J. Li, R. Lv, Adv. Funct. Mater. 31 (2021) 2100300.
[166] Z. Chang, G. Meng, Y. Chen, C. Chen, S. Han, P. Wu, L. Zhu, H. Tian, F. Kong, M. Wang, X. Cui, J. Shi, Adv. Mater. 35 (2023) 2304508.
[167] D.K. Yesudoss, B. Ngozichukwu, I. Gning, B.D. Ngom, A. Djire, ACS Energy Lett. 10 (2025) 1688–1699.
[168] M. Han, M. Guo, Y. Yun, Y. Xu, H. Sheng, Y. Chen, Y. Du, K. Ni, Y. Zhu, M. Zhu, Adv. Funct. Mater. 32 (2022) 2202820.
[169] S. Liu, T. Qian, M. Wang, H. Ji, X. Shen, C. Wang, C. Yan, Nature Catalysis 4 (2021) 322–331.
[170] J.-Y. Fang, Q.-Z. Zheng, Y.-Y. Lou, K.-M. Zhao, S.-N. Hu, G. Li, O. Akdim, X.-Y. Huang, S.-G. Sun, Nat. Commun. 13 (2022) 7899.
[171] X. Zhang, X. Zhu, S. Bo, C. Chen, M. Qiu, X. Wei, N. He, C. Xie, W. Chen, J. Zheng, P. Chen, S.P. Jiang, Y. Li, Q. Liu, S. Wang, Nat. Commun. 13 (2022) 5337.
[172] Q. Liu, L. Xie, J. Liang, Y. Ren, Y. Wang, L. Zhang, L. Yue, T. Li, Y. Luo, N. Li, B. Tang, Y. Liu, S. Gao, A.A. Alshehri, I. Shakir, P.O. Agboola, Q. Kong, Q. Wang, D. Ma, X. Sun, Small 18 (2022) 2106961.
[173] T. Matsui, S. Suzuki, Y. Katayama, K. Yamauchi, T. Okanishi, H. Muroyama, K. Eguchi, Langmuir 31 (2015) 11717–11723.
[174] A.A. Abd-El-Latif, C.J. Bondue, S. Ernst, M. Hegemann, J.K. Kaul, M. Khodayari, E. Mostafa, A. Stefanova, H. Baltruschat, TrAC Trends Anal. Chem. 70 (2015) 4–13.
[175] W. Chen, F. He, Y.-X. Chen, Current Opinion in Electrochemistry 42 (2023) 101393.
[176] M. Duca, M.O. Cucarella, P. Rodriguez, M.T.M. Koper, J. Am. Chem. Soc. 132 (2010) 18042–18044.
[177] N. Meng, Y. Huang, Y. Liu, Y. Yu, B. Zhang, Cell Rep. Phys. Sci. 2 (2021) 100378.
[178] H. Wang, Y. Jiang, S. Li, F. Gou, X. Liu, Y. Jiang, W. Luo, W. Shen, R. He, M. Li, Appl. Catal. B Environ. 318 (2022) 121819.
[179] Y. Yao, S. Zhu, H. Wang, H. Li, M. Shao, Angew. Chem. Int. Ed. 59 (2020) 10479–10483.
[180] Y. Pan, X. Shan, F. Cai, H. Gao, J. Xu, M. Zhou, Angew. Chem. Int. Ed. 63 (2024) e202407116.

[181] D. Reyter, D. Bélanger, L. Roué, Electrochim. Acta 53 (2008) 5977–5984.
[182] N. Shpigel, M.D. Levi, S. Sigalov, L. Daikhin, D. Aurbach, Acc. Chem. Res. 51 (2018) 69–79.
[183] X. Wei, X. Wen, Y. Liu, C. Chen, C. Xie, D. Wang, M. Qiu, N. He, P. Zhou, W. Chen, J. Cheng, H. Lin, J. Jia, X.-Z. Fu, S. Wang, J. Am. Chem. Soc. 144 (2022) 11530–11535.
[184] M.S. Saleem, Y. Wang, C. Nie, X. Zhang, Y. Zhang, H. Li, K. Liu, J. Song, M. Cheng, S. Ma, L. Wang, M.Z. Nawaz, L. Zhang, M.-H. Zhao, J. Zhong, G. Luo, C. Li, Adv. Funct. Mater., e24555. Doi: https://doi.org/10.1002/adfm.202524555.
[185] Y.-B. Li, Y.-P. Liu, J. Wang, Y.-L. Guo, K. Chu, Inorganic Chemistry Frontiers 7 (2020) 455–463.
[186] X. Wang, X. Wu, W. Ma, X. Zhou, S. Zhang, D. Huang, L.R. Winter, J.-H. Kim, M. Elimelech, Proceedings of the National Academy of Sciences USA 120 (2023) e2217703120.
[187] Q. Li, N. Xia, Y. Zhu, Y. Gao, Y. Liu, H. Wang, Chem. Eng. J. 515 (2025) 163947.
[188] S. Bhowmick, A. Adalder, A. Maiti, S. Kapse, R. Thapa, S. Mondal, U.K. Ghorai, Chem. Sci. 16 (2025) 4806–4814.
[189] Y. Guo, X. Cai, S. Shen, G. Wang, J. Zhang, J. Catal. 402 (2021) 1–9.
[190] Y. Tan, Y. Xu, Y. Cao, Y. Zhao, J. Phys. Chem. C 126 (2022) 13147–13156.
[191] J. Wang, L. Yu, L. Hu, G. Chen, H. Xin, X. Feng, Nat. Commun. 9 (2018) 1795.
[192] J. Kang, X. Chen, R. Si, X. Gao, S. Zhang, G. Teobaldi, A. Selloni, L.-M. Liu, L. Guo, Angew. Chem. Int. Ed. 62 (2023) e202217428.
[193] Y. Wang, H. Li, W. Zhou, X. Zhang, B. Zhang, Y. Yu, Angew. Chem. Int. Ed. 61 (2022) e202202604.
[194] R. Han, R. Hu, H. Zhao, P. Liu, Y.-Q. Wang, Chem. Eng. J. 520 (2025) 165995.
[195] C. Lin, X. Chen, L. Wang, W. Li, Z. Wang, M. Li, J. Feng, B. Hou, W. Yan, Adv. Funct. Mater. 34 (2024) 2401287.
[196] X. Zhang, C. Wang, Y. Guo, B. Zhang, Y. Wang, Y. Yu, J. Mater. Chem. A 10 (2022) 6448–6453.
[197] L. Chen, Q. Wang, H. Gong, M. Xue, Appl. Surf. Sci. 546 (2021) 149131.
[198] K.S. Exner, Acc. Chem. Res. 57 (2024) 1336–1345.
[199] S.M. Stratton, S. Zhang, M.M. Montemore, Surf. Sci. Rep. 78 (2023) 100597.
[200] P. Su, Y. Li, Z. Ke 16 (2021) 3427–3436.
[201] M.D. Wodrich, B. Sawatlon, M. Busch, C. Corminboeuf, Acc. Chem. Res. 54 (2021) 1107–1117.
[202] Y. Li, Z. Ren, Z. He, P. Ouyang, Y. Duan, W. Zhang, K. Lv, F. Dong, Green Energy Environ. 9 (2024) 623–658.
[203] S. Du, J. Fang, M. Guo, G. Yang, Q. Zhang, Z. Liu, F. Peng, ACS Sustain. Chem. Eng. 12 (2024) 16320–16328.
[204] W. Fu, Y. Cao, Q. Feng, W.R. Smith, P. Dong, M. Ye, J. Shen, Nanoscale 11 (2019) 1379–1385.
[205] X. Huo, D.J. Van Hoomissen, J. Liu, S. Vyas, T.J. Strathmann, Appl. Catal. B Environ. 211 (2017) 188–198.
[206] X. Chen, X. Huo, J. Liu, Y. Wang, C.J. Werth, T.J. Strathmann, Chem. Eng. J. 313 (2017) 745–752.
[207] H. Xu, Y. Ma, J. Chen, W.-X. Zhang, J. Yang, Chem. Soc. Rev. 51 (2022) 2710–2758.
[208] Z. Wang, S.D. Young, B.R. Goldsmith, N. Singh, J. Catal. 395 (2021) 143–154.
[209] J. Su, K. Shi, B. Liu, Z. Xi, J. Yu, X. Xu, P. Jing, R. Gao, J. Zhang, Adv. Funct. Mater. 34 (2024) 2401194.
[210] W. Gao, K. Xie, J. Xie, X. Wang, H. Zhang, S. Chen, H. Wang, Z. Li, C. Li, Adv. Mater. 35 (2023) 2202952.
[211] S. Xu, Y. Zhu, Z. Wen, S. Yu, Z. Teng, G. Liu, H. Gao, R. Zhao, L. Sun, F. Li, Chem Catalysis 3 (2023) 100751.
[212] Y. Yao, L. Zhao, J. Dai, J. Wang, C. Fang, G. Zhan, Q. Zheng, W. Hou, L. Zhang, Angew. Chem. Int. Ed. 61 (2022) e202208215.
[213] M. Jiang, A. Tao, Y. Hu, L. Wang, K. Zhang, X. Song, W. Yan, Z. Tie, Z. Jin, ACS Appl. Mater. Interfaces 14 (2022) 17470–17478.
[214] X. Zhao, Y. Jiang, M. Wang, S. Liu, Z. Wang, T. Qian, C. Yan, Adv. Energy Mater. 13 (2023) 2301409.
[215] Y. Wang, F. Hao, M. Sun, M.-T. Liu, J. Zhou, Y. Xiong, C. Ye, X. Wang, F. Liu, J. Wang, P. Lu, Y. Ma, J. Yin, H.-C. Chen, Q. Zhang, L. Gu, H.M. Chen, B. Huang, Z. Fan, Adv. Mater. 36 (2024) 2313548.
[216] H. Cao, B. Liang, S. Ye, Z. Zhuang, L. Zheng, W. Chen, W. Chen, J. Zhang, Q. Zhang, J. Liu, X. Yan, Q. Zhang, Chem. Eng. J. 490 (2024) 151883.
[217] W. Zhu, F. Yao, Q. Wu, Q. Jiang, J. Wang, Z. Wang, H. Liang, Energy Environ. Sci. 16 (2023) 2483–2493.
[218] J. Liu, ACS Catal. 7 (2017) 34–59.
[219] M.Z. Nawaz, M. Bilal, H. Gulzar, H. Gulzar, R.Z.A. Manj, M.S. Saleem, I.M. Ul Hasan, M.A. Rafiq, G. Naz, H.M.N.U.H.K. Asghar, M. Javed, M. Li, ACS Appl. Nano Mater. 7 (2024) 15354–15364.
[220] Y. Zhou, L. Zhang, Z. Zhu, M. Wang, N. Li, T. Qian, C. Yan, J. Lu 63 (2024) e202319029.
[221] J. Lim, C.-Y. Liu, J. Park, Y.-H. Liu, T.P. Senftle, S.W. Lee, M.C. Hatzell, ACS Catal. 11 (2021) 7568–7577.
[222] H. Guo, M. Li, Y. Yang, R. Luo, W. Liu, F. Zhang, C. Tang, G. Yang, Y. Zhou, Small 19 (2023) 2207743.
[223] L. Bai, F. Franco, J. Timoshenko, C. Rettenmaier, F. Scholten, H.S. Jeon, A. Yoon, M. Rüscher, A. Herzog, F.T. Haase, S. Kühl, S.W. Chee, A. Bergmann, R.C. Beatriz, J. Am. Chem. Soc. 146 (2024) 9665–9678.
[224] Y. Xu, K. Ren, T. Ren, M. Wang, M. Liu, Z. Wang, X. Li, L. Wang, H. Wang, Chem. Commun. 57 (2021) 7525–7528.
[225] J. Xiang, H. Zhao, K. Chen, X. Li, X. Li, K. Chu, J. Colloid Interface Sci. 653 (2024) 390–395.
[226] X. Li, X. Zhao, Y. Zhou, J. Hu, H. Zhang, X. Hu, G. Hu, Appl. Surf. Sci. 584 (2022) 152556.
[227] M. Jiang, J. Su, X. Song, P. Zhang, M. Zhu, L. Qin, Z. Tie, J.-L. Zuo, Z. Jin, Nano Lett. 22 (2022) 2529–2537.
[228] F. Zhang, J. Chen, G.G. Wallace, J. Yang, Prog. Mater. Sci. 133 (2023) 101069.
[229] K. Wang, J. Pan, J. Hu, X. Fu, Y. Dou, H. Xian, H. Guo, J. Song Chen, T. Li, Chem. Eng. J. 482 (2024) 148883.
[230] X. Yu, S. Du, Z. Xu, J. He, F. Liu, B. Wang, S. Sun, Y. Tang, K. Zhao, Chem. Eng. J. 480 (2024) 148152.
[231] M. Xie, G. Zhu, H. Yang, B. Liu, M. Li, C. Qi, L. Wang, W. Jiang, P. Qiu, W. Luo, Adv. Energy Mater. 14 (2024) 2401717.
[232] K. Chen, Z. Ma, X. Li, J. Kang, D. Ma, K. Chu, Adv. Funct. Mater. 33 (2023) 2209890.
[233] L. Qin, F. Sun, Z. Gong, G. Ma, Y. Chen, Q. Tang, L. Qiao, R. Wang, Z.-Q. Liu, Z. Tang, ACS Nano 17 (2023) 12747–12758.
[234] H. Choi, M. Jun, W. Kang, T. Kim, S. Choi, C. Choi, H. Wang, H. Baik, Y. Jung, K. Jin, K. Lee, Chem Catalysis 4 (2024).
[235] Y. Xu, W. Xu, Z. Gao, Y. Liang, H. Jiang, Z. Li, Z. Cui, E. Liu, L. Ma, S. Zhu, ACS Appl. Mater. Interfaces 17 (2025) 26692–26700.
[236] Y. Ma, J. Wang, Q. Liu, Z. Li, L. Wang, Chem. Commun. 61 (2025) 8544–8547.
[237] X. Rao, S. Feng, Y. Zou, L. Wang, M.-F. Chien, C. Inoue, Y. Liu, Sep. Purif. Technol. 354 (2025) 129286.
[238] Y. Jiang, D. Kong, L. Huang, S. Wu, P. Xu, L. Ye, X. Zhou, J. Qian, H. Tang, Y. Ge, J. Guan, Z. Yang, H. Nie, Appl. Catal. B Environ. Energy 356 (2024) 124224.
[239] X. Wen, Y. Zhao, P. Fan, J. Wu, K. Xiong, C. Liu, Q. Qu, L. Li, Green Chem. 26 (2024) 968–978.
[240] B. Shi, L. Zhang, R. Qi, M. Xia, X. Yu, M. Zhong, W. Song, X. Lu, J. Colloid Interface Sci. 696 (2025) 137837.
[241] Z. Fan, C. Cao, X. Yang, W. Yuan, F. Qin, Y. Hu, X. Sun, G. Liu, Y. Tian, L. Xu, Angew. Chem. Int. Ed. 63 (2024) e202410356.
[242] M. Zhang, Z. Ma, S. Zhou, C. Han, V. Kundi, P.V. Kumar, L. Thomsen, B. Johannessen, L. Peng, Y. Shan, C. Tsounis, Y. Yang, J. Pan, R. Amal, ACS Catal. 14 (2024) 11231–11242.
[243] S. Liu, W. Miao, K. Ma, H. Teng, X. Zhang, J. Li, W. Li, X. Cui, L. Jiang, Appl. Catal. B Environ. Energy 350 (2024) 123919.
[244] H. Liu, J. Timoshenko, L. Bai, Q. Li, M. Rüscher, C. Sun, B. Roldan Cuenya, J. Luo, ACS Catal. 13 (2023) 1513–1521.
[245] W. Zhong, Q.-L. Hong, X. Ai, C. Zhang, F.-M. Li, X.-F. Li, Y. Chen, Adv. Mater. 36 (2024) 2314351.
[246] K. Chen, Z. Wang, L. Wang, X. Wu, B. Hu, Z. Liu, M. Wu, Nano-Micro Lett. 13 (2021) 138.
[247] J.-Y. Zhu, Q. Xue, Y.-Y. Xue, Y. Ding, F.-M. Li, P. Jin, P. Chen, Y. Chen, ACS Appl. Mater. Interfaces 12 (2020) 14064–14070.
[248] K. Chen, G. Wang, Y. Guo, D. Ma, K. Chu, Nano Res. 16 (2023) 8737–8742.
[249] T. Jin, J. Wang, Y. Gong, Q. Zheng, T. Wang, R. Wu, Y. Lyu, X. Liu, Chem Catalysis 3 (2023) 100477.
[250] Z.-N. Zhang, Q.-L. Hong, X.-H. Wang, H. Huang, S.-N. Li, Y. Chen, Small 19 (2023) 2300530.
[251] I. Masood Ul Hasan, L. Bo, N. Zhengrong, G. Dandan, Z. Yaoling, X. Li, M. Z. Nawaz, M. Ikram, M. Irfan, K. Hussain, H. Feng, Earth Syst. Environ. (2025). https://doi.org/10.1007/s41748-025-00789-7.
[252] M. Qadeer, Q. Guan, Q. Guo, A. Rahman, M.Z. Nawaz, J. Zhou, S. Zhu 7 (2022) 2200002.
[253] S. Luo, X. Li, B. Zhang, Z. Luo, M. Luo, ACS Appl. Mater. Interfaces 11 (2019) 26891–26897.
[254] Y. Liu, L. Huang, X. Zhu, Y. Fang, S. Dong, Nanoscale 12 (2020) 1811–1816.
[255] T. Ding, M. Wang, F. Wu, B. Song, K. Lu, H. Zhang, ACS Appl. Energy Mater. 7 (2024) 11475–11496.
[256] Y. Chen, B. Wu, B. Sun, N. Wang, W. Hu, S. Komarneni, ACS Sustain. Chem. Eng. 7 (2019) 18874–18883.
[257] L. Zheng, Y. Zhang, W. Chen, X. Xu, R. Zhang, X. Ren, X. Liu, W. Wang, J. Qi, G. Wang, C. Ma, L. Xu, P. Han, Q. He, D. Ma, J. Wang, C. Ling, D. Su, M. Shao, Y. Chen, Angew. Chem. Int. Ed. 64 (2025) e202500985.
[258] Y. Liu, Y. Su, X. Quan, X. Fan, S. Chen, H. Yu, H. Zhao, Y. Zhang, J. Zhao, ACS Catal. 8 (2018) 1186–1191.
[259] X. Lu, J. Yu, J. Cai, Q. Zhang, S. Yang, L. Gu, G.I.N. Waterhouse, S.-Q. Zang, B. Yang, S. Lu, Cell Rep. Phys. Sci. 3 (2022).
[260] X. Li, Y. Gu, S. Wu, S. Chen, X. Quan, H. Yu, Chemosphere 285 (2021) 131501.
[261] P. Wei, H. Xie, X. Zhu, R. Zhao, L. Ji, X. Tong, Y. Luo, G. Cui, Z. Wang, X. Sun, ACS Sustain. Chem. Eng. 8 (2020) 29–33.
[262] W. Kang, L. Yan, J. Tang, S. Wu, H. Yu, Z. Li, Appl. Catal. B Environ. 329 (2023) 122553.
[263] Y. Wu, Y. Gu, W. Kang, H. Yu, S. Chen, X. Quan, N. Lu, Chem. Eng. J. 452 (2023) 139126.
[264] L. Huang, L. Cheng, T. Ma, J.-J. Zhang, H. Wu, J. Su, Y. Song, H. Zhu, Q. Liu, M. Zhu, Z. Zeng, Q. He, M.-K. Tse, D.-t. Yang, B.I. Yakobson, B.Z. Tang, Y. Ren, R. Ye, Adv. Mater., 35 (2023) 2211856.
[265] F. Jiao, B. Xu, Adv. Mater. 31 (2019) 1805173.
[266] G.-F. Chen, Y. Yuan, H. Jiang, S.-Y. Ren, L.-X. Ding, L. Ma, T. Wu, J. Lu, H. Wang, Nat. Energy 5 (2020) 605–613.
[267] H. Huang, F. Gong, Y. Wang, H. Wang, X. Wu, W. Lu, R. Zhao, H. Chen, X. Shi, A. M. Asiri, T. Li, Q. Liu, X. Sun, Nano Res. 12 (2019) 1093–1098.
[268] S. Chen, Y. Liang, M. Bu, Z. Dai, J. Shi, Catal. Lett. 154 (2024) 1795–1805.
[269] L. Cheng, T. Ma, B. Zhang, L. Huang, W. Guo, F. Hu, H. Zhu, Z. Wang, T. Zheng, D.-T. Yang, C.-K. Siu, Q. Liu, Y. Ren, C. Xia, B.Z. Tang, R. Ye, ACS Catal. 12 (2022) 11639–11650.
[270] X. Huang, Z. Liu, H. Yang, T. Ding, Z. Zhang, D. Yue, G. Shi, J. Power Sources 640 (2025) 236748.

[271] M.K.R. Souza, E.S.F. Cardoso, L.M.C. Pinto, I.S.C. Crivelli, C.D. Rodrigues, R. S. Souto, A.T. Rezende-Filho, M.R.V. Lanza, G. Maia, ACS Appl. Mater. Interfaces 17 (2025) 1295–1310.
[272] Y. Qu, T. Dai, G. Ding, Z. Feng, Z. Wang, Q. Jiang, J. Mater. Sci. Technol. 247 (2026) 226–234.
[273] H. Zou, W. Rong, B. Long, Y. Ji, L. Duan, ACS Catal. 9 (2019) 10649–10655.
[274] X. Liu, L. Zhao, Y. Shen, W. Peng, B. Mao, J. Hou, D. Wang, X. Chen, Y. Dai, C. Zhang, C. Hu, Adv. Mater. 37 (2025) 2417623.
[275] W. Wang, M. Li, M. Liang, Y. Lu, Q. He, F. Chen, J. Clean. Prod. 472 (2024) 143514.
[276] T. Wu, P. Li, H. Wang, R. Zhao, Q. Zhou, W. Kong, M. Liu, Y. Zhang, X. Sun, F. Gong, Chem. Commun. 55 (2019) 2684–2687.
[277] N.J. Harmon, J. Li, B.T. Wang, Y. Gao, H. Wang, ACS Catal. 14 (2024) 3575–3581.
[278] G. Jia, Y. Sun, P. Liu, J. Luo, P. Zhang, Y. Wei, W. Song, Z. Li, Z. Zhao, J. Liu, Nano Res. 18 (2025) 94907265.
[279] S. Chen, S. Perathoner, C. Ampelli, C. Mebrahtu, D. Su, G. Centi, Angew. Chem. Int. Ed. 56 (2017) 2699–2703.
[280] J. Yu, R.-T. Gao, X. Guo, N. Truong Nguyen, L. Wu, L. Wang, Angew. Chem. Int. Ed. 64 (2025) e202415975.
[281] J. Chen, K. Zuo, Y. Li, X. Huang, J. Hu, Y. Yang, W. Wang, L. Chen, A. Jain, R. Verduzco, X. Li, Q. Li, Water Res. 216 (2022) 118351.
[282] T. Wang, L. Niu, K. Zhang, Y. Wang, H. Guo, X. He, H. Xian, T. Li, Chem. Commun. 61 (2025) 3532–3535.
[283] M. Yang, J. Yang, N. He, S. Wang, H. Ni, J. Yuan, Y. Kang, Y. Liu, C. Zhou, L. Tong, B. Lu, X. Liu, Q. Wang, S. Huang, B. Feng, G. Guo, S. Han, Z. Han, ACS Appl. Nano Mater. 8 (2025) 179–188.
[284] W. Chen, X. Yang, Z. Chen, Z. Ou, J. Hu, Y. Xu, Y. Li, X. Ren, S. Ye, J. Qiu, J. Liu, Q. Zhang, Adv. Funct. Mater. 33 (2023) 2300512.
[285] H. Jung, J. Yang, J. Maeng, W.B. Kim, Y. Yun, Appl. Surf. Sci. 686 (2025) 162089.
[286] S. Kuramochi, A. Fiorani, Y. Einaga, ACS Sustain. Chem. Eng. 12 (2024) 12643–12651.
[287] M. Jiang, Y. Zhu, Z. Jia, X. Zhong, Q. Sun, Y. Wang, J. Yao, Small 9 (2025) 2401672.
[288] S. Bhardwaj, S.J. Alli, N. Barman, R. Thapa, R.S. Dey, ACS Appl. Mater. Interfaces 17 (2025) 26661–26670.
[289] M.J. Liu, C.A. Fernández Otero, D.U. Patino, H. Gong, M.D. Hossain, J. E. Matthews, K.S. Williams, A. Vargas, M.J. Zachman, A.S. Hoffman, D. Nordlund, M. Bajdich, S.R. Bare, M.B. Stevens, T.F. Jaramillo, Z. Bao, W.A. Tarpeh, J. Am. Chem. Soc. 147 (2025) 29026–29041.
[290] R. He, L. Sun, K. Ren, X. Li, P. Tian, G. Ning, J. Ye, ChemSusChem 18 (2025) e202500059.
[291] X. Zhou, W. Xu, Y. Huang, Z. Gao, Y. Liang, H. Jiang, Z. Li, F. Wang, S. Zhu, Z. Cui, Green Chem. 27 (2025) 6556–6566.
[292] B. Zhang, Z. Dai, Y. Chen, M. Cheng, H. Zhang, P. Feng, B. Ke, Y. Zhang, G. Zhang, Nat. Commun. 15 (2024) 2816.
[293] S. Lv, Y. Wang, D. Wang, C. Song, Chem. Eur. J. 30 (2024) e202400342.
[294] Z. Ma, C. Wang, T. Yang, G. Wei, J. Huang, M. Liu, K. Zhang, Z. Zhang, Y. Liu, S. Gao, J. Mater. Chem. A 12 (2024) 7654–7662.
[295] M. Wu, S. Li, K. Wei, H. Hu, Y. Song, Z. Zheng, H. Li, F. Gao, Inorganic Chemistry Frontiers 12 (2025) 6631–6639.
[296] Y. Ge, Y. Wang, Z. Liu, X. Xu, Y. Chen, Z. Yin, Q. Zhou, W. Yang, Water Res. 274 (2025) 123077.
[297] Z. Wang, S. Liu, X. Zhao, M. Wang, L. Zhang, T. Qian, J. Xiong, C. Yang, C. Yan, ACS Materials Letters 5 (2023) 1018–1026.
[298] Z. Zhang, A. Niu, Y. Lv, H. Guo, J.S. Chen, Q. Liu, K. Dong, X. Sun, T. Li, Angew. Chem. Int. Ed. 63 (2024) e202406441.
[299] Z. Zhang, T. Wang, J. Song Chen, K. Dong, S. Sun, Y. Luo, H. Guo, X. Sun, T. Li, J. Colloid Interface Sci. 648 (2023) 693–700.
[300] R. Cao, S. Yin, Y. Han, J. Zhang, W. Jiang, G. Liu, Coord. Chem. Rev. 538 (2025) 216722.
[301] S. Zhang, R. Zhang, Y. Guo, C. Zhi, EES Catal. 3 (2025) 235–253.
[302] G.A. Cerrón-Calle, A.S. Fajardo, C.M. Sánchez-Sánchez, S. Garcia-Segura, Appl. Catal. B Environ. 302 (2022) 120844.
[303] B. Xu, D. Li, Q. Zhao, S. Feng, X. Peng, P.K. Chu, Coord. Chem. Rev. 502 (2024) 215609.
[304] J. Zhao, L. Liu, Y. Yang, D. Liu, X. Peng, S. Liang, L. Jiang, ACS Sustain. Chem. Eng. 11 (2023) 2468–2475.
[305] Z. Ren, K. Shi, X. Feng, ACS Energy Lett. 8 (2023) 3658–3665.
[306] Q. Hu, Y. Qin, X. Wang, Z. Wang, X. Huang, H. Zheng, K. Gao, H. Yang, P. Zhang, M. Shao, C. He, Energy Environ. Sci. 14 (2021) 4989–4997.
[307] Y. Wang, X. Qin, M. Shao, J. Catal. 400 (2021) 62–70.
[308] T. Zhu, Q. Chen, P. Liao, W. Duan, S. Liang, Z. Yan, C. Feng, Small 16 (2020) 2004526.
[309] Y. Wang, W. Zhang, W. Wen, X. Yu, Y. Du, K. Ni, Y. Zhu, M. Zhu, Adv. Funct. Mater. 33 (2023) 2302651.
[310] C. Li, S. Liu, Y. Xu, T. Ren, Y. Guo, Z. Wang, X. Li, L. Wang, H. Wang, Nanoscale 14 (2022) 12332–12338.
[311] Y. Li, J. Wei, H. Lin, Y. Guo, X. Lu, S. Liu, H. Liu, M. Tang, J. Zhou, Y.-y. Li, ACS Catal., 15 (2025) 1672-1683.
[312] Y.-X. Lin, S.-N. Zhang, Z.-H. Xue, J.-J. Zhang, H. Su, T.-J. Zhao, G.-Y. Zhai, X.-H. Li, M. Antonietti, J.-S. Chen, Nat. Commun. 10 (2019) 4380.
[313] E. Zhang, T. Wang, K. Yu, J. Liu, W. Chen, A. Li, H. Rong, R. Lin, S. Ji, X. Zheng, Y. Wang, L. Zheng, C. Chen, D. Wang, J. Zhang, Y. Li, J. Am. Chem. Soc. 141 (2019) 16569–16573.
[314] T. Ren, K. Ren, M. Wang, M. Liu, Z. Wang, H. Wang, X. Li, L. Wang, Y. Xu, Chem. Eng. J. 426 (2021) 130759.
[315] C. Li, S. Mou, X. Zhu, F. Wang, Y. Wang, Y. Qiao, X. Shi, Y. Luo, B. Zheng, Q. Li, X. Sun, Chem. Commun. 55 (2019) 14474–14477.
[316] W. Fu, Z. Hu, Y. Zheng, P. Su, Q. Zhang, Y. Jiao, M. Zhou, Chem. Eng. J. 433 (2022) 133680.
[317] R. Qi, L. Zhang, S. Ren, B. Shi, M. Zhong, Z.-j. Chen, X. Lu, Nano Lett., 24 (2024) 8964-8972.
[318] K. Wu, C. Sun, Z. Wang, Q. Song, X. Bai, X. Yu, Q. Li, Z. Wang, H. Zhang, J. Zhang, X. Tong, Y. Liang, A. Khosla, Z. Zhao, ACS Materials Letters 4 (2022) 650–656.
[319] Y.-T. Xu, M.-Y. Xie, H. Zhong, Y. Cao, ACS Catal. 12 (2022) 8698–8706.
[320] G. Ma, F. Sun, L. Qiao, Q. Shen, L. Wang, Q. Tang, Z. Tang, Nano Res. 16 (2023) 10867–10872.
[321] Z. Gong, W. Zhong, Z. He, Q. Liu, H. Chen, D. Zhou, N. Zhang, X. Kang, Y. Chen, Appl. Catal. B Environ. 305 (2022) 121021.
[322] Y. Xu, K. Ren, T. Ren, M. Wang, Z. Wang, X. Li, L. Wang, H. Wang, Appl. Catal. B Environ. 306 (2022) 121094.
[323] X. Zhang, W. Li, J. Zhang, H. Zhou, M. Zhong, Chin. J. Catal. 68 (2025) 404–413.
[324] H. Huang, F. Li, Q. Xue, Y. Zhang, S. Yin, Y. Chen, Small 15 (2019) 1903500.
[325] Y. Wang, X. Cui, J. Zhao, G. Jia, L. Gu, Q. Zhang, L. Meng, Z. Shi, L. Zheng, C. Wang, Z. Zhang, W. Zheng, ACS Catal. 9 (2019) 336–344.
[326] J. Li, X. Zhu, T. Wang, Y. Luo, X. Sun, Inorganic Chemistry Frontiers 6 (2019) 2682–2685.
[327] X. Liu, T. Xie, Z. Cai, Z. Li, L. Zhang, X. Fan, D. Zhao, S. Sun, Y. Luo, Q. Liu, X. Sun, J. Electroanal. Chem. 933 (2023) 117295.
[328] W. Yang, Z. Chang, X. Yu, R. Shen, L. Wang, X. Cui, J. Shi, Angew. Chem. Int. Ed. 64 (2025) e202415300.
[329] W. Xiong, Z. Guo, S. Zhao, Q. Wang, Q. Xu, X. Wang, J. Mater. Chem. A 7 (2019) 19977–19983.
[330] J. Xu, S. Zhang, H. Liu, S. Liu, Y. Yuan, Y. Meng, M. Wang, C. Shen, Q. Peng, J. Chen, X. Wang, L. Song, K. Li, W. Chen, Angew. Chem. Int. Ed. 62 (2023) e202308044.
[331] J. Song, S.-j. Qian, W. Yang, J. Mu, J. Li, Y. Liu, F. Sun, S. Yu, F. Xu, X. Song, D. Deng, Y.-g. Wang, L. Yan, Y. Ding, Adv. Funct. Mater., 34 (2024) 2409089.
[332] X. Cui, C. Tang, X.-M. Liu, C. Wang, W. Ma, Q. Zhang, Chem. Eur. J. 24 (2018) 18494–18501.
[333] S. Qi, Z. Lei, Q. Huo, J. Zhao, T. Huang, N. Meng, J. Liao, J. Yi, C. Shang, X. Zhang, H. Yang, Q. Hu, C. He, Adv. Mater. 36 (2024) 2403958.
[334] K. Chandra Majhi, H. Chen, A. Batool, Q. Zhu, Y. Jin, S. Liu, P.H.-L. Sit, J. Chun-Ho Lam, Angew. Chem. Int. Ed. 64 (2025) e202500167.
[335] S. Tang, M. Xie, S. Yu, X. Zhan, R. Wei, M. Wang, W. Guan, B. Zhang, Y. Wang, H. Zhou, G. Zheng, Y. Liu, J.H. Warner, G. Yu, Nat. Commun. 15 (2024) 6932.
[336] G. Zhang, X. Li, K. Chen, Y. Guo, D. Ma, K. Chu, Angew. Chem. Int. Ed. 62 (2023) e202300054.
[337] H. Wang, S. Yuan, Y. Jia, Y. Xue, D. Zhao, J. Fan, W.-x. Zhang, Chem. Eng. J., 521 (2025) 166686.
[338] L. Zhang, M. Cong, X. Ding, Y. Jin, F. Xu, Y. Wang, L. Chen, L. Zhang, Angew. Chem. Int. Ed. 59 (2020) 10888–10893.
[339] F. Lü, S. Zhao, R. Guo, J. He, X. Peng, H. Bao, J. Fu, L. Han, G. Qi, J. Luo, X. Tang, X. Liu, Nano Energy 61 (2019) 420–427.
[340] X. Xiang, Z. Wang, X. Shi, M. Fan, X. Sun, ChemCatChem 10 (2018) 4530–4535.
[341] W. Zhong, Y. Chen, P. Chen, Q. Chen, C. Yang, N. Zhang, X. Liu, Z. Lin, Angew. Chem. Int. Ed. 64 (2025) e202503117.
[342] X. Fan, C. Liu, X. He, Z. Li, L. Yue, W. Zhao, J. Li, Y. Wang, T. Li, Y. Luo, D. Zheng, S. Sun, Q. Liu, L. Li, W. Chu, F. Gong, B. Tang, Y. Yao, X. Sun, Adv. Mater. 36 (2024) 2401221.
[343] P. Chen, N. Zhang, S. Wang, T. Zhou, Y. Tong, C. Ao, W. Yan, L. Zhang, W. Chu, C. Wu, Y. Xie, Proceedings of the National Academy of Sciences USA 116 (2019) 6635–6640.
[344] W. Guo, Z. Liang, J. Zhao, B. Zhu, K. Cai, R. Zou, Q. Xu 2 (2018) 1800204.
[345] A. Zhu, H. Liu, S. Bu, K. Liu, C. Luan, D. Lin, G. Gan, Y. Zhou, T. Zhang, K. Liu, G. Hong, H. Li, W. Zhang, ACS Nano 18 (2024) 22344–22355.
[346] W. Lin, E. Zhou, J.-F. Xie, J. Lin, Y. Wang, Adv. Funct. Mater. 32 (2022) 2209464.
[347] X. Li, Y. Chen, X. Zhan, Y. Xu, L. Hao, L. Xu, X. Li, M. Umer, X. Tan, B. Han, A. W. Robertson, Z. Sun, Innov. Mater. 1 (2023) 100014.
[348] S.-S. Li, Q.-Q. Xu, J.-T. Xu, G. Yan, Y.-X. Zhang, S.-W. Li, L.-C. Yin, Sensors Actuators B Chem. 354 (2022) 131095.
[349] J. Chen, W. Jia, X. Yu, Y. Sun, J. Zhang, S. Yang, X. Tang, L. Peng, X. Zeng, L. Lin, Fuel 332 (2023) 126137.
[350] J. Zhang, X. Tian, M. Liu, H. Guo, J. Zhou, Q. Fang, Z. Liu, Q. Wu, J. Lou, J. Am. Chem. Soc. 141 (2019) 19269–19275.
[351] X. Shi, W.-H. Huang, J. Rong, M. Xie, Q. Wa, P. Zhang, H. Wei, H. Zhou, M.-H. Yeh, C.-W. Pao, J. Wang, Z. Hu, X. Yu, J. Ma, H. Cheng, Nat. Commun. 16 (2025) 6161.
[352] Q. Wang, Y. Lei, D. Wang, Y. Li, Energy Environ. Sci. 12 (2019) 1730–1750.
[353] Z. Chen, W. Wei, Y. Shen, B.-J. Ni, Green Chem. 25 (2023) 5979–5988.
[354] Y. Chen, J. He, H. Pang, P. Jiang, F. Qu, D. Yu, J. Zhang, Sci. Total Environ. 850 (2022) 157845.
[355] Z. Deng, C. Ma, Z. Li, Y. Luo, L. Zhang, S. Sun, Q. Liu, J. Du, Q. Lu, B. Zheng, X. Sun, ACS Appl. Mater. Interfaces 14 (2022) 46595–46602.
[356] Z. Chen, X. Duan, W. Wei, S. Wang, B.-J. Ni, J. Mater. Chem. A 7 (2019) 14971–15005.
[357] Z. Niu, S. Fan, X. Li, Z. Liu, J. Wang, J. Duan, M.O. Tadé, S. Liu, ACS Appl. Mater. Interfaces 14 (2022) 35477–35484.
[358] K. Chu, Y.-p. Liu, Y.-b. Li, H. Zhang, Y. Tian, J. Mater. Chem. A, 7 (2019) 4389-4394.

[359] O.Q. Carvalho, R. Marks, H.K.K. Nguyen, M.E. Vitale-Sullivan, S.C. Martinez, L. Árnadóttir, K.A. Stoerzinger, J. Am. Chem. Soc. 144 (2022) 14809–14818.
[360] R. Qi, Q. Jiang, L. Deng, X. Yu, B. Shi, M. Zhong, Y. Wang, X. Lu, Chem. Sci. 16 (2025) 378–385.
[361] C. Wang, J. Li, F. Besenbacher, R. Su, Nano Materials Science (2024). https://doi.org/10.1016/j.nanoms.2024.10.010.
[362] M.Z. Nawaz, H. Gulzar, I.M. Ul Hasan, M.S. Saleem, A. Khaleeq, W. Ul Hasan, M. Imran, M. Li, H.M.N.U.H.K. Asghar, G. Naz, A. Baldycheva, M.F. Craciun, C. Wang, Y. Illarionov, ACS Applied Electronic Materials 6 (2024) 4381–4390.
[363] X. Fan, D. Zhao, Z. Deng, L. Zhang, J. Li, Z. Li, S. Sun, Y. Luo, D. Zheng, Y. Wang, B. Ying, J. Zhang, A.A. Alshehri, Y. Lin, C. Tang, X. Sun, Y. Zheng, Small 19 (2023) 2208036.
[364] Y. Yu, C. Wang, Y. Yu, Y. Wang, B. Zhang, SCIENCE CHINA Chem. 63 (2020) 1469–1476.
[365] T. Xu, Z. Wang, H. Zhu, Z. Zhang, Y. Zhang, D. Shang, L. Zhai, T. Yang, M. Wang, F. Yang, Chem. Commun. 61 (2025) 10387–10390.
[366] S. Zhang, W. Gong, Y. Lv, H. Wang, M. Han, G. Wang, T. Shi, H. Zhang, Chem. Commun. 55 (2019) 12376–12379.
[367] Q. Yao, J. Chen, S. Xiao, Y. Zhang, X. Zhou, ACS Appl. Mater. Interfaces 13 (2021) 30458–30467.
[368] J. Wang, H. Jang, G. Li, M.G. Kim, Z. Wu, X. Liu, J. Cho, Nanoscale 12 (2020) 1478–1483.
[369] L. Fang, S. Wang, C. Song, X. Yang, Y. Li, H. Liu, J. Hazard. Mater. 421 (2022) 126628.
[370] Y. Wang, A. Xu, Z. Wang, L. Huang, J. Li, F. Li, J. Wicks, M. Luo, D.-H. Nam, C.-S. Tan, Y. Ding, J. Wu, Y. Lum, C.-T. Dinh, D. Sinton, G. Zheng, E.H. Sargent, J. Am. Chem. Soc. 142 (2020) 5702–5708.
[371] X. Gu, J. Zhang, S. Guo, Y. Zhang, L. Xu, R. Jin, G. Li, J. Am. Chem. Soc. 147 (2025) 22785–22795.
[372] S. Zhu, K. Liu, Z. Feng, H. Jiang, J. Lin, Nano Research Energy 4 (2025) e9120188. https://doi.org/10.26599/NRE.2025.9120188.
[373] K. Chu, Y.-p. Liu, J. Wang, H. Zhang, ACS Appl. Energy Mater., 2 (2019) 2288-2295.
[374] F. Liu, J. Zhou, M. Sun, Z. Xu, H. Wang, N. Yao, Y. Wang, F. Hao, Y. Xiong, J. Wang, L. Guo, Q. Wa, G. Wang, X. Meng, M. Shao, C. Wang, H.-C. Chen, H. M. Chen, Y. Zhu, B. Huang, Z. Fan, Angew. Chem. Int. Ed. 64 (2025) e202504641.
[375] C. Guo, S. Yang, L. Wei, Z. Wang, J. Su, L. Guo, ACS Sustain. Chem. Eng. 13 (2025) 1604–1616.
[376] M. Zhao, R. Duan, Z. Zhang, Q. Mao, Q. Wang, Y. Zhou, X. Wang, C. Ding, C. Li, J. Mater. Chem. A 13 (2025) 25991–25997.
[377] Z. Zhang, M. Liu, B. Ge, T. Yang, S. Wang, Y. Liu, S. Gao, Chin. Chem. Lett. 36 (2025) 110657.
[378] Z. Mo, Z. Ma, Y. Ran, Y. Wang, T. Li, W. Sun, W. Hu, ChemSusChem 18 (2025) e202401607.
[379] F. Quan, P. Xu, X. Liu, W. Shen, Y. Li, J. Li, Y. He, F. Chen, J. Ind. Eng. Chem. (2025). https://doi.org/10.1016/j.jiec.2025.07.049.
[380] W. Zhang, S. Zhan, J. Xiao, T. Petit, C. Schlesiger, M. Mellin, J.P. Hofmann, T. Heil, R. Müller, K. Leopold, M. Oschatz, Adv. Sci. 10 (2023) 2302623.
[381] Y. Pan, Y. Liu, J. Zhao, K. Yang, J. Liang, D. Liu, W. Hu, D. Liu, Y. Liu, C. Liu, J. Mater. Chem. A 3 (2015) 1656–1665.
[382] D. Deng, S. Wu, H. Li, H. Li, L. Xu, Small 19 (2023) 2205469.
[383] H. Li, J. Shang, Z. Ai, L. Zhang, J. Am. Chem. Soc. 137 (2015) 6393–6399.
[384] S. Liu, M. Zhao, Z. He, Y. Zhong, H. Ding, D. Chen, Chin. J. Catal. 40 (2019) 446–457.
[385] X. Gao, Y. Shang, L. Liu, F. Fu, J. Catal. 371 (2019) 71–80.
[386] Q. Wang, W. Wang, L. Zhong, D. Liu, X. Cao, F. Cui, Appl. Catal. B Environ. 220 (2018) 290–302.
[387] Y. Liu, Z. Jiang, X. Zhang, P.K. Shen, J. Mater. Chem. A 6 (2018) 20037–20043.
[388] D.-L. Guan, C.-G. Niu, X.-J. Wen, H. Guo, C.-H. Deng, G.-M. Zeng, J. Colloid Interface Sci. 512 (2018) 272–281.
[389] Y. Han, Q. Fang, Q. Wu, H. Yin, X. Mao, X. Yan, Q. Li, X. Yao, A. Du, Small 21 (2025) e06191.
[390] W.J. Dong, J.P. Menzel, K. Li, Z. Ye, Z. Long, I.A. Navid, K.R. Yang, Y. Xiao, V. S. Batista, Z. Mi, Nat. Commun. 16 (2025) 3383.
[391] S. Nazari, J. Sun, M. Baharfar, P. Poulin, K. Kalantar-Zadeh, A. Jalili, D. Esrafilzadeh, Adv. Energy Mater. 14 (2024) 2304287.
[392] Y. Sun, X. Liu, M. Zhu, Z. Zhang, Z. Chen, S. Wang, Z. Ji, H. Yang, X. Wang, De Carbon 2 (2023) 100018.
[393] T. Liu, C. Chen, Z. Pu, Q. Huang, X. Zhang, A.M. Al-Enizi, A. Nafady, S. Huang, D. Chen, S. Mu, Small 20 (2024) 2405399.
[394] Y. Guo, R. Zhang, S. Zhang, Y. Zhao, Q. Yang, Z. Huang, B. Dong, C. Zhi, Energy Environ. Sci. 14 (2021) 3938–3944.
[395] X. Yang, R. Wang, S. Wang, C. Song, S. Lu, L. Fang, F. Yin, H. Liu, Appl. Catal. B Environ. 325 (2023) 122360.
[396] T. Wu, X. Zhu, Z. Xing, S. Mou, C. Li, Y. Qiao, Q. Liu, Y. Luo, X. Shi, Y. Zhang, X. Sun, Angew. Chem. Int. Ed. 58 (2019) 18449–18453.
[397] T. Feng, F. Li, X. Hu, Y. Wang, Chin. Chem. Lett. 34 (2023) 107862.
[398] X. Fan, X. He, X. Ji, L. Zhang, J. Li, L. Hu, X. Li, S. Sun, D. Zheng, Y. Luo, Y. Wang, L. Xie, Q. Liu, B. Ying, X. Sun, Inorganic Chemistry Frontiers 10 (2023) 1431–1435.
[399] L. Ouyang, X. He, S. Sun, Y. Luo, D. Zheng, J. Chen, Y. Li, Y. Lin, Q. Liu, A. M. Asiri, X. Sun, J. Mater. Chem. A 10 (2022) 23494–23498.
[400] Z. Li, Q. Zhou, J. Liang, L. Zhang, X. Fan, D. Zhao, Z. Cai, J. Li, D. Zheng, X. He, Y. Luo, Y. Wang, B. Ying, H. Yan, S. Sun, J. Zhang, A.A. Alshehri, F. Gong, Y. Zheng, X. Sun, Small 19 (2023) 2300291.
[401] Q. Song, S. Zhang, X. Hou, J. Li, L. Yang, X. Liu, M. Li, J. Hazard. Mater. 438 (2022) 129455.
[402] J. Wan, W. Chen, C. Jia, L. Zheng, J. Dong, X. Zheng, Y. Wang, W. Yan, C. Chen, Q. Peng, D. Wang, Y. Li, Adv. Mater. 30 (2018) 1705369.
[403] Z. Wang, B. Wen, Q. Hao, L.-M. Liu, C. Zhou, X. Mao, X. Lang, W.-J. Yin, D. Dai, A. Selloni, X. Yang, J. Am. Chem. Soc. 137 (2015) 9146–9152.
[404] H. Wu, H. Guo, F. Zhang, P. Yang, J. Liu, Y. Yang, Z.-F. Huang, C. Zhu, W. Wang, X. Tu, G. Yang, Y. Zhou, J. Mater. Chem. A 11 (2023) 22466–22477.
[405] Y.-T. Liu, X. Chen, J. Yu, B. Ding, Angew. Chem. Int. Ed. 58 (2019) 18903–18907.
[406] X.-E. Zhao, Z. Li, S. Gao, X. Sun, S. Zhu, Chem. Commun. 58 (2022) 12995–12998.
[407] X. He, J. Li, R. Li, D. Zhao, L. Zhang, X. Ji, X. Fan, J. Chen, Y. Wang, Y. Luo, D. Zheng, L. Xie, S. Sun, Z. Cai, Q. Liu, K. Ma, X. Sun, Inorg. Chem. 62 (2023) 25–29.
[408] C. Chaudhari, Y. Manaka, T. Nanba, Chemistry Select 9 (2024) e202304789.
[409] X. Wu, A. Ma, D. Liu, X. Li, Y. Zhou, A.T. Kuvarega, B.B. Mamba, H. Li, J. Gui, Sci. China-Mater. 66 (2023) 4367–4376.
[410] M. Yang, T. Wei, J. He, Q. Liu, L. Feng, H. Li, J. Luo, X. Liu, Nano Res. 17 (2024) 1209–1216.
[411] Y. Liang, X. Fan, X. He, D. Zheng, S. Sun, Y. Luo, H. Chen, X. Sun, Nano Res. 18 (2025) 94907344.
[412] J. Wang, K. Zhao, Y. Yao, F. Xue, F. Lu, W. Yan, F. Yuan, X. Wang, Nat. Commun. 16 (2025) 1129.
[413] Y.-T. Xu, Y. Han, D.K. Sam, Y. Cao, J. Mater. Chem. A 10 (2022) 22390–22398.
[414] D. Wu, H. Wan, J. Lin, Z. Zheng, C. Kuang, G. Chen, N. Zhang, X. Liu, R. Ma, Appl. Catal. B Environ. Energy 380 (2026) 125783.
[415] P. Lin, R. Chen, S. Xu, X. Xia, F. Zhao, X. Ren, Y. Lu, L. Gao, J. Bao, A. Liu, Catalysis Science & Technology 15 (2025) 1445–1455.
[416] X. Fan, C. Ma, D. Zhao, Z. Deng, L. Zhang, Y. Wang, Y. Luo, D. Zheng, T. Li, J. Zhang, S. Sun, Q. Lu, X. Sun, J. Colloid Interface Sci. 630 (2023) 714–720.
[417] X.-Y. Zhou, C.-X. Gao, M.-H. Guan, H.-N. Xu, J. Liu, H.-L. Wang, T. Wu, A.-H. Lu, ChemSusChem 18 (2025) e202501375.
[418] S. Zhang, M. Li, J. Li, Q. Song, X. Liu, Proc. Natl. Acad. Sci. 119 (2022) e2115504119.
[419] J. Wang, Y. Wang, C. Cai, Y. Liu, D. Wu, M. Wang, M. Li, X. Wei, M. Shao, M. Gu, Nano Lett. 23 (2023) 1897–1903.
[420] X. Fan, L. Xie, J. Liang, Y. Ren, L. Zhang, L. Yue, T. Li, Y. Luo, N. Li, B. Tang, Y. Liu, S. Gao, A.A. Alshehri, Q. Liu, Q. Kong, X. Sun, Nano Res. 15 (2022) 3050–3055.
[421] S. Mariya Varghese, A.V. Gopinathan, S. Rathnakumaran, S. Sasikumar, S. Kunnikuruvan, R.R. Gangavarapu, ACS Catal. 15 (2025) 5982–5992.
[422] M. Ran, G. Zhang, Chem. Eng. J. 516 (2025) 164104.
[423] J. Kang, Y. Xiao, L. Li, L. Qiao, C. Liu, C. Zhong, P. Sun, D. Liu, W.F. Ip, H. Pan, 2025 2507619.
[424] Q. Liu, Q. Liu, L. Xie, Y. Ji, T. Li, B. Zhang, N. Li, B. Tang, Y. Liu, S. Gao, Y. Luo, L. Yu, Q. Kong, X. Sun, ACS Appl. Mater. Interfaces 14 (2022) 17312–17318.
[425] Q. Yin, S. Hu, J. Liu, H. Zhou, Sustainable Energy & Fuels 6 (2022) 4716–4725.
[426] H. Zhao, Y. Duan, X. Cheng, C. Fan, Y.-Q. Wang, Dalton Trans. 53 (2024) 15674–15680.
[427] M.Z. Nawaz, A. Khaleeq, W.U. Hasan, W. Ahmad, R.Z.A. Manj, M.S. Saleem, I. Ullah, A. Irfan, I.M. Ul Hasan, M. Yaqub, H.M.N.U.H.K. Asghar, G. Naz, M. Li, C. Wang, Y.Y. Illarionov, ACS Appl. Nano Mater. 8 (2025) 11015–11025.
[428] M.Z. Nawaz, L. Xu, X. Zhou, M. Javed, J. Wang, B. Wu, C. Wang, ACS Appl. Mater. Interfaces 15 (2023) 14715–14726.
[429] Q. Hu, S. Qi, Q. Huo, Y. Zhao, J. Sun, X. Chen, M. Lv, W. Zhou, C. Feng, X. Chai, H. Yang, C. He, J. Am. Chem. Soc. 146 (2024) 2967–2976.
[430] L. Qiao, D. Liu, A. Zhu, J. Feng, P. Zhou, C. Liu, K.W. Ng, H. Pan, Appl. Catal. B Environ. 340 (2024) 123219.
[431] W. Lin, E. Zhou, J.-F. Xie, J. Lin, Y. Wang, Adv. Funct. Mater. 32 (2022) 2209464.
[432] X. Deng, Y. Yang, L. Wang, X.-Z. Fu, J.-L. Luo, Adv. Sci. 8 (2021) 2004523.
[433] T. Xie, X. Li, J. Li, J. Chen, S. Sun, Y. Luo, Q. Liu, D. Zhao, C. Xu, L. Xie, X. Sun, Inorg. Chem. 61 (2022) 14195–14200.
[434] X. Fan, C. Liu, Z. Li, Z. Cai, L. Ouyang, Z. Li, X. He, Y. Luo, D. Zheng, S. Sun, Y. Wang, B. Ying, Q. Liu, A. Farouk, M.S. Hamdy, F. Gong, X. Sun, Y. Zheng, Small 19 (2023) 2303424.
[435] X. Kang, X.-J. Yang, Z. Meng, X.-F. Sun, M.-M. Shi, H.-R. Li, R. Gao, B. Bi, D.-X. Liu, J.-M. Yan, Q. Jiang, Adv. Energy Mater. 14 (2024) 2303321.
[436] F. Zhao, G. Hai, X. Li, Z. Jiang, H. Wang, Chem. Eng. J. 461 (2023) 141960.
[437] Z. Li, G. Wen, J. Liang, T. Li, Y. Luo, Q. Kong, X. Shi, A.M. Asiri, Q. Liu, X. Sun, Chem. Commun. 57 (2021) 9720–9723.
[438] K. Fan, W. Xie, J. Li, Y. Sun, P. Xu, Y. Tang, Z. Li, M. Shao, Nat. Commun. 13 (2022) 7958.
[439] R. Zhao, Q. Yan, L. Yu, T. Yan, X. Zhu, Z. Zhao, L. Liu, J. Xi, Adv. Mater. 35 (2023) 2306633.
[440] K. Kim, A. Zagalskaya, J.L. Ng, J. Hong, V. Alexandrov, T.A. Pham, X. Su, Nat. Commun. 14 (2023) 823.
[441] S. Han, H. Li, T. Li, F. Chen, R. Yang, Y. Yu, B. Zhang, Nature Catalysis 6 (2023) 402–414.
[442] Y. Zhou, H. Sun, X. Hu, J. Guo, Y. Liang, X. Gong, X. Xiao, L. Luo, Z. Wu, P. Qin, J. Colloid Interface Sci. 683 (2025) 709–721.
[443] Y. Wang, Y. Zeng, J. Xie, C. Wang, C. Zhou, L. Song, K. Ma, H. Yue, Green Chem. 27 (2025) 1763–1770.
[444] N. Sun, Y. Guo, L. Luo, X. Cai, S. Shen, J. Zhang, Appl. Surf. Sci. 624 (2023) 157118.
[445] L. Dai, S. Li, Y. Dai, Y. Zheng, K. Liu, H. Li, B. Jiang, Chem. Eng. J. 498 (2024) 155735.

[446] X. Zhou, W. Xu, Y. Liang, H. Jiang, Z. Li, S. Wu, Z. Gao, Z. Cui, S. Zhu, ACS Catal. 14 (2024) 12251–12259.
[447] Y. Xu, L. Cao, H. Hua, R. Li, Y. Wang, J. Liu, Y. Wang, C. Fan, Chem. Eng. J. 508 (2025) 160985.
[448] J. Liu, Y. Li, X. Jia, J. Shen, Y. Zhu, C. Li, Small 21 (2025) 2408279.
[449] I.M.U. Hasan, L. Bo, N. Zhengrong, G. Dandan, Z. Yaoling, M.B. Shakoor, M. Z. Nawaz, Y. Liu, J. Qiao, N.K. Niazi, H. Feng, J. Mol. Liq. 435 (2025) 128058.
[450] N.U.H. Khan, Z.A. Gilani, M. Khalid Samiullah, H.M.N. Ul Huda Khan Asghar, M. Z. Nawaz, S.M. Ali, M.A. Khan, F.A. Sheikh, Applied Physics A 130 (2024) 321.
[451] N.-U.-H. Khan, Z.A. Gilani, M. Abid, G. Hussain Samiullah, M. Khalid, H.M. Noor Huda Khan Asghar, M.Z. Nawaz, S.M. Ali, M.A. Khan, F.A. Sheikh, R. Alotaibi, Applied Physics A 130 (2024) 829.
[452] F. Haider, M.S. Shifa, G.H. Tariq, H.M.N. Ul Huda Khan Asghar, M.M. Alam, A. Ali, M.A. Khan, Z.A. Gilani, M.Z. Nawaz, R. Alotaibi, S.M. Ali, Applied Physics A 131 (2025) 226.
[453] Z. Niu, S. Fan, X. Li, P. Wang, Z. Liu, J. Wang, C. Bai, D. Zhang, Chem. Eng. J. 450 (2022) 138343.
[454] Z. Niu, S. Fan, X. Li, J. Duan, A. Chen, Appl. Catal. B Environ. 322 (2023) 122090.
[455] F. Lai, J. Feng, X. Ye, W. Zong, G. He, C. Yang, W. Wang, Y.-E. Miao, B. Pan, W. Yan, T. Liu, I.P. Parkin, J. Mater. Chem. A 8 (2020) 1652–1659.
[456] J. Li, D. Zhao, L. Zhang, L. Yue, Y. Luo, Q. Liu, N. Li, A.A. Alshehri, M.S. Hamdy, Q. Li, X. Sun, Chem. Commun. 58 (2022) 4480–4483.
[457] X. He, T. Xie, K. Dong, J. Nan, H. Sun, Y. Yao, X. Fan, D. Zheng, Y. Luo, S. Sun, Q. Liu, L. Li, W. Chu, L. Xie, Q. Kong, X. Sun, Sci. China-Mater. 68 (2025) 2756–2763.
[458] S. He, V. Somayaji, M. Wang, S.-H. Lee, Z. Geng, S. Zhu, P. Novello, C.V. Varanasi, J. Liu, Nano Res. 15 (2022) 4785–4791.
[459] A.A. Bayode, O.T. Ore, E.A. Nnamani, B. Sotunde, D.T. Koko, E.I. Unuabonah, B. Helmreich, M.O. Omorogie, ACS Omega 9 (2024) 19770–19785.
[460] S. Zhang, G. Duan, L. Qiao, Y. Tang, Y. Chen, Y. Sun, P. Wan, S. Zhang, Ind. Eng. Chem. Res. 58 (2019) 8935–8939.
[461] Y. Chen, C. Chen, W.-H. Huang, C.-W. Pao, C.-C. Chang, T. Mao, J. Wang, H. Fu, F. Lai, N. Zhang, T. Liu, ACS Nano 18 (2024) 20530–20540.
[462] H. Zheng, Y. Zhang, Y. Wang, Z. Wu, F. Lai, G. Chao, N. Zhang, L. Zhang, T. Liu, Small 19 (2023) 2205625.
[463] Q. Yin, H. Zhou, Mater. Today Commun. 35 (2023) 106048.
[464] Y. Lv, J. Ren, M. Jiang, R. Wang, H. Guo, X. Sun, X. Guo, T. Li, ACS Catal. 15 (2025) 8094–8102.
[465] P. Hu, X. Zhang, M. Xu, Y. Lv, H. Guo, J.S. Chen, X. Ye, H. Xian, X. Sun, T. Li, Appl. Catal. B Environ. Energy 357 (2024) 124267.
[466] M. Xu, S. Dong, H. Guo, Z. Tao, Y. Jeon, Z. Zhang, Z. Chen, H. Su, Z. Liu, Y. Lin, J. T.S. Irvine, T. Li, D. Chen, Appl. Catal. B Environ. Energy 375 (2025) 125433.
[467] Z. Gong, W. Zhong, Z. He, C. Jia, D. Zhou, N. Zhang, X. Kang, Y. Chen, Catal. Today 402 (2022) 259–265.
[468] F. Liu, Z. Zhang, L. Shi, Y. Zhang, X. Qiu, Y. Dong, H. Jiang, Y. Zhu, J. Zhu, J. Mater. Chem. A 11 (2023) 10596–10604.
[469] J. Wang, D. Wu, M. Li, X. Wei, X. Yang, M. Shao, M. Gu, Nano Lett. 22 (2022) 5600–5606.
[470] C. Li, D. Ma, S. Mou, Y. Luo, B. Ma, S. Lu, G. Cui, Q. Li, Q. Liu, X. Sun, Journal of Energy Chemistry 50 (2020) 402–408.
[471] T. Wu, W. Kong, Y. Zhang, Z. Xing, J. Zhao, T. Wang, X. Shi, Y. Luo, X. Sun, Small Methods 3 (2019) 1900356.
[472] C. He, Z.-Y. Wu, L. Zhao, M. Ming, Y. Zhang, Y. Yi, J.-S. Hu, ACS Catal. 9 (2019) 7311–7317.
[473] J. Kong, A. Lim, C. Yoon, J.H. Jang, H.C. Ham, J. Han, S. Nam, D. Kim, Y.-E. Sung, J. Choi, H.S. Park, ACS Sustain. Chem. Eng. 5 (2017) 10986–10995.
[474] L. Hu, A. Khaniya, J. Wang, G. Chen, W.E. Kaden, X. Feng, ACS Catal. 8 (2018) 9312–9319.
[475] X. Zhao, X. Lan, D. Yu, H. Fu, Z. Liu, T. Mu, Chem. Commun. 54 (2018) 13010–13013.
[476] Q. Liu, X. Zhang, B. Zhang, Y. Luo, G. Cui, F. Xie, X. Sun, Nanoscale 10 (2018) 14386–14389.
[477] Y. Tian, D. Xu, K. Chu, Z. Wei, W. Liu, J. Mater. Sci. 54 (2019) 9088–9097.
[478] J. Miao, Q. Hong, L. Liang, G. Li, Z. Liu, S. Yin, Y. Chen, Chin. Chem. Lett. 35 (2024) 108935.
[479] X. Fan, L. Xie, J. Liang, Y. Ren, L. Zhang, L. Yue, T. Li, Y. Luo, N. Li, B. Tang, Nano Res. (2022) 1–6.
[480] T. Chouki, M. Machreki, I.A. Rutkowska, B. Rytelewska, P.J. Kulesza, G. Tyuliev, M. Harb, L.M. Azofra, S. Emin, J. Environ. Chem. Eng. 11 (2023) 109275.
[481] Z. Liu, C. Wang, C. Chen, C. Li, C. Guo, Electrochem. Commun. 131 (2021) 107121.
[482] Y. Zhang, X. Chen, W. Wang, L. Yin, J.C. Crittenden, Appl. Catal. B Environ. 310 (2022) 121346.
[483] P. Huang, T. Fan, X. Ma, J. Zhang, Y. Zhang, Z. Chen, X. Yi, ChemSusChem 15 (2022) e202102049.
[484] K. Wang, R. Mao, R. Liu, J. Zhang, H. Zhao, W. Ran, X. Zhao, Nature Water 1 (2023) 1068–1078.
[485] J. Qin, L. Chen, K. Wu, X. Wang, Q. Zhao, L. Li, B. Liu, Z. Ye, ACS Appl. Energy Mater. 5 (2021) 71–76.
[486] Z. Wang, J. Chang, Z. Gao, Inorganic Chemistry Frontiers 11 (2024) 8876–8889.
[487] Z. Gao, Y. Lai, Y. Tao, L. Xiao, L. Zhang, F. Luo, ACS Central Science 7 (2021) 1066–1072.
[488] M. Rinawati, Y.-S. Chiu, L.-Y. Chang, C.-Y. Chang, W.-N. Su, N.L.W. Septiani, B. Yuliarto, W.-H. Huang, J.-L. Chen, M.-H. Yeh, J. Mater. Chem. A 12 (2024) 22070–22081.
[489] J. Cai, Y. Wei, A. Cao, J. Huang, Z. Jiang, S. Lu, S.-Q. Zang, Appl. Catal. B Environ. 316 (2022) 121683.
[490] Q. Hu, Y. Qin, X. Wang, Z. Wang, X. Huang, H. Zheng, K. Gao, H. Yang, P. Zhang, M. Shao, Energy Environ. Sci. 14 (2021) 4989–4997.
[491] Y. Wang, S. Shu, M. Peng, L. Hu, X. Lv, Y. Shen, H. Gong, G. Jiang, Nanoscale 13 (2021) 17504–17511.
[492] Y. Liu, R. Cheng, H. Ren, T. Sun, D. Liu, ACS Sustain. Chem. Eng. 12 (2024) 3780–3789.
[493] Q. Ru, P. Bai, X. Kong, L. Xu, Chem. Eng. Sci. 298 (2024) 120378.
[494] Y. Jia, Y.-G. Ji, Q. Xue, F.-M. Li, G.-T. Zhao, P.-J. Jin, S.-N. Li, Y. Chen, ACS Appl. Mater. Interfaces 13 (2021) 45521–45527.
[495] Y. Xu, M. Wang, K. Ren, T. Ren, M. Liu, Z. Wang, X. Li, L. Wang, H. Wang, J. Mater. Chem. A 9 (2021) 16411–16417.
[496] X. Hu, M. Zhang, C. Lai, M. Cheng, F. Xu, D. Ma, L. Li, H. Yan, H. Sun, X. Fan, B. Wang, Chem. Eng. J. 493 (2024) 152543.
[497] J. Zhou, M. Wen, R. Huang, Q. Wu, Y. Luo, Y. Tian, G. Wei, Y. Fu, Energy Environ. Sci. 16 (2023) 2611–2620.
[498] Y. Han, X. Zhang, W. Cai, H. Zhao, Y. Zhang, Y. Sun, Z. Hu, S. Li, J. Lai, L. Wang, J. Colloid Interface Sci. 600 (2021) 620–628.
[499] J. Wang, C. Cai, Y. Wang, X. Yang, D. Wu, Y. Zhu, M. Li, M. Gu, M. Shao, ACS Catal. 11 (2021) 15135–15140.
[500] X. Fu, X. Zhao, X. Hu, K. He, Y. Yu, T. Li, Q. Tu, X. Qian, Q. Yue, M. R. Wasielewski, Y. Kang, Appl. Mater. Today 19 (2020) 100620.
[501] X. Lu, H. Song, J. Cai, S. Lu, Electrochem. Commun. 129 (2021) 107094.
[502] N.C. Kani, J.A. Gauthier, A. Prajapati, J. Edgington, I. Bordawekar, W. Shields, M. Shields, L.C. Seitz, A.R. Singh, M.R. Singh, Energy Environ. Sci. 14 (2021) 6349–6359.
[503] H. Wang, Q. Mao, T. Ren, T. Zhou, K. Deng, Z. Wang, X. Li, Y. Xu, L. Wang, ACS Appl. Mater. Interfaces 13 (2021) 44733–44741.
[504] F. Lei, W. Xu, J. Yu, K. Li, J. Xie, P. Hao, G. Cui, B. Tang, Chem. Eng. J. 426 (2021) 131317.
[505] X. Zhao, X. Jia, Y. He, H. Zhang, X. Zhou, H. Zhang, S. Zhang, Y. Dong, X. Hu, A. V. Kuklin, G.V. Baryshnikov, H. Ågren, G. Hu, Appl. Mater. Today 25 (2021) 101206.
[506] Q.-L. Hong, J. Zhou, Q.-G. Zhai, Y.-C. Jiang, M.-C. Hu, X. Xiao, S.-N. Li, Y. Chen, Chem. Commun. 57 (2021) 11621–11624.
[507] Y. Zhao, Y. Liu, Z. Zhang, Z. Mo, C. Wang, S. Gao, Nano Energy 97 (2022) 107124.
[508] H. Choi, M. Jun, W. Kang, T. Kim, S. Choi, C. Choi, H. Wang, H. Baik, Y. Jung, K. Jin, K. Lee, Chem Catalysis 4 (2024) 101029.
[509] Y. Li, S. Xiao, X. Li, C. Chang, M. Xie, J. Xu, Z. Yang, Mater. Today Phys. 19 (2021) 100431.
[510] G.-Y. Zhai, Q.-Y. Li, S.-N. Zhang, D. Xu, S.-Y. Xia, P. Gao, X. Lin, Y.-X. Lin, J.-H. Cheng, W.-Y. Hu, L.-H. Sun, X.-H. Li, J.-S. Chen, CCS Chem. 4 (2022) 3455–3462.
[511] W. Yu, J. Yu, M. Huang, Y. Wang, Y. Wang, J. Li, H. Liu, W. Zhou, Energy Environ. Sci. 16 (2023) 2991–3001.
[512] Y. Wang, L. Zhang, Y. Niu, D. Fang, J. Wang, Q. Su, C. Wang, Green Chem. 23 (2021) 7594–7608.
[513] T. Hu, C. Wang, M. Wang, C.M. Li, C. Guo, ACS Catal. 11 (2021) 14417–14427.